INELASTIC LIGHT SCATTERING INVESTIGATIONS ON NOVEL MATERIALS

A Thesis
Submitted for the Degree of
DOCTOR OF PHILOSOPHY

By

GOPAL K. PRADHAN

CHEMISTRY AND PHYSICS OF MATERIALS UNIT
JAWAHARLAL NEHRU CENTRE FOR ADVANCED SCIENTIFIC RESEARCH
BANGALORE – 560 064, INDIA.
FEBRUARY 2010

Dedicated to

My Family

DECLARATION

I hereby declare that the matter embodied in this thesis entitled “**Inelastic Light Scattering Investigations on Novel Materials**" is the result of the investigations carried out by me in the Chemistry and Physics of Materials Unit, Jawaharlal Nehru Centre for Advanced Scientific Research (JNCASR), Bangalore, India, under the supervision of Professor Chandrabhas Narayana.

In keeping with the general practice of reporting scientific observations, due acknowledgements have been made whenever the work described is based on the findings of other investigators. Any omission which might have occurred by oversight or error in judgement is regretted.

Gopal K. Pradhan

CERTIFICATE

I hereby certify that the matter embodied in this thesis entitled “**Inelastic Light Scattering Investigations on Novel Materials**" has been carried out by Mr. Gopal K. Pradhan at the Chemistry and Physics of Materials Unit, Jawaharlal Nehru Centre for Advanced Scientific Research (JNCASR), Bangalore, India under my supervision and that it has not been submitted elsewhere for the award of any degree or diploma.

Prof. Chandrabhas Narayana

(Research Supervisor)

ACKNOWLEDGEMENTS

It is always a matter of great pleasure to acknowledge people who have inspired, motivated and supported me by sharing their knowledge and wisdom. I take this opportunity to extend my gratitude to all of them who had a great impact on my academic as well as personal life.

First of all, I had been extremely fortunate to get a wonderful mentor like Prof. Chandrabhas Narayana. I would like to thank him and convey my deepest sense of gratitude for providing excellent guidance through ample scientific inputs, enormous freedom in workplace and giving an exposure to wide variety of scientific problems. He has been very supportive in my professional as well as personal life. All this has been pivotal in making me a better scientist and a good human being. I have always admired his extraordinary energy and enthusiasm in everything that he does.

I wish to thank Prof. Ajay K. Sood, IISc (Bangalore). I have been immensely benefited from many stimulating discussions with him. I really liked his approach in attempting scientific problems.

I want to thank Prof. C. N. R. Rao for his never ending enthusiasm for science. He continues to be a source of inspiration for many of us.

I would like to thank all of our collaborators Prof Olivier Pages (Université Paul Verlaine, France), Dr. S. K. Deb (CAT, Indore), Prof. T. N. Guru Row and Dr. Diptikanta Swain (IISc, Bangalore), Prof. A. K. Ganguly (IIT Delhi), Prof. A. Sunderesan and Dr V.K. Mangalam (JNCASR), Prof. Umesh Waghmare and Mr. Anil Kumar (JNCASR), Prof. B. V. R. Tata and Ms Brijitta (IGCAR, Kalpakkam). I have learnt a great deal from Prof. Pages during our work on semiconductor alloys. I have been associated with Dr. S. K. Deb in many ways. Though it has been a nice learning experience with him, his help has been particularly useful in understanding, analyzing *and performing synchrotron high pressure XRD measurements. I have learnt several things about symmetry and x-ray crystallography from Dr. Diptikanta Swain. I thank Surajit of IISc for being extremely helpful while doing some of the Laue diffraction experiments. I also have had many useful discussions with him on pyrochlores and Raman.*

I would like to thank the faculties of CPMU, TSU and EMU, Prof. K B R Verma, S.B. Kripanidhi and Sriram Ramaswamy (IISc) for their wonderful courses. I had many useful discussions with Prof Srikanth Sastry, K. R. Sreenivas and Meheboob Alam. I thank all of them.

I would like to thank Dr. Tomasz Blachowicz, Poland who has been very generous in donating his book on Brillouin scattering. I greatly benefited from the book.

I had some amazing lab mates (past and present) like Drs (Motin, Kavitha, Pavan, Nashiour and Navneet), Jyotirmayee, Partha, Srinu, Soumik, Sonia, Gayatri and Ritu. We had lots of fun together and we have always learnt from each other. They have always kept the lab atmosphere a terrific place to work. I thank all of them. A special thank to Partha and Srinu for their critical reading of my thesis. I thank K.R.G. Karthik who spent couple of months with me in the lab. I thank him for his help in some of the experiments.

I had some fantastic batch mates, friends and well wishers at JNCASR. Few of them need special mention. They are Shibu, Dhritiman, Chandrasekhar, Jyoti, Jaita, Hembram, Kirti, Sasmita, Soumya, Prakash, Gayatri, Surbhi, Pranab, Moumita Maiti, Raju, Abhishek, Saikrishna, Thiru, Joydeep, Mousumi and Ayan. I thank all of them for their support and encouragement. They had made my stay at JNC pleasant and enjoyable.

I am privileged to have some wonderful friends, seniors and juniors from my MSc and BSc days. The list includes Sudhansu, Jaykrishna (D), Tapan, Ramakanta, Jaykrishna (K), Sujit Bhutia, Surya Narayan, Suchismita, Itishri, Mamata, Arun, Savilash, Bibhuti, Ganapati, Jagdeesh, Bibhu Ranjan, Kalpataru, Pramod, Himanshu, Saumya Ranjan, Madhusmita, Padmanav, Dr. Himanshu, Dr Debashish, Debakanta, Anant, Bharat, Bhupal and Ajay. Sudhansu has always been a great source of inspiration and strength to me and has provided extraordinary support in both good and bad times. I would like to thank all these wonderful and sweet personalities for making life memorable and pleasant.

I express my heartfelt thank to all the academic, technical, library and computer lab staff members of JNCASR. A special thank to Mr. Arokyanathan, whom we fondly call "Professor", has been instrumental in fabricating many of our experimental designs.

I have been very fortunate to be taught by many great teachers who value knowledge and wisdom equally. I thank all of them. Prof Karmadev Maharana and Swapna Mahapatra have provided me outstanding support during my MSc days. I owe a lot to both of them. I would also like to thank four outstanding teachers Prof. C. C. Hazra, Mahendra sir, Benudhar sir and Kahnu sir who have influenced me in a big way.

I would like to take this very special opportunity to thank my family who have been very supportive despite of all the difficulties and I dedicate this work to them.

Preface

This thesis is unified more by the ubiquity and versatility of the use of inelastic light scattering (ILS) spectroscopy coupled with the two thermodynamic variables (pressure and temperature) within the realm of condensed matter physics than by the investigation of a single topic. The experimental investigations described in the resulting chapters each addresses discrete topics about different class of materials. Along with ILS, in order to understand specific material properties and open issues in these materials, the two thermodynamic variables, namely pressure and temperature were used wherever necessary. The thesis consists of six chapters and is divided into two parts (Part A and B). Introduction to general aspect of inelastic light scattering along with pressure and temperature effects on it, experimental details of Raman, Brillouin scattering and high pressure technique, high pressure Raman investigations on ZnBeSe ternary alloys, and high temperature Raman studies on $Na_2Cd(SO4)_2$ (NCSO) each occupies a chapter in Part A. Low temperature studies on acoustic phonons in pyrochlores $RE_2Ti_2O_7$ (RE = Sm, Dy, Ho, Lu) and elastic properties of double walled carbon nanotubes (DWCNT), studied by Brillouin scattering each occupies a chapter in Part B. Each chapter includes a topical introduction about the material under investigation.

Chapter 1 accounts a thorough introduction about the general aspects of inelastic light scattering (ILS). Effect of temperature and pressure on materials and how temperature or/and pressure studies integrated with ILS can be used to obtain useful information about material properties are also touched upon.

Chapter 2 describes about the experimental details of the design and working principles of Raman and Brillouin scattering setup. The methods of doing high pressure Raman experiments have also been discussed.

Chapter 3 contains high pressure Raman investigations up to about 25GPa on $Zn_{1-x}Be_xSe$, an II-VI wide band gap ternary alloy. In this chapter, from the high pressure Raman studies, we discuss about nature of the alloy formation within the percolation picture, semiconductor-metal phase transition related to the structural stability of the alloy for different Be concentration of x= 11.6, 16 and 24% .

Chapter 4 is about high temperature phase transition studies on a novel fast ion conductor material NCSO using Raman spectroscopy. This material shows two conductivity transitions at high temperature. In this chapter, role of SO_4 ions in these conductivity transitions of NCSO is elucidated using Raman spectroscopy.

Chapter 5 discusses low temperature acoustic phonon behavior studies in pyrochlores $RE_2Ti_2O_7$ (RE = Sm, Dy, Ho, Lu) using Brillouin scattering. Here we have investigated subtle structural transitions in the pyrochlore lattice of $Dy_2Ti_2O_7$ using temperature dependent Brillouin scattering from 300-25K.

In **Chapter 6,** Brillouin scattering was used to investigate the acoustic properties of double walled carbon nanotubes (DWCNT). Here we have studied the bulk acoustic modes in DWCNT bundles and determine the average bulk sound velocity.

Table of Contents

Preface viii

Chapter 1 Introduction 1

1.1 Scattering of Light 2

1.2 Raman Scattering 4

1.2.1 Macroscopic Theory of Raman Scattering 5

1.2.2 Microscopic Theory of Raman Scattering 8

1.3 Brillouin Scattering 13

1.3.1 Brillouin Scattering in solids 15

1.3.2 Brillouin Scattering in fluids 19

1.3.3 Brillouin scattering in opaque materials 21

1.4 Kinematics of Light Scattering 22

1.5 Pressure and Temperature Effects on Materials 25

1.5.1 Pressure Units 28

1.5.2 Methods for generating High Pressure 30

1.6 References 31

Chapter 2 Experimental Techniques 38

2.1 Raman Spectrometer 39

2.1.1 Design, Fabrication and performance of the Raman microscope 40

2.2 Brillouin Spectrometer 46

2.2.1 The Fabry-Perot interferometer 47

2.2.2 Interferometer Construction 51

2.2.3 Alignment of the interferometer 53

2.2.4 Stabilizing the interferometer 55

2.2.5 Detection of the scattered light 55

2.2.6 180^o backscattering geometry 56

2.3 High Pressure Techniques 57

2.3.1 Diamond Anvil Cell 58

2.3.2 Mao-Bell Diamond Anvil Cell 60

2.3.3 Diamond 61

2.3.4 Backing plates 62
2.3.5 Diamond alignment 63
2.3.6 Gasket 64
2.3.7 Pressure medium 65
2.3.8 Pressure measurement 67
2.4 Temperature dependent studies 68
2.5 References 68

Chapter 3 High Pressure Raman Scattering Investigations on $Zn_{1-x}Be_xSe$ (x = 0.112, 0.16 and 0.24) Ternary Alloy. 74
3.1 Introduction 75
3.2 Experimental 78
3.3 *Ab initio* calculation 78
3.4 Results and Discussions 79
3.4.1 Zn-Se spectral range 85
3.4.2 Be-Se spectral range 89
3.5 Conclusions 92
3.6 References 93

Chapter 4 High Temperature Raman Studies on a Novel Fast Ion Conductor, $Na_2Cd(SO4)_2$ 97
4.1 Introduction 98
4.2 Experimental Details 101
4.3 Results and Discussion 101
4.4 Conclusion 107
4.5 References 107

Chapter 5 Temperature Dependent Brillouin Scattering Investigations of the Acoustic Phonons in Pyrochlores $RE_2Ti_2O_7$ (RE = Sm, Dy, Ho and Lu) 111
5.1 Introduction 112
5.2 Experimental details 115
5.3 Results and discussions 116
5.4 Conclusion 126
5.5 References 126

Chapter 6 Inelastic Light Scattering from the Acoustic Modes of Double Walled Carbon Nanotubes 129

6.1 Introduction 130

6.2 Experimental details 133

6.3 Results and discussion 137

6.4 Conclusion 139

6.5 References 140

Miscellaneous Work 144

List of Figures

Figure 1-1: Feynman diagram for Stokes’s (Left) and anti-Stokes (Right) Raman process. 8
Figure 1-2 - Schematic diagram of the energy states involved in Raman scattering (Left - Stokes process, Right- anti-stokes process) 10
Figure 1-3: Wave vector conservation of the incident and scattered light 23
Figure 2-4: Phonon Dispersion Relations 24
Figure 1-5: The pressure scale range (1 atm = 10^5 Pa) in nature encompasses 64 orders of magnitude. The right-hand side of the scale relates to experimentally attainable conditions 29
Figure 2-1 : Schematic of the micro- Raman spectrometer: MS- Micro stage; OL- Objective lens, DM – Dichroic mirror, SM- special mirror, AS – Aperture stop, FS – Field stop, NDF - Neutral density filter, PF – Plasma filter, M1 (M) – Movable mirror, EP – Eyepiece, BS (M) – Movable beam splitter, M2 – Mirror, CAM – Camera, EF, Edge filter, FL- Focusing lens, OF- Optical fibre, MONO – Monochromator, CCD - Charge coupled device, PC – personal computer 41
Figure 2-2 : Fabricated Raman spectrometer. 45
Figure 2-3: Raman spectra of silicon. 45
Figure 2-4 : Transmission of a Fabry-Perot interferometer 48
Figure 2-5 : Schematic diagram of an interferometer in tandem opearation 50
Figure 2-6 : Transmission from a Fabry-Perot interferometer operated in Tandem 51
Figure 2-7: Lay out of the Brillouin spectromter. 53
Figure 2-8 Alignment procedure for the interferometer 54
Figure 2-9: Schematic of representation of the experimental setup in the backscattering geometry used for the present study. BS – Beam Splitter, M- Mirror, CL- camera lens, S- Sample, AD – Achromatic doublet, MS- Mechanical shutter, FP1, FP2 – Fabry- Perot etalon pair, DA&D- Data Acquisition and display 56
Figure 2-10: - Schematic of a diamond anvil mechanism. 59
Figure 2-11 : Schematic of the Mao-Bell diamond anvil cell. 60
Figure 2-12 Picture of the used DAC (left) and an exploded view of the DAC (right) 61
Figure 2-13: A hole drilled in a preindented gasket. 65
Figure 3-1: Raman spectra of $Zn_{1-x}Be_xSe$ (x = .112, .16 and .24) at ambient conditions of temperature and pressure. 80
Figure 3-2: a)- Pressure-dependent Raman spectra of Zn0.88Be0.112Se. b)-The frequency versus pressure variations of the main features are shown in the inset. Remarkable trends (A,B,C) are marked by circles. 82

Figure 3-3: a) Pressure-dependent Raman spectra of $Zn_{0.84}Be_{0.16}Se$. b)-The frequency versus pressure variations of the main features are shown in the inset. Remarkable trends (A,B,C) are marked by circles. 83

Figure 3-4 : Pressure-dependent Raman spectra of Zn0.76Be0.24Se. The frequency versus pressure variations of the main features are shown in the inset. Remarkable trends (A,B,C) are marked by circles. The antiresonances (squares) and the strong peak (star) are characteristic of anharmonic coupling. 84

Figure 3-5: Schematic explanation of features A and B (circles) by referring to pure ZnSe (symbols, digitalized from Ref. [22]). In the alloy the weak TO_{Zn-Se}^{Be} (thick line – in the vibration pattern the dotted and plain lines indicate perpendicular planes) appears on top of the strong TO_{Zn-Se}^{Zn} (pure- ZnSe like, dashed line). The natural splitting of ~8 cm^{-1} is magnified to ~30 cm^{-1} by an anharmonic coupling that downshifts the weak mode from the thick line to the thin one. The lineshapes of the weak mode over its decoupling process are shown in the inset. The star and squares mark features characteristic of anharmonic coupling, as in Fig. 4. At 8 GPa an arrow marks the position of the harmonic mode, for reference purpose. 86

Figure 3-6: *Ab initio* ZC TO-DOS per impurity of the 2-imp. Be (main curves) and P (inset) motifs in ZnSe- and GaAs-like supercells, respectively. The Be-Se vibration patterns are indicated, emphasizing the bond-stretching modes (dashed areas) in reference to feature C (circle). 90

Figure 4-1: Packing diagram of $Na_2Cd(SO_4)_2$, view down the *z*-axis. 99

Figure 4-2: Channels of $Cd_4(SO_4)_4$ 100

Figure 4-3: Room-temperature infrared and Raman spectra of $Na_2Cd(SO_4)_2$ showing the SO_4 internal vibrational modes 102

Figure 4-4: Temperature evolution of the Raman spectra of $Na_2Cd(SO_4)_2$ in the temperature interval 550-595 °C. 103

Figure 4-5: Temperature dependence of the fwhm of the v_1 mode of the SO_4 ion in the temperature interval 24-595 °C. 104

Figure 4-6: Temperature dependences of the v_2 and v_4 modes of the SO_4 ion in the temperature interval 24-595 °C. 105

Figure 5-1: Structure of the Pyrochlore lattice 112

Figure 5-2: Room temperature Brillouin spectra of STO, DTO, HTO and LTO 117

Figure 5-3: Laue photograph of DTO 118

Figure 5-4: Temperature evolution of the Brillouin spectra of STO 119

Figure 5-5: Temperature evolution of the Brillouin spectra of DTO 120
Figure 5-6: Temperature evolution of the Brillouin spectra of HTO 121
Figure 5-7: Temperature evolution of the Brillouin spectra of LTO 122
Figure 5-8: Longitudinal sound velocities of STO, DTO, HTO and LTO as a function of temperature. 123
Figure 5-9: Transverse sound velocities of DTO as a function of temperature. 125
Figure 6-1: The unrolled graphene sheet (honeycomb lattice). When we connect sites O and A, and sites B and B', a nanotube can be constructed. The vectors OA and OB define the chiral vector C_h and the translational vector T of the nanotube, respectively. The rectangle OABB' defines the unit cell for the nanotube 131
Figure 6-2: High resolution SEM micrograph of as-produced CVD DWCNT matted film used in the work. 134
Figure 6-3: HRTEM Micrograph of a cross section of a CVD DWCNT bundle, with individual tubes about 2.2 nm in diameter. 135
Figure 6-4: HRTEM Micrograph of a single DWCNT end 135
Figure 6-5: Schematic representation of the experimental geometry 136
Figure 6-6: Anti-Stokes Brillouin spectra of DWCNT. The solid line is a Lorentzian fit. 137
Figure 6-7: Brillouin spectra for different azimuthal rotations (φ) along the surface normal. 138

Chapter 1

Introduction

1.1 Scattering of Light

Scattering of light has long been a topic of great fascination for physicists right from the beginning of investigations on the properties of light. The subject has a very long, rich and eventful history. Curiosity about the explanation of the blue colour of the sky led Lord Rayleigh to formulate the classical theory of light scattering without change of frequency, now known as Rayleigh scattering. However, the first recorded experiments were by Tyndall,[1] who observed that blue light is more strongly scattered than light of lower frequency and also noted that the scattered light was strongly polarized. It was in 1871, the first satisfactory explanation of even the most elementary aspects of scattering came from Lord Rayleigh[2] who deduced his well-known λ^{-4} law for light scattering by objects whose dimensions are small compared with the wavelength of the incident light. Individual atoms, molecules and electrons, being such particles, scatter light elastically (i.e. without change in frequency) according to Rayleigh's law. Elastic scattering of light can also arise from larger scattering centres like dust particles, and is usually known as Mie scattering.[3] More progress was made in the early part of 20th century when Einstein[4] and Smoluchowski[5,6] suggested the use of fluctuation theory to account for the variations in local dielectric constant which cause the scattering in otherwise homogeneous media. The theoretical possibility that light may be scattered inelastically was first predicted by Brillouin,[7] who calculated the spectrum of light scattered from periodic, coherent fluctuations in the density of a liquid or solid. Smekal[8] developed the theory of light scattering by a system with two quantized energy levels. If it was blueness of sky that led Rayleigh to put forth his theory, fascination with the marvelous blue of the Mediterranean sea and scattering of x-rays by electrons (i.e. Compton scattering) inspired C. V. Raman[9-11] to investigate the scattering of light from liquids and to discover experimentally the scattering of light with change of frequency known as "Raman effect".

Shortly after Raman and Krishnan's publication, there was a similar observation of light scattering with change of frequency in quartz reported by two Russian scientists, Landsberg and Mandelstam.[12] Smekal's theory contained the essential characteristics of the phenomena discovered in liquids by Raman and, independently, by Landsberg and Mandelstam. It was soon realized that the newly discovered effect constituted an excellent tool to study excitations of molecules and molecular structure. The inelastic scattering from sound waves, predicted by Brillouin,[7] known as Brillouin scattering, was first observed in quartz and liquids by Gross.[13,14] The scattering in this case arises from the fluctuations in dielectric constant of the medium. The two scattering processes are treated similarly whether these fluctuations arise from molecular vibrations, sound waves or diffusional motion. In each case some energy is exchanged between the light and the scattering medium, the difference being merely in the magnitude of this exchange. The reasons for the division are largely historical, but in practice it turns out that there is a natural experimental basis for using different experimental techniques because of the three different frequency regions probed. The potential of these two inelastic light scattering (Raman and Brillouin scattering) phenomena in condensed matter was realized immediately. Today, the range of applicability of light scattering in condensed matter is enormous and wide. After the advent of laser, sophisticated spectrometers with associated electronics, inelastic light scattering spectroscopy has emerged as one of the most powerful and most widely used optical techniques for material characterization. The signature of this versatility is reflected in the voluminous work reported in the series of monographs in the Light Scattering in Solids edited by Cardona *et al*.[15-23] A detailed discussion on various aspects of Raman and Brillouin scattering is described below.

1.2 Raman Scattering

When light travels through a medium, it is either transmitted or absorbed following the laws of reflection and refraction, a tiny fraction is scattered by inhomogeneities in the medium. These inhomogeneities can be static or dynamic. For purely geometric or local inhomogeneities with no time dependence the scattering is elastic. Defects such as dislocations in a crystal are static scattering centres, and they scatter light elastically. Fluctuations in the density of the medium that are associated with the phonons (atomic vibrations) are examples of dynamic scatterers, and they scatter light inelastically. The Raman scattering is an inelastic light scattering process in which the incident light with momentum $\hbar k_i$ and energy $\hbar\omega_i$ is modified by an interaction (i.e creation and annihilation) with elementary excitations (quasi particles) of the matter leading to either an increase (anti-Stokes process) or a decrease (Stokes process) in the scattered photon energy $\hbar\omega_s$ as well as a momentum transfer $\hbar q$ to the matter. The elementary excitations could be optical phonons, surface and bulk polaritons, magnons, plasmons as well as electronic and vibrational excitations of isolated ions in crystals and molecular vibrations in liquids. In this thesis, we would be dealing with the lattice vibrations (phonons) which are the elementary excitation of interest described by their quasi-momentum $\hbar q$ and energy $\hbar\Omega$. Raman spectroscopy is very useful in identifying vibration modes (phonons) in solids. The phonon frequencies of a material depend on the chemical bonding and structure. So Raman scattering is very useful in getting the bonding and structural information of materials. Since vibrational modes are affected by external perturbations (such as pressure, temperature, magnetic/electric fields etc.), one can explore structural changes using Raman spectroscopy. It is also a very useful technique in chemistry, as it can be used to identify molecules and radicals since the Raman spectrum can be considered to be like a ‘fingerprint’ of any substance.

1.2.1 Macroscopic Theory of Raman Scattering

When the crystal is subjected to the oscillating electric field $E = E_0 e^{i\omega_0 t}$ of the incident electromagnetic radiation, it induces a polarization in the crystal. In the linear approximation, the induced electric polarization in any specific direction is given by

$$P_i = \chi_{ij} E_j , \tag{1.1}$$

where χ_{ij} is the susceptibility tensor. (For molecules one has to consider polarizability (α_{ij}) tensor instead of susceptibility). The susceptibility becomes altered as the atoms in the solid are vibrating periodically around the equilibrium positions. Within the framework of classical electrodynamics the scattered light can be described as the oscillation of an ensemble of dipoles, the Raman scattering intensity can thus be expressed by the dipole radiation intensity using the transition susceptibility

$$I_s = I_i \frac{\omega_s^4 V}{(4\pi\varepsilon\varepsilon_0)^2 c^4} \left| \hat{e}_s . \chi . \hat{e}_i \right|^2 \tag{1.2}$$

Thus, for a particular vibrating mode (phonon) at a frequency Ω_j, each component of the susceptibility tensor can be expressed as

$$\chi_{ij} = \chi_{ij}{}^{(0)} + \sum \frac{\partial \chi_{ij}}{\partial Q_k} Q_k + \tfrac{1}{2} \sum \left(\frac{\partial^2 \chi_{ij}}{\partial Q_k \partial Q_l} \right) Q_k Q_l + \text{higher order terms (h.o.t)} \tag{1.3}$$

where $Q_j = Q_0 e^{\pm i\Omega_j t}$ represents a normal coordinate measured from the equilibrium position. Therefore, using Eq. (1.3), the induced polarization can be written as

$$P_i = \chi_{ij}^0 E_{0j} e^{i\omega_i t} + E_{0j} Q_0 \sum \frac{\partial \chi_{ij}}{\partial Q_k} e^{i(\omega_i \pm \Omega_j)t} + \frac{1}{2} E_{0j} Q_0^2 \sum \left(\frac{\partial^2 \chi_{ij}}{\partial Q_k \partial Q_l} \right) e^{i(\omega_i \pm \Omega_k \pm \Omega_l)t} + \text{h.o.t} \tag{1.4}$$

This expression corresponds to oscillating dipoles re-radiating light at frequencies, ω_0 (Rayleigh scattering), $\omega_i - \Omega_j$ (Stokes Raman scattering), and $\omega_i + \Omega_j$ (anti-Stokes Raman scattering). This explains the appearance of the Raman lines as symmetric side bands with respect to ω_i. In the case of the one-phonon (1st order) Raman process the energy of the scattered light photons is shifted by Ω_j. The two-phonon (second order) Raman process leads to scattered photons with frequencies of $\omega_s = \omega_i \pm \Omega_i \pm \Omega_j$. There are several additional phonon processes concerning influences by electric fields and deformation gradients. The radiated intensity of such oscillating dipoles is proportional to $\left| \frac{d^2 P}{dt^2} \right|^2$, so that we can write:

$$I \propto \omega_i^4 (\chi_{ij}^0 E_{0j})^2 + \omega_S^4 \left(Q_{0E_{0j}} \frac{\partial \chi_{ij}}{\partial Q_k} Q_k \right) + \text{higher order terms} \tag{1.5}$$

The first term on the right-hand side of Eq. (1.5) accounts for the intensity due to Rayleigh scattered light (elastic), while the second term is related to the intensity of the Raman scattered (inelastic) light. For visible light $\omega_i \sim 10^{15}$ Hz, while the characteristic phonon frequencies are much shorter, typically $\Omega \sim 10^{12}$ Hz. So $\omega_i^4 \approx \omega_s^4$ and the intensity of Raman scattering varies as ω_i^4. It should be mentioned that Raman and infrared (IR) absorption spectra (i.e., absorption spectra among vibrational levels) are very often complementary methods to investigate the energy-level structure associated with vibrations. In Chapter 4, we use both Raman and IR to unambiguously assign the internal vibration of a tetrahedral SO_4 molecular unit in a fast ion conductor crystal called $Na_2Cd(SO_4)_2$ (NCSO). If a vibration (phonon) causes a change in the dipole moment of the system, which occurs when the symmetry of the charge density distribution is changed, then the vibration is *infrared active*. Mathematically, it can be represented as $(\partial P / \partial Q)|_0 \neq 0$. On the other hand, according to Eq. (1.5), if a vibration causes a change in polarizability (or susceptibility), that isn $(\partial \chi / \partial Q)|_0 \neq 0$, then it is *Raman active*. For local symmetries with a ‘centre of symmetry’, an infrared active vibration is Raman inactive, and vice versa. This rule is usually known as the *mutual exclusion principle.*

The partial derivatives in Eq. (1.4) constitute the Raman polarizability, often termed as Raman tensor $\Re$. For a first order one-phonon Raman process, $\Re$ is given by the complex second rank tensor

$$\Re = (\frac{\partial \chi}{\partial Q})_0 \hat{Q}_0(\omega_0) \tag{1.6}$$

where, $\hat{Q} = Q / |Q|$ a unit vector parallel to the phonon displacement and the corresponding Raman scattering intensity is given by

$$I_s \sim |\hat{e}_s.\Re.\hat{e}_i|^2 \quad , \tag{1.7}$$

which depends on the polarization ($\hat{e}_i$ and $\hat{e}_s$) of the incident and scattered radiation. By measuring the dependence of the scattering intensity on the incident and scattered polarization one can deduce the symmetry of the corresponding Raman active phonon. Symmetries of the medium and of the vibrations involved in the scattering impose requirements on the Raman tensor. The result of these symmetry requirements is that the scattered radiation vanishes for certain choices of the polarisation $\hat{e}_i$ and $\hat{e}_s$ and scattering geometries. These are the so-called Raman selection rules. The scattering geometry is specified by four vectors: k_i and k_s (the directions of the incident and scattered light, respectively), $\hat{e}_i$ and $\hat{e}_s$ (the polarisations of the incident and scattered light, respectively). These four vectors define the scattering configuration usually represented as $k_i(\hat{e}_i, \hat{e}_s)k_s$ which is known as the Porto notation.[24]

1.2.2 Microscopic Theory of Raman Scattering

The microscopic details of the Raman scattering mechanism can be obtained by using quantum mechanics in the third order time-dependent perturbation theory. At first sight it might look like that this scattering process can be described by a Hamiltonian involving photons and phonons only. However, the strength of such an interaction is very weak, unless the photon and phonon have comparable energies. This is not the case for visible or ultraviolet light scattering. In fact the interaction between the photons and phonons is mediated by an electron.[25] The Raman scattering process by phonons then can be described by three interactions[15,26] which are visualized in Fig.1-1 through Feynman diagram.

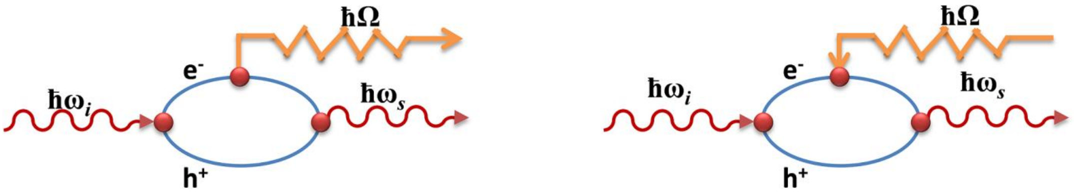

Figure 1-1: Feynman diagram for Stokes’s (Left) and anti-Stokes (Right) Raman process.

The scattering occurs in a three step process as the following.

1. Photon-electronic system interaction - An incident photon excites the electrons from ground state $|0\rangle$ into an intermediate (virtual) state $|i\rangle$ by creating an electron-hole pair.
2. Electron-phonon or hole-phonon interaction- Due to creation or annihilation of a phonon in the lattice with energy $\hbar\Omega$, the intermediate state $|i\rangle$ goes to another state $|i'\rangle$ with energy lower (Stokes process) or higher (anti-Stokes process) than that of the state $|i\rangle$.
3. Electron - photon interaction - Finally the electron-hole pair in the state $|i'\rangle$ recombines radiatively with the emission of the Raman scattered photon. A schematic diagram of the energy states in the scattering process is shown in Fig. 1-2.

The combination of these three interactions leads in third order perturbation theory to[15]

$$\hat{e}_s.\Re.\hat{e}_i \sim \frac{\langle 0|\hat{e}_s.p|i'\rangle\langle i'|H_{ep}|i\rangle\langle i|p.\hat{e}_i|0\rangle}{(E_{i'}-\hbar\omega_s)(E_i-\hbar\omega_i)} \tag{1.8}$$

Here p is the electron momentum, H_{ep} is the electron (hole)-phonon interaction Hamiltonian, $E_i, E_{i'}, \omega_s$ and ω_i are defined in Fig. 1-2. It is important to note that the virtual electronic levels in Fig. 1-2 do not necessarily correspond to real stationary eigenstates. As a result, Raman scattering is much weaker than fluorescence phenomena (by an efficiency factor of about 10^{-5} to 10^{-7}). When the frequency of the incident light is resonant with the energy difference between two real electronic levels, the scattering cross section becomes very large [see Eq. (1.7) and (1.8)] and the efficiency can be enhanced by a factor of 10^6. This is called Resonance Raman effect.[16,26,27]

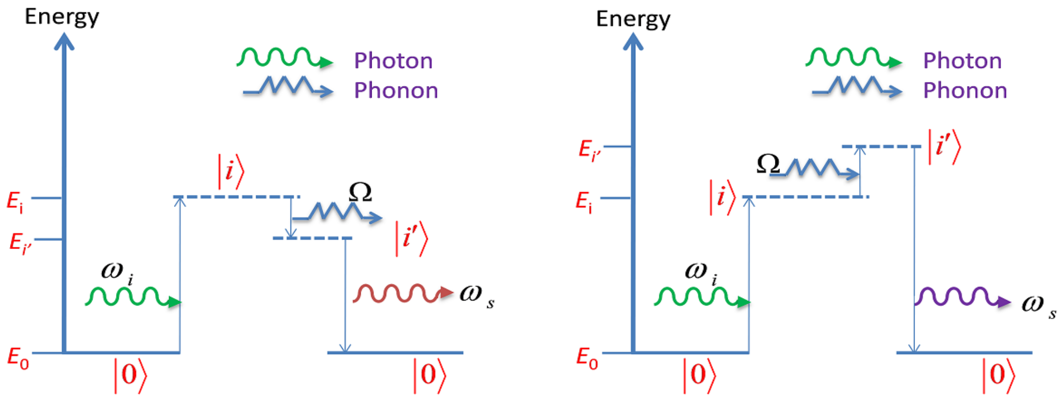

Figure 1-2 - Schematic diagram of the energy states involved in Raman scattering (Left - Stokes process, Right- anti-stokes process)

The standard derivation for the differential cross section (which defines the scattering efficiency) for scattering into the solid angle and frequency increments $d\Theta$ at Θ and $d\omega_s$ at ω_s leads to

$$\frac{\partial^2\sigma}{\partial\Theta\partial\omega_s} = vV\frac{\omega_s^4}{c^4}\left|\hat{e}_s.\Re.\hat{e}_i\right|^2\left\langle UU^*\right\rangle_\omega \tag{1.9}$$

Here $\Re$ is the Raman tensor appropriate to the elementary excitation of amplitude U, $\hat{e}_i$ and $\hat{e}_s$ are the unit polarization vectors of incident and scattered light, v is the interaction volume and V is the sample volume. The notation $\left\langle UU^*\right\rangle_\omega$, denotes the power spectrum of $|U|^2$. Eq. (1.9) separates the cross section into a shape factor $\left\langle UU^*\right\rangle_\omega$, which describes the frequency spectrum of the excitation under study, and a strength factor $\left|\hat{e}_s.\Re.\hat{e}_i\right|^2$, which contains the relevant interactions of light with the elementary excitation through other possible intermediate excitations of the solid. To be more specific, for a one-phonon Stokes process we have[16]

$$\left\langle UU^{\dagger}\right\rangle_{\omega} = \frac{\hbar}{2N\omega_i}(n_i+1)g_i(\omega) \ , \tag{1.10}$$

and

$$\left\langle UU^{\dagger}\right\rangle_{\omega} = \frac{\hbar}{2N\omega_i} n_i g_i(\omega) \ , \tag{1.11}$$

for an anti-stokes process, where N is the number of oscillators in the solid (note that $\partial^2\sigma / \partial\Theta\partial\omega_s$ actually depends on *V/N* not *V*), $n_i = [\exp(\hbar\omega_i / kT) - 1]^{-1}$ is the Bose-Einstein thermal population factor and $g_i(\omega)$ is a line-shape response function, often taken to be a Lorentzian :

$$g_i = \frac{\Gamma_i / 2\pi}{(\omega_i - \omega)^2 + (\Gamma_i / 2)^2} \tag{1.12}$$

For a multiphonon process we must replace $(\mathrm{n}_i + 1)$ in Eq.(1.10) by the appropriate thermal factor [e.g., $(\mathrm{n}_1+1)(\mathrm{n}_2+1)$ for a summation process involving ω_1 and ω_2] and $g_i(\omega)$ is replaced with the multiphonon density of states which generally contains several sharp critical point features.[28,29] The Stokes Raman scattering occurs as a result of photon absorption from the ground state to a virtual state, followed by depopulation to a phonon-excited state. On the other hand, the anti-Stokes Raman scattering is a result of photon absorption from the phonon-excited state to a virtual state, followed by depopulation down to the ground state. As it is obvious from the Boltzmann population factor $e^{\hbar\omega/k_B T}$, the phonon-excited state is less populated than the ground state and hence the anti-Stokes lines must be of a lower intensity than the Stokes lines. From Eqs. (1.8 - 1.11) it can be shown that

$$\frac{I_{Stokes}}{I_{anti-Stokes}}=\left(\frac{\omega_i-\omega}{\omega_i+\omega}\right)^4 e^{\frac{\hbar\omega}{k_B T}} \tag{1.13}$$

So from Eq. (1.13) by measuring the intensity ratio of Stokes and anti-Stokes process, one can determine the local sample temperature.[30] Because of the creation of phonons in the Stokes process and their annihilation in the anti-Stokes process, the anti-Stokes intensity increases while the Stokes intensity decreases with increasing sample temperature. However, Eq. (1.13) cannot be utilized if the excitation frequency is in the vicinity of any resonance of the electronic band structure and thus the material is not optically thin anymore.[31]

From the above discussion it is clear that three major factors contribute to the Raman spectra.

i. **The scattered light frequency**- Since the scattered and the incident light frequency differ very little, in the case of one-phonon processes, scattering intensity can be increased by increasing the laser light frequency. In addition, the susceptibility tensor depends dramatically on the chosen laser light frequency as described in the section above. By varying the incident light frequency this dependence can be used to investigate the inter- and intra-band critical points of the electronic band structure.[16]

ii. **The scattering volume V**. The light penetration depth (*d*) in the material is determined by the absorption coefficient (κ) and the wavelength (λ_i) of the incident light by the relation,

$$d=\frac{\lambda_i}{2\kappa} \tag{1.14}$$

This can be utilized to increase the scattering volume as the light penetration depth generally increases with increasing λ. However, the dependence on the incident light energy, discussed above, behaves in the opposite way. With increasing λ, ω^4 decreases drastically and thus no advantage can be gained.

iii. **Polarization configuration and the crystal symmetry $\hat{e}_s.\Re.\hat{e}_i$:** Depending on the crystal symmetry, the components of the Raman tensors are different. Based on the components of the Raman tensor and with the suitable choice of the polarization, the allowed vibrations in the crystal lattice and their symmetries can be determined. The corresponding Raman tensors are listed elsewhere for the different point groups.[25] The appearance of the Raman active phonon modes depends on the chosen polarization configuration. Due to the nature of the Raman tensor, the occurrence of the longitudinal optical (LO) and transverse optical (TO) phonon modes depends on the choice of the incident and the scattered light polarization and the measurement geometry. The polarization selection rules are listed elsewhere in greater detail.[25,26,32,33]

Considering these three points, the experimental conditions need to be optimised so that the scattering intensity of the interesting phonon features is of maximum intensity. In this thesis, we have used the backscattering measurement geometry without any polarization selection.

1.3 Brillouin Scattering

Brillouin scattering, first predicted by Brillouin,[7] studies the scattering of light from the long-wavelength thermal acoustic wave or spin waves in a solid and from the random thermal density fluctuations in a liquid or gas. The velocity of the acoustic modes propagating inside the materials is determined directly from the Brillouin shift. It is a non-destructive optical probe that provides a variety of information about the acoustic properties of materials namely acoustic sound velocities and attenuation,[34,35] structural relaxation,[36,37] elastic and photo elastic properties,[38-40] stress/strain conditions[41,42] and phase transitions in condensed matter.[43] From the careful analysis of the spectral width, the information about the acoustic attenuation arising from carrier damping, structural relaxation and other possible mechanism can also be determined. Brillouin scattering (optical technique) is complementary to the ultrasound (mechanical) techniques for the study of acoustical properties. In Brillouin scattering, scattering takes place in the hypersonic regime (GHz):

$$10^7\mathrm{s}^{-1} \leq |\Omega| \leq 10^{12}\mathrm{s}^{-1}, \qquad (|\Omega| \ll \omega_i,\ \omega_s) \tag{1.15}$$

and the dispersion $q = q(\Omega)$ is determined by the viscoelastic transport coefficients of the scattering medium. The frequency range is in between ultrasonic and neutron-scattering techniques. But each has some advantages and disadvantages. Brillouin scattering is a non-destructive probe. The incident light, usually a focused laser beam, and the scattered light essentially leave the sample in thermodynamic equilibrium. Unlike ultrasonic techniques, no external forces need to be applied. The thermal acoustic excitations which maintain the state of thermodynamic equilibrium are already present. Brillouin scattering is a powerful tool for investigating the elastic properties of materials. One can perform Brillouin scattering experiments with tiny sample, in extreme physical conditions and of highly reactive or fragile samples. Moreover, using Brillouin scattering technique one can determine optical properties of the materials as well.[44] All these considerations make Brillouin scattering an elegant, effective and non-contact technique to measure the spectral density of acoustic phonons and optical constants of materials. The disadvantages are quite extensive experimental setup, which includes single mode monochromatic laser, the Fabry-Perot interferometer with controller unit and related system and lower accuracy compared to ultrasonic technique.

1.3.1 Brillouin Scattering in solids

The light scattering by acoustic waves in solids can take place both from the surface and bulk of the material under investigation. The mechanism of scattering from surface and bulk acoustic waves is pretty different. The surface acoustic wave scatters light by surface-ripple mechanism which is a dominant factor in the case of opaque material and will be discussed in the following section. The scattering of light by bulk acoustic wave is mediated by the elasto-optic scattering mechanism, in which dynamic fluctuations in strain field brings about fluctuation in the dielectric constant and these in turn translate in the fluctuation in refractive index. The elasto-optic mechanism is the dominate factor in the case of transparent material. The fluctuating optical inhomogeneities results in inelastic scattering of the light as it passes through the solid. The modulation in dielectric constant by the propagating thermal acoustic wave is viewed as a moving diffraction grating by an incident light wave. Therefore, Brillouin scattering can be explained by two concepts, namely, Bragg reflection and Doppler shift. Following the Bragg's law which relates the grating spacing to Bragg's angle, one can consider the wavelength Λ of the acoustic wave as the grating spacing and the scattering angle ($\theta / 2$) as Bragg's angle to get the relation

$$\lambda_I = \frac{\lambda_i}{n_i} = 2\Lambda \sin(\frac{\theta}{2}) \tag{1.16}$$

where λ_I, λ_i and n_i are the wavelength of the light inside the medium, in vacuum and refractive index of the medium , respectively. The moving grating scatters the incident light with a Doppler effect, giving scattered photons with shifted frequency $\Delta\Omega$. Brillouin spectrum gives frequency shift ($\Delta\Omega$) of the thermal phonon and its wavelength Λ from the knowledge of the experimental geometry. The Brillouin shift can be written as

$$\Delta\Omega = \pm 2Vn_i k_i \sin(\theta / 2) \tag{1.17}$$

and for backscattering geometry $\theta = \pi$

$$\Delta\Omega = \pm 2Vn_i k_i \ , \tag{1.18}$$

where V and k_i are the phase velocity of acoustic wave and the wave vector of the incident light, respectively. This phenomenological relationship was first derived by Brillouin. Combining these two Eqs. (1.17, 1.18) one gets

$$\Delta\Omega = \pm \frac{V}{\Lambda} = \pm Vq \ , \tag{1.19}$$

where q is the wavevector of the phonon. The wavelength of the phonon is not infinite even though it is larger than the unit cell dimensions, hence acoustic waves in crystal lattice behave like sound wave in a continuous medium and their properties can be derived by the macroscopic elastic theory.[45] In the long wavelength limit, the polarization and frequencies of the three acoustic modes for a particular q are determined by the stiffness tensor C_{iklm}, through the Eq.s of motion given by,

$$\rho \ddot{u}_i = C_{iklm} \frac{\partial^2 u_m}{\partial x_k \partial x_l} \ , \tag{1.20}$$

where u is the local displacement vector. The elements of the 4th rank stiffness tensor C_{iklm} are the elastic constants. Eq. (1.20) describes the Eq. of motion of the atomic displacement fields in the limit where the crystal structure of the solid is treated as a continuum. Solution of this Eq. is considerably simplified by the restrictions placed on the elastic constants by crystal symmetry.[40] For a given *q*, plane wave solution to Eq. (1.20) can be found, and one gets three modes (two transverse and one longitudinal), usually of mixed polarizations. Only for special directions of *q*, one finds two pure transverse and one pure longitudinal mode. The scattering tensors for any crystal can be computed in terms of the elastic constants and Pockel's coefficient.[40]

In Brillouin scattering, $q \to 0$ limit of the acoustic modes correspond to rigid translation of the crystal as a whole, and cannot perturb the dielectric constant. Since $q \neq 0$, we observe the Brillouin effect and one can't deal with Brillouin scattering in the $q \to 0$ limit. Unlike Raman scattering, Brillouin scattering tensor will depend on the directions of *q* as well as the incident and scattered electric field. Therefore it is necessary to calculate the scattering tensors for every direction of *q*. The general procedure to calculate the scattering tensors with respect to the *q* direction is described below.

The microscopic equation of motion relate to u_i, the local Cartesian components of displacement from the equilibrium position, to the spatial derivatives of u_i and the stiffness tensor C_{iklm}. If we assume plane wave solution in the form

$$u_i = u_i^0 e^{i(q.r-\omega t)} \tag{1.21}$$

Then from Eq. (1.20)

$$\rho V^2 = C_{iklm} q_k q_l u_m^0 \ , \tag{1.22}$$

where q_k, q_l are components of q. For long wavelength acoustic modes $\Omega = Vq$, where V is the appropriate sound velocity. Thus

$$[C_{iklm}\hat{q}_k\hat{q}_l - \rho V^2\delta_{im}]u_m^0 = 0 \, , \tag{1.23}$$

where $\hat{q}_k = q_k / |q|$ is the k-component of unit vector q_k

Eq.(1.23) has non-trivial solutions only if the determinant for the secular equation vanishes:

$$\left|C_{iklm}\hat{q}_k\hat{q}_l - \rho V^2\delta_{im}\right| = 0 \tag{1.24}$$

The elastic constants, i.e. the elements of the 4th rank stiffness tensor C_{iklm}, are usually described using the contracted notation of two indices running from 1 to 6. So we can write them as C_{ij}, where i and j varies from 1 to 6. So Eq. (1.24) can be written in a simplified form as

$$X = \rho V^2 \, , \tag{1.25}$$

where X is the combination of elastic constants (C_{ij}) depending on the direction of propagation of the phonon with respect to the crystallographic axis and ρ is the density. In Brillouin scattering experiments, one measures sound velocities using the Eq. (1.17) and assuming the refractive index to be known and then solving Eq. (1.24) for getting maximum no of elastic constants allowed by crystal symmetry. For example, in a cubic crystal, a longitudinal phonon propagating along the [110] direction is related to $X = (C_{11}+C_{12}+C_{44})/2$ and the two non-degenerate transverse phonons are related to $X = (C_{11} - C_{12})/2$ and $X = C_{44}$. Therefore, by correctly choosing the geometry of the experiment, it is possible to determine the complete set of elastic constants. An exhaustive table for determining elastic constants (C_{ij}) for various scattering geometry and crystal symmetry is given by Vacher and Boyer. [40]

1.3.2 Brillouin Scattering in Fluids

Brillouin has suggested that light is scattered by thermal sound wave in fluid.[46] These waves are analogous to Debye waves in a crystal. Since sound wave propagation is an adiabatic process, density fluctuations should be decomposed into pressure fluctuations at constant entropy or temperature and entropy or temperature fluctuation at constant pressure. Pressure fluctuation arises when particles with momenta somewhat smaller or larger than the volume-average momentum accumulate in a definite place and at a definite time whereas entropy or temperature fluctuation means that particles with a kinetic energy greater or smaller than the value averaged over the sample have gathered in a certain small region at a certain time. Pressure fluctuation is quite independent of temperature or entropy fluctuations. The light scattered by the fluctuations at constant pressure is not shifted in frequency whereas the frequency of the light scattered by the fluctuations at constant entropy (thermal sound wave or phonons) is shifted by an amount proportional to the velocity of the phonons. Energy and momentum considerations require that the proportionality constant be the magnitude of the change in the wave vector of the scattered light. The two lines are observed because scattering can occur from waves travelling in opposite directions but at the same speed.

The fluctuations in density or entropy vary as function of time leading to fluctuations of the permittivity ($\Delta\epsilon$) or of the refractive index (Δn) ($\epsilon = n^2$) of the medium. The exciting light incident on such a fluctuation is scattered sideways and the field of the scattered light wave is also a function of time. In other words, the time dependence of an optical inhomogeneity leads to modulation of the scattered light. The change in susceptibility associated with the fluctuations of the two independent variables pressure and entropy is given as

$$\delta\chi = \left(\frac{\partial\chi}{\partial P}\right)_S \delta P + \left(\frac{\partial\chi}{\partial S}\right)_P \delta S \tag{1.26}$$

The differential scattering cross section originating from the optical inhomogeneities associated with the fluctuations can be written as[47]

$$\frac{d\sigma}{d\omega} = \frac{\omega_i^4 V k_B T}{16\pi^2 c^4}\left[\beta_s \rho^2 \left(\frac{\partial\chi}{\partial\rho}\right)_s^2 + \frac{T}{\rho C_p}\left(\frac{\partial\chi}{\partial T}\right)_p^2\right]\cos^2\theta \tag{1.27}$$

where V, k_B, T, θ, β_s, ρ and C_P are the scattering volume, Boltzman constant, absolute temperature, scattering angle, adiabatic compressibility, density and heat capacity at constant pressure, respectively. The spectrum of the scattered light consists of three lines. The ratio of the intensity of the central line I_0 to that of the two shifted line $2I_S$ is determined by the thermodynamic fluctuation theory to be[48]

$$\frac{I_0}{2I_S} = \frac{C_P}{C_V} - 1, \tag{1.28}$$

where C_P and C_V are the specific heats at constant pressure and constant volume, respectively. This ratio is known as Landau-Placzek ratio.[48] The calculated linewidth of the central and shifted lines are given by $\Gamma_0 = 2\sigma' q^2$ and $\Gamma_S = 2\alpha' q^2$, respectively, where $\sigma' = \sigma / \rho C_p$ is the thermal diffusivity, σ is the thermal conductivity and α' is the generalized kinematic viscosity and q is the wave vector transfer. The linewidths in both the cases decreases from backscattering to forward scattering direction as a function of $\sin^2(\theta/2)$.[49,50]

1.3.3 Brillouin scattering in opaque materials

Unlike transparent materials, opaque materials are characterized by a complex refractive index $n = \eta + i\kappa$ due to high optical absorption. In the case of opaque materials the intensity of the incident light falls off exponentially inside the medium. Consequently the scattering volume is confined close to the sample surface and it strongly influences the wave vector conservation rule. As the exponentially decayed light field traverses the material, a range of phonon wave vectors q is covered, adding up to the formed spectrum of the scattered light.[44,51] The absorption effect in opaque materials leads to the broadening of the Brillouin peaks in addition to that due to the instrumental, geometry and lifetime broadening of the phonon. For backscattering geometry, two expressions have been used to fit the observed Brillouin peak intensity as a function of wave vector q[44]

$$I_S = \frac{1}{\pi}\frac{\alpha_0}{(\beta_0 - q)^2 + \alpha_0^2} \tag{1.29}$$

where $\beta_0 = 2\omega_i\eta / c$ and $\alpha_0 = 2\omega_i\kappa / c$, ω_i being the angular frequency of the incident light and c being the speed of light. A more appropriate expression was given as follows[51]

$$I_S = \frac{Bq}{(\beta_0^2 + \alpha_0^2 - q^2)^2 + (2q\alpha_0)^2} \tag{1.30}$$

For weakly absorbing material both Eq. (1.29) and (1.30) give identical results but for strongly absorbing sample, Eq. (1.30) is more appropriate. The situation becomes more complicated by the contribution of surface waves of the Rayleigh type to the scattered intensity.[52] Further, the bulk acoustic phonons in opaque materials are also modified by coupling of the longitudinal and transverse polarizations near the surface and cannot be considered independent. As a result of the confinement of the scattering volume near surface in opaque material one must have to take into consideration the surface excitations. Until the advent of high-contrast spectrometer (discussed in Chapter 2) called tandem Fabry-Perot interferometer,[53] the study of opaque materials, namely, surface Brillouin scattering and spin waves in magnetic materials was almost impossible. This advancement in high contrast spectroscopy has been widely used in the last few decades to study the physical properties of thin films, interfaces and multi-layer in opaque materials.

1.4 Kinematics of Light Scattering

The kinematics of inelastic light scattering processes is determined by conservation of energy and momentum. For scattering media with *translational symmetry*, the conservation conditions can be written in terms of the wave vectors and frequencies of the photons and elementary crystal excitations involved in the process. For crystals transparent to the incident and scattered light, with elementary excitations having an infinite lifetime, the conservation of energy and momentum can be written as

$$\omega_i - \omega_s = \pm\omega \tag{1.31}$$

$$k_i - k_s = \pm q \tag{1.32}$$

where ω and q are the frequency and wave vector of the elementary crystal excitation. The plus and minus signs correspond to the Stokes and anti-Stokes processes, respectively. The magnitude of the scattering wave vector is determined by the scattering geometry. The scattering geometry is shown in the vector diagram of Fig. 1-3. In a scattering experiment, we have monochromatic incident light propagating in a direction given by the wave vector k_i.

This light is scattered in all directions, but experimentally, only one direction given by $k_{s,}$ is selected. As indicated by Fig. 1-3, the minimum value of q is obtained in the forward scattering (θ = 0°), maximum for back scattering geometry (θ = 180°) and in isotropic media is given by

$$[n(\omega_i)\omega_i - n(\omega_s)\omega_s]/c \leq q \leq [n(\omega_i)\omega_i + n(\omega_s)\omega_s]/c \tag{1.33}$$

where, n is the refractive index of the medium and c is the velocity of light in vacuum. For visible light scattering, Eq. (1.33) becomes

$$0 \leq q \leq 10^5 \text{ cm}^{-1} \tag{1.34}$$

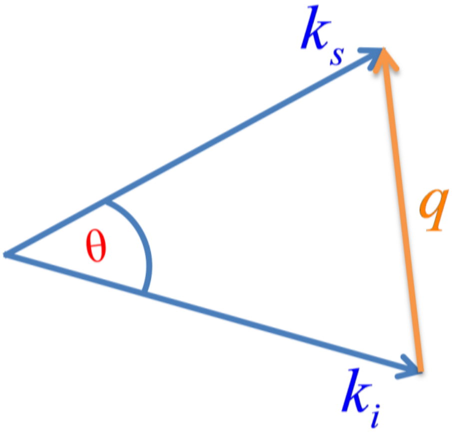

Figure 1-3: Wave vector conservation of the incident and scattered light

This implies that for first-order scattering processes the accessible range of q, under conditions of wave vector conservation, is very small ($q \sim 10^5$ cm^{-1}) compared to the length of the Brillouin zone ($\sim 10^8$ cm^{-1}). So in 1st order inelastic light scattering process one probes the crystal excitations (here phonons) very close (q ~ 0) to the Brillouin zone centre (Γ-point) (see Fig. 1-4). In higher-order processes the individual phonon wave vectors q, can range from zero to the length of the entire Brillouin zone. Eq. (1.15) implies that the frequencies of the incident and scattered light are approximately equal, as are their wave numbers $k_s \approx k_i = k$. Using this, from Fig. 1-3 it is easy to show that

$$q = 2k \sin(\theta / 2) \tag{1.35}$$

As it can be seen from the phonon dispersion relations in Fig. 1-4, the dispersion relation $\Omega_i(q_i)$ is usually flat in the $q \sim 0$ region of interest for the optical phonons.

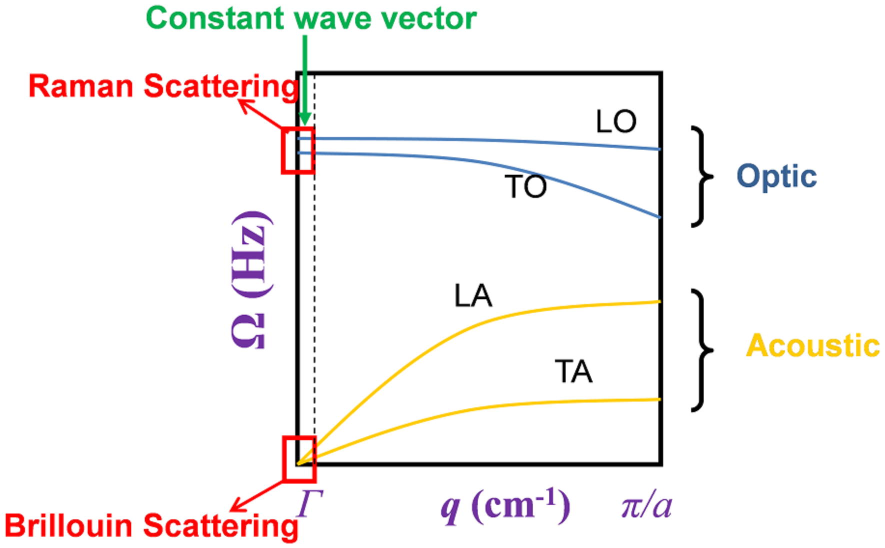

Figure 1-4: Phonon Dispersion relations for a two atom per unit cell crystal

Hence Raman mode frequencies are insensitive to the scattering geometry. However, the acoustic modes show linear dispersion $\Omega = Vq$ in the q ~ 0 region. Thus, by varying the scattering angle θ, one can trace a small part of the dispersion curve $\Omega = \Omega(q)$ with $10^4 \leq q(\theta) \leq 10^5 \mathrm{cm}^{-1}$ using Brillouin scattering.

Eqs. (1.29) and (1.30) have to be modified when the lifetime of the crystal excitations are strongly limited by their decay into other crystal excitations. For example, the optical phonons can be annihilated by decay into two acoustical phonons with opposite quasi momentum. In addition, Eq. (1.30) breaks down in imperfect crystals, in solids lacking translational symmetry (like solid solutions and amorphous solids) and in crystals which are opaque to the incident and scattered light. The cases where violation of conservation of wave vector may occur are

1. *The scattering medium has no translational symmetry.* The absence of translational symmetry allows scattering by modes far away from the Brillouin zone centre. This occurs in crystals with defects, in solid solutions, and in amorphous solids. In Chapter 3, we discuss, one such example, namely, in $Zn_{1-x}Be_xSe$ solid solutions.
2. *The scattering volume is small.* In such cases, the light scattering is due to excitations with wave vectors in a range $\Delta q \sim 2\pi / d$, (where d is a characteristic length in the scattering volume).
3. *The incident and scattered waves are damped inside the scattering volume.* This occurs in metals and small gap semiconductors that are opaque to the light, k_i and k_s are complex in this case.[54]

1.5 Pressure and Temperature Effects on Materials

Pressure and temperature are the two important thermodynamic variables and properties of materials are dependent on them. All applied research consists of studying the temperature and pressure dependence of physical properties of materials with a view of preparing material to exhibit an expected property in a specific condition of thermal (temperature) and mechanical stress (pressure) environment. Materials subjected to a change in these two variables can undergo profound changes including phase transitions of many types. The effect of increasing pressure is specifically to drive the atoms of the material into more closely packed structures with a concomitant increase in the delocalization of valence electrons. Increasing the temperature tends to result in less ordered (higher entropy) structures, the disruption of chemical bonds and ionization. Insight into the nature of these mechanisms is also useful for practical applications. For example, information concerning phase changes in metastable solids can be used to evaluate whether the material with the properties of interest can be synthesized at ambient pressure. The most innovative and prolific practitioner of these two variables is nature, which has for time immemorial created new materials by applying enormous range of pressures and temperatures, to give birth to or destroy stars, to turn graphite into beautiful diamond, as well as to help generate on earth, and may be on other planets, the conditions favourable for life itself. It is thus natural that a primary function of pressure and/or temperature studies is to better understand the world around us. The more appropriate approach of utilizing high pressures and temperatures is not just to better understand the matter in the world around us, but to create entirely new class of technologically interesting materials, many of which certainly do not exist in nature. Success in synthesis of superhard materials, diamond and superconducting materials are a few examples to mention in this direction.[55-57] The application of the variables temperature and pressure to arbitrary mixtures of any or all of the 92 naturally occurring elements allows essentially infinite synthesis possibilities. A third important application of the pressure variable is to use it to vary the electrical, magnetic, superconducting, and other properties of matter in order to test theoretical predictions. High pressure experiments allow a particularly critical test of theory since the variation of a given property can be carried out using only a single parameter, namely, volume.

Pressure is a stronger and cleaner perturbation than the more common thermodynamic variable temperature. For example, in Si a pressure of 10 GPa produces a volume decrease of

5 %, whereas the total temperature induced volume change in Si from 0 K to melting is only 1.8%. For the softer molecular solids this contrast is even greater. Therefore, temperature is more subtle in its effect than pressure. Furthermore, temperature is complicated by the parallel action of thermal expansion (anharmonicity)[58,59] and phonon population effects. In contrast, hydrostatic pressure manifests solely through volume change. In fact, measurements of the pressure dependence at constant temperature and measurements of the temperature dependence at constant pressure allow to determine the anharmonic contributions. In both cases the phonon density of states is a critical parameter, where the temperature affects its population and the pressure changes its form. When the atomic spacing between atoms of a material is changed by 1 to 5% (equivalent to a pressure range of 0 – 20 GPa), the overlap of atomic orbitals which governs the electronic and/or magnetic properties of the material can show drastic changes. This can lead to phase transformations with large changes in the bonds: breaking of sp^3 hybridization, delocalisation of f electrons, metallization of semiconductors, and charge transfer between intramolecular and intermolecular bonds are some examples.[60]

The frequencies of phonon modes in solids are sensitive to changes in applied pressure/temperature as a result of the volume and structural dependence of interatomic or intermolecular forces in the material. Inelastic light scattering can thus be used to probe structural properties of solids at high pressures and to identify pressure induced phase transitions. If pressure and/or temperature cause a phase transition involving a change in point group symmetry, the Raman selection rules will also change. In general this is manifested through the appearance of new features in the observed spectra as forbidden excitations become Raman active or degeneracies are lifted. At the same time, the variations of the half-width of Raman bands under the effect of temperature or pressure are attributed to the decay of a given phonon into two or three phonons.

1.5.1 Pressure Units

Pressure is defined as force per unit area. One atmospheric pressure (atm) is defined as the force exerted on a unit surface at sea level by the weight of the air above that surface. It is equal to the pressure exerted by 760 mm column of Hg. The SI unit of pressure is Pascal (Pa) and is defined as 1 Pa = 1 N/m^2. There is another practical unit of pressure called bar given as 1 bar = 10^5 Pa = 10^6 dynes / cm^2 (1 atm = 1.01325 bar). In high pressure literature, MPa (10^6 Pa) and GPa (10^9 Pa) are generally used. Another commonly used pressure unit is kilobar (1 kbar = 0,1 GPa). It is important to know the extent of pressure experienced in nature. Though the pressure we experience is only 1 bar, pressure experienced in the deepest trench of the ocean (Mariana trench) is about 1.2 kbar and the pressure at the centre of the earth is about 3.6 Mbar. Fig 1-5 shows some known pressure scales in nature and natural phenomena.[61]

When we apply force on a body, we generate *stress* (also defined as force per unit area). Stress (σ_{ij}) is a 2nd rank tensor as shown below. Under certain special conditions, we call the stress as 'hydrostatic pressure' as in the case of "**c**" (see below).

a. Nonhydrostatic **b.** Uniaxial **c.** Hydrostatic

$$\begin{pmatrix} \sigma_{xx} & \sigma_{xy} & \sigma_{xz} \\ \sigma_{yx} & \sigma_{yy} & \sigma_{yz} \\ \sigma_{zx} & \sigma_{zy} & \sigma_{zz} \end{pmatrix} \quad \begin{pmatrix} \sigma_{xx} & 0 & 0 \\ 0 & \sigma_{yy} & 0 \\ 0 & 0 & \sigma_{zz} \end{pmatrix} \quad \begin{pmatrix} \sigma_{xy} & 0 & 0 \\ 0 & \sigma_{yy} & 0 \\ 0 & 0 & \sigma_{zz} \end{pmatrix}$$

$$\sigma_{xx} = \sigma_{yy} \neq \sigma_{zz} \qquad \sigma_{xx} = \sigma_{yy} = \sigma_{zz}$$

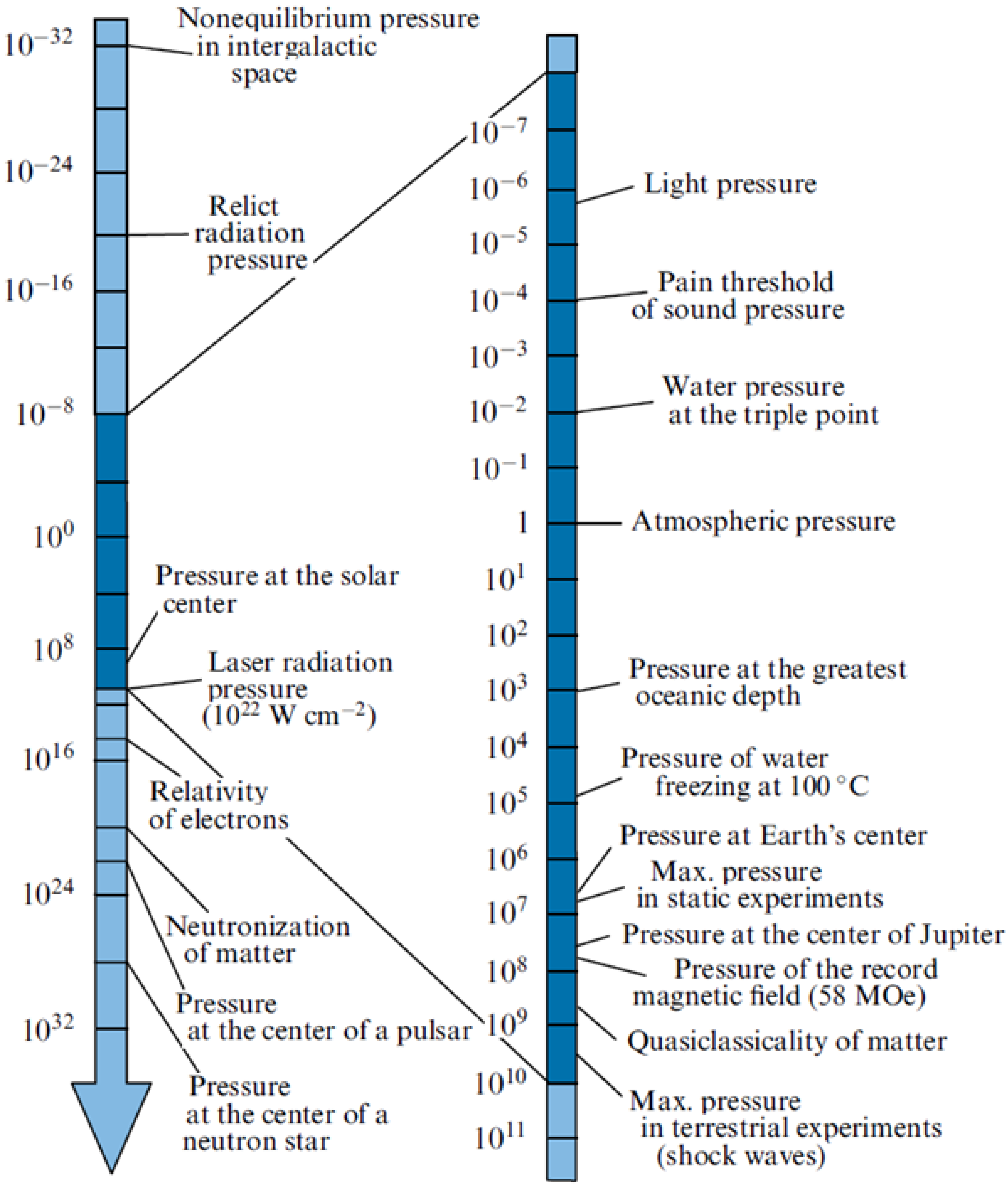

Figure 1-5: The pressure scale range (1 atm = 10^5 Pa) in nature encompasses 64 orders of magnitude. The right-hand side of the scale relates to experimentally attainable conditions

In practice, hydrostatic pressure is achieved by immersing the body in a pressurized fluid medium. The fluid medium also ensures that the load is transmitted slowly.

1.5.2 Methods for Generating High Pressure

Application of pressure on the materials under investigation can be achieved in two ways.

a. **Static method of pressure generation** – Static pressure does not accompany with change in temperature. It does not have any statistical effect associated with temperature and can be achieved using anvil cells, multi anvil cells and piston and cylinder assembly. The most important recent advancement in static high-pressure research has been the development of the diamond anvil cell (DAC).[62] Using DAC, a sample may be subjected to multi megabar pressures, when the two opposing flat parallel faces of diamond anvils are pressed together. Systematic investigations of static high-pressure properties date back to Bridgman[63] and he was awarded with Nobel Prize in 1946.

b. **Dynamic method of pressure generation** – In this method, the change in pressure is always accompanied with change in temperature. This is achieved using shock wave technique. A shock wave is a disturbance propagating at supersonic speed in a material, preceded by an extremely rapid rise in pressure, density and temperature. Although shock waves are irreversible, the process is well understood and can be controlled to produce a desired response.[64,65]

In this thesis, we have applied static pressure of up to about 25 GPa at room temperature using the Diamond Anvil Cell technique in a hydrostatic or quasi-hydrostatic pressure environment. The details of the DAC technique are discussed in Chapter 2.

1.6 References

1. J. Tyndall, Phil. Mag **37,** 384 (1869).
2. L. Rayleigh, Phil. Mag **41,** 447 (1871).
3. G. Mie, Ann. Phys. , Lpz **330,** 377 (1908).
4. A. Einstein, Ann. Phys. , Lpz **338,** 1275 (1910).
5. M. Smoluchowski, Ann. der Phys **330,** 205 (1908).
6. M. Smoluchowski, Phil. Mag **23,** 165 (1912).
7. L. Brillouin, Ann. Phys. (Paris) **17,** 88 (1922).
8. A. Smekal, Die Naturwissenschaften **11,** 873 (1923).
9. C. V. Raman and K. S. Krishnan, Nature **121,** 501 (1928).
10. C. V. Raman, Nature **121,** 619 (1928).
11. C. V. Raman, Indian J. Phys. **2,** 387 (1928).
12. G. S. Landsberg and L. I. Mandelstam, Naturwiss **16,** 557 (1928).
13. E. Gross, Nature **126,** 201 (1930).

14. E. Gross, Nature **126,** 400 (1930).

15. M. Cardona, *Light scattering in solids I: Introductory concepts, Topics in Applied Physics, Vol 8, Springer-Verlag Berlin Heidelberg New York* (1982).

16. M. Cardona and G. Guntherodt, *Light-Scattering in Solids II: Basic Concepts and Instrumentation, Topics in Applied Physics, Vol 50, Springer-Verlag Berlin Heidelberg New York* (1982).

17. M. Cardona and G. Guntherodt, *Light-Scattering in Solids III: Recent Results - Topics in Applied Physics, Vol 51, Springer-Verlag Berlin Heidelberg New York* (1982).

18. M. Cardona and G. Guntherodt, *Light-Scattering in Solids IV: Electronic Scattering, Spin Effects, SERS and Morphic Effects -Topics in Applied Physics, Vol 54, Springer-Verlag Berlin Heidelberg New York* (1984).

19. M. Cardona and G. Guntherodt, *Light-Scattering in Solids V: Superlattices and Other Microstructures -Topics in Applied Physics, Vol 66, Springer-Verlag Berlin Heidelberg New York* (1989).

20. M. Cardona and G. Guntherodt, *Light-Scattering in Solids VI: Recent Results,*

Including High-Tc Superconductivity - Topics in Applied Physics, Vol 68, Springer-Verlag Berlin Heidelberg New York (1991).

21. M. Cardona and G. Guntherodt, *Light-Scattering in Solids VII: Crystal-Field and Magnetic Excitations - Topics in Applied Physics, Vol 75, Springer-Verlag Berlin Heidelberg New York* (1999).
22. M. Cardona and G. Guntherodt, *Light scattering in solids VIII : Fullerenes, semiconductor surfaces, coherent phonons - Topics in Applied Physics, Vol 76, Springer-Verlag Berlin Heidelberg New York* (2000).
23. M. Cardona and R. Merlin, *Light scattering in solids IX - Novel Materials and Techniques, Topics in Applied Physics, Vol 108, Springer-Verlag Berlin Heidelberg* (2006).
24. T. C. Damen, S. P. S. Porto, and B. Tell, Physical Review **142,** 570 (1966).
25. R. Loudon, Advances in Physics **50,** 813 (2001).
26. A. S. Barker and R. Loudon, Reviews of Modern Physics **44,** 18 (1972).
27. R. Loudon, Journal de Physique **26,** 677 (1965).
28. P. A. Temple and C. E. Hathaway, Physical Review B **7,** 3685 (1973).

29. B. A. Weinstein and M. Cardona, Physical Review B **7,** 2545 (1973).

30. M. Balkanski, R. F. Wallis, and E. Haro, Physical Review B **28,** 1928 (1983).

31. H. Herchen, M. A. Cappelli, M. I. Landstrass, M. A. Plano, and M. D. Moyer, Thin Solid Films **212,** 206 (1992).

32. D. W. Feldman, J. Parker, W. J. Choyke, and L. Patrick, Physical Review **170,** 698 (1968).

33. D. W. Feldman, J. H. Parker, W. J. Choyke, and L. Patrick, Physical Review **173,** 787 (1968).

34. G. E. Durand and A. S. Pine, IEEE J. Quantum Electron. **4,** 525 (1968).

35. I. L. Fabelinskii, *Molecular Scattering of Light, Plenum, New York* (1968).

36. Y. Y. Huang and C. H. Wang, J. Chem. Phys. **62,** 120 (1975).

37. Y. H. Lin and C. H. Wang, The Journal of Chemical Physics **70,** 681 (1979).

38. M. V. Nevitt, S. K. Chan, J. Z. Liu, M. H. Grimsditch, and Y. Fang, Physica B+C **150,** 230 (1988).

39. A. Polian, Journal of Raman Spectroscopy **34,** 633 (2003).

40. R. Vacher and L. Boyer, Physical Review B **6,** 639 (1972).

41. T. Sakurai, T. Matsuoka, S. Koda, and H. Nomura, Journal of Applied Polymer Science **76,** 978 (2000).

42. B. C. YAP, S. H. I. R. SHICHIJYO, K. A. Z. U. MATSUSHIGE, and T. E. T. U. TAKEMURA, Jpn J Appl Phys Part 2 **V 21,** 523 (1982).

43. A. Yoshihara, J. C. Burr, S. M. Mudare, E. R. Bernstein, and J. C. Raich, The Journal of Chemical Physics **80,** 3816 (1984).

44. J. R. Sandercock, Physical Review Letters **28,** 237 (1972).

45. L. Landau and E. M. Lifshitz, *Electrodynamics of Continuous Media, Addison-Wesley* (1960).

46. L. Brillouin, Ann. Phys. (Paris) **17,** 88 (1922).

47. H. Z. Cummins and R. W. Gammon, Journal of Chemical Physics **44,** 2785 (1966).

48. L. Landau and G. Placzek, Phys. Z. Sowjun. **5,** 172 (1934).

49. R. D. Mountain, Reviews of Modern Physics **38,** 205 (1966).

50. R. D. Mountain, The Journal of Chemical Physics **44,** 832 (1966).

51. G. Dresselhaus and A. S. Pine, Solid State Communications **16,** 1001 (1975).

52. R. Loudon, Physical Review Letters **40,** 581 (1978).

53. S. M. Lindsay, M. W. Anderson, and J. R. Sandercock, Review of Scientific Instruments **52,** 1478 (1981).

54. R. Zeyher, C. S. Ting, and J. L. Birman, Physical Review B **10,** 1725 (1974).

55. G. Demazeau, Chemica scripta **28,** 21 (1987).

56. Z. Hiroi and M. Takano, Physica C: Superconductivity and its applications **235-240,** 29 (1994).

57. P. F. McMillan, Nature Materials **1,** 19 (2002).

58. H. D. Hochheimer, M. L. Shand, J. E. Potts, R. C. Hanson, and C. T. Walker, Physical Review B **14,** 4630 (1976).

59. P. S. Peercy and B. Morosin, Physical Review B **7,** 2779 (1973).

60. W. B. Holzapfel, Reports on Progress in Physics **59,** 29 (1996).

61. V. E. Fortov, Physics-Uspekhi **52,** 615 (2009).

62. S. Block and G. Piermarini, Physics Today **29,** 44-& (1976).

63. P. W. Bridgman, *The Physics of High Pressures , London: G Bell and Sons* (1958).

64. L. Davison and R. A. Graham, Phys. Rep. **55,** 255 (1979).

65. W. J. Nellis, *High Pressure Measurement Techniques , G N Peggs (ed), London: Applied Science Publishers* (1983), p. 68.

Chapter 2[*]

Experimental Techniques

---

[*] The author's major contribution in this chapter is in designing and fabricating the micro-Raman spectrometer used for all Raman experiments reported in this thesis and gaining a high level of expertise in high pressure technique and Brillouin scattering.

In light-scattering experiments the spectral distribution of the scattered light is analyzed with respect to the spectrum of the incident light. In the case of Raman or Brillouin scattering spectroscopy the changes in the spectrum are very close in energy (~10-1000 cm^{-1} for Raman and ~ 0.1-1 cm^{-1} for Brillouin scattering) to the energy of the incident light but usually many orders of magnitude smaller in intensity. Therefore, a very good suppression is required for the elastically or quasi-elastically scattered light. Monochromators with suitable filters and Fabry – Perot interferometers are used for the analysis of the Raman and Brillouin scattered light, respectively. This chapter describes the main experimental apparatuses used in this thesis to perform the Raman scattering and Brillouin scattering experiments. The methods of doing high pressure and temperature dependent studies are also discussed.

2.1 Raman Spectrometer

Raman scattering being a two photon process is inherently weak (for a strong scattering material one Raman scattered photon can be expected for every 10^7 incident photons).[1] Ever since Raman's experiment,[2] with the invention of laser sources, there have been remarkable change in Raman instrumentation to study very weak as well as low frequency Raman modes in different class of materials including nano materials. [3-10] Especially in the post laser era, the use of laser, modern monochromators and charge coupled device (CCD) as detector, Raman measurements have been relatively simple. However, the cost of the modern commercial Raman spectrometers and the flexibility in using them for experiments in various different conditions has been a matter of concern. In our laboratory, we have fabricated and used various custom built Raman spectrometer for doing different kinds of Raman experiments.[11,12] The Raman investigations reported in this thesis have been possible because of one such custom built micro Raman spectrometer. We have designed an inexpensive, easy to build and high throughput micro-Raman spectrometer which is based on a single monochromator and a CCD detector coupled to a part of a Nikon microscope using a fiber optic cable. Apart from the cost, this particular spectrometer provides enormous flexibility to carry out Raman experiments in ambient as well as in different temperature and pressure conditions with throughputs as good as the commercially available spectrometers. The design, fabrication and working principle of the spectrometer are described below.

2.1.1 Design, Fabrication and performance of the Raman microscope

In order to address the issue of cost, flexibility and versatility in our design of the Raman microscope, we have assembled the collection optics from the parts of a microscope by using the modular focusing unit (LV-IM), double port (Y-IDP), sextuple nosepiece (C-N), universal epi illuminator (LV-U EPI 2), eyepiece lens (CFI 10x) and a trinocular tube (Y-TF2) all from NIKON, Japan. Since the collection optics is not a complete microscope with a sample stage, hence is mounted to the optical table using an L-shaped metal holder fabricated in-house. A simplified schematic of the fabricated micro-Raman spectrometer using this microscope is shown in Fig. 2-1.

The collection optics formed from the parts of a microscope is marked by the dotted area in Fig. 2-1. In this microscope, one of the slots in the dichroic mirror (DM)-cube holder was replaced by a special mirror (SM) designed by us and fabricated by Acexon technologies, Singapore. The special mirror has an Ag coating of 2-3 mm diameter at the

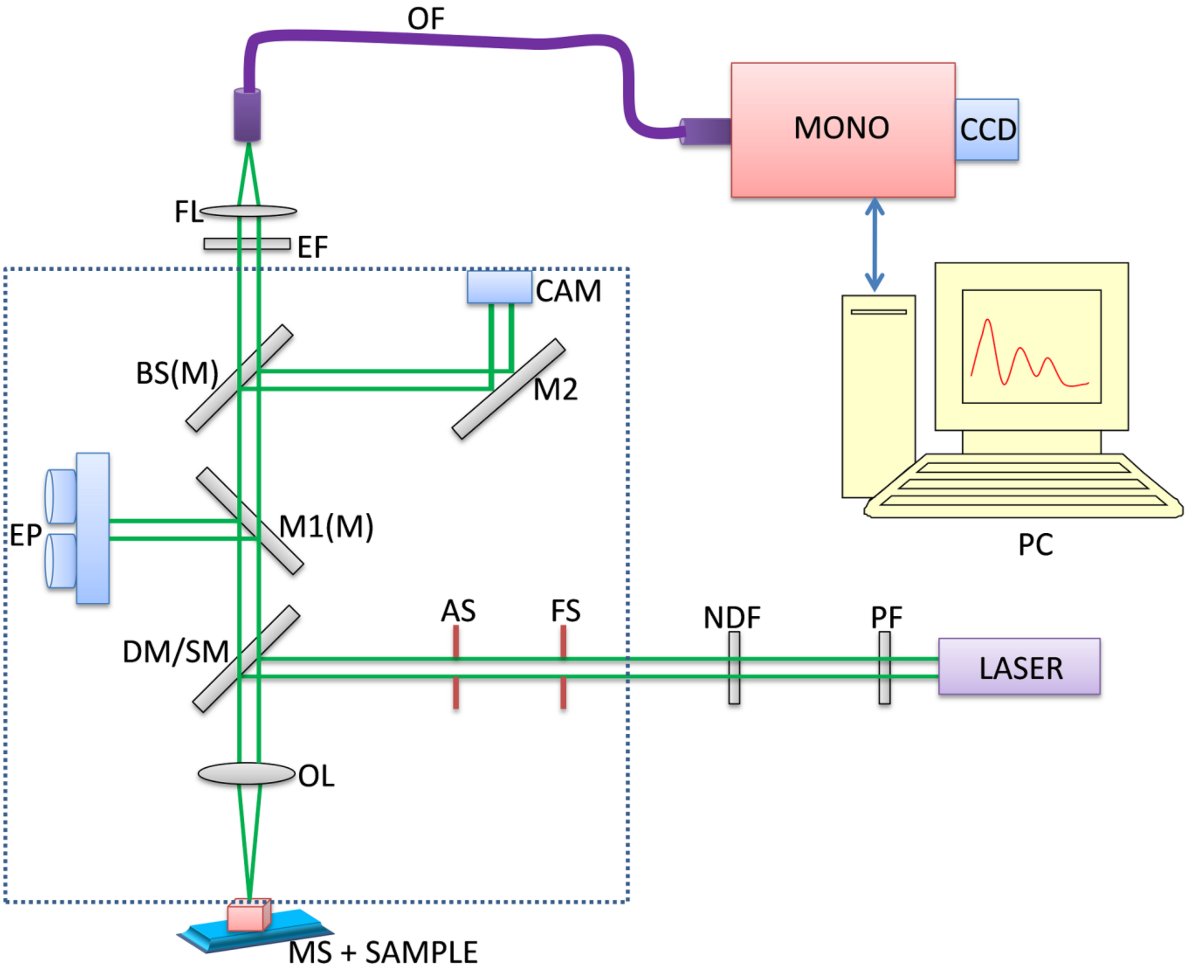

Figure 2-1 : Schematic of the micro- Raman spectrometer: MS- Micro stage; OL- Objective lens, DM – Dichroic mirror, SM- special mirror, AS – Aperture stop, FS – Field stop, NDF - Neutral density filter, PF – Plasma filter, M1 (M) – Movable mirror, EP – Eyepiece, BS (M) – Movable beam splitter, M2 – Mirror, CAM – Camera, EF, Edge filter, FL- Focusing lens, OF- Optical fibre, MONO – Monochromator, CCD - Charge coupled device, PC – personal computer

centre of a 25.2 x 35.6 (±0.2) mm fused silica substrate of 1.1 mm thickness. The silver coating was used to reflect the laser light.The microscope is marked by the dotted area. In this microscope, one of the dichroic mirror (DM)-cube holders was replaced by a special mirror (SM) designed by us and fabricated by Acexon technologies, Singapore. The special mirror has an Ag coating of 1 mm diameter at the centre of a 25.2 x 35.6 (±0.2) mm fused silica substrate of 1.1 mm thickness. The silver coating was used to reflect the laser light. The 532 nm line of a frequency doubled Nd–YAG solid state diode pumped continuous wave laser (model GDLM-5015 L, Photop Suwtech Inc., China) is used as the excitation source. The laser is linearly polarized and power of the laser is ~30 mW. This monochromatic, parallel laser beam is first passed through laser plasma-line filters (PF) (LL01-633-12.5, Semrock) to remove the laser plasma-lines. Since the high power density of the laser can sometimes result in damages of the chemical or structural properties of the sample, the beam then passes through one of several selectable neutral-density filters (NDF). These filters can be moved in and out of the beam path depending on the intensity requirement. Then the beam passes through the open field stop (FS) and the aperture stop (AS) of the microscope and hits the dichroic mirror (DM) or the special mirror (SM) at an angle of 45^{o}. Both AS and FS serve as a guide to the optical path while aligning the laser into the microscope. The reflected laser beam is then directed onto the sample via an infinity corrected microscope objective lens (OL). The typical objective chosen for most of the experiments was an infinity corrected 50X magnification objective with numerical aperture (NA) and working distance (WD) of 0.45 and 17 mm, respectively. (NIKON, L Plan 50X, 0.45 NA, WD 17mm). The revolving sextuple nosepiece provides an option for hosting six objective lenses. Depending on the experimental requirement (depth of focus, working distance, scattering efficiency etc), the choice of the objective can be decided. For example, a long working distance (WD) objective (NIKON L Plan 20X, 0.33 NA, WD 24 mm) has been used for all the high pressure Raman studies in this thesis. Whenever required, the sample and the focused laser spot (with all the NDFs engaged) can be viewed at the eye piece by bringing the movable mirror M1 (M) into the light path. Similarly optical pictures can also be recorded by a camera (CAM) by engaging the movable beam splitter (BS (M)). Mirror M2 directs the beam to the camera (CAM) port. Since the beam splitter splits the beam in 55:45 ratios, it is possible to record a spectrum as well as take a picture simultaneously. Even though, this will cause a 45% loss of Raman signal, it can be used to check if the sudden loss of Raman signal is due to the loss of laser alignment. The reflected and Rayleigh elastically scattered light from the sample together with the inelastically scattered Raman signals are collected by the objective lens and directed onto the edge filter (EF) (LP03-532RS-25, Semrock) which rejects most of the Rayleigh light. The collected light is then focused onto the optical fiber (OF) (200 µm multimode single core optical fiber with a band pass of 400–1000 nm) using an objective lens (NIKON L Plan 20X, 0.33 NA, WD 24 mm), as shown in the Fig. 2-1. The other end of the optical fibre was *f*-number matched to the monochromator (MONO) of focal length: 550 mm (Jobin-Yovn, Triax 550, Instruments SA, Inc., NJ, USA) attached with a liquid nitrogen cooled CCD (Spectrum One) detector. The monochromator (TRIAX 550) includes gratings: holographic 1800 grooves/mm, blazed reflection type 1200 grooves/mm (500 nm blaze) and 900 grooves/mm (450 nm blaze). This allows flexibility in the choice of the gratings for optimum resolution and desired spectral range. The on-axis triple grating turret, allows the TRIAX to maintain on-axis grating rotation during scanning, keeping a constant *f*- number and image quality. The light was focused onto the monochromator through a slit of variable width and dispersed by the motorized diffraction grating onto the CCD via a shutter. Before starting any experiment, the CCD was always liquid nitrogen cooled to reduce the dark counts and to improve the signal to noise ratio. The CCD has rectangular two-dimensional array (1024 x 128) of pixels. A personal computer running the Spectramax software program controls the data acquisition aspects of the spectrometer. Using the software the user chooses the desired grating and can also set the slit width, spectral range for the spectrum (determined by the angle of the diffraction grating), the exposure time of the CCD (controlled by the shutter) and the pixels used on the CCD for data collection. In this thesis, we have always used the grating with 1800 grooves/mm with the input slit width of 100 µm. This provides us a resolution of ~2 cm^{-1}.

As discussed in the beginning, this particular microscope doesn't include any sample stage. So the area under the objective lens is absolutely free for use of different types of experimental setup. We use micrometer stages (MS) on which we place samples on a microscope slide for spectral acquisition at ambient conditions and focusing is done by the vertical movement of the stage. This also provides us tremendous flexibility and allows us to place our temperature controller, diamond anvil cell (DAC) on this micrometer stages to do in-situ Raman measurements in different conditions of temperature or pressure, respectively. Fig. 2-2 shows a picture of the fabricated micro-Raman spectrometer.

Fig. 2-3 shows the room temperature first-order Raman spectra[13] of crystalline silicon at ~ 520 cm^{-1} recorded using the fabricated Raman microscope. The excitation energy (2.33 eV) used in our Raman measurements is always greater than the band-gap energy of silicon (1.1 eV) so the laser light is strongly absorbed in the top layer of a silicon wafer. The spectra was collected using a 50X (NA = .80) objective. The input slit width was 200 µm and the 1800 grooves/mm grating was used. The laser power at the sample was 15 mW. As it can be seen, a very high throughput (~16, 000 counts/second) is achieved. At ambient conditions, a typical spectral acquisition time was 1-2 minutes, for most of the spectrum reported later.

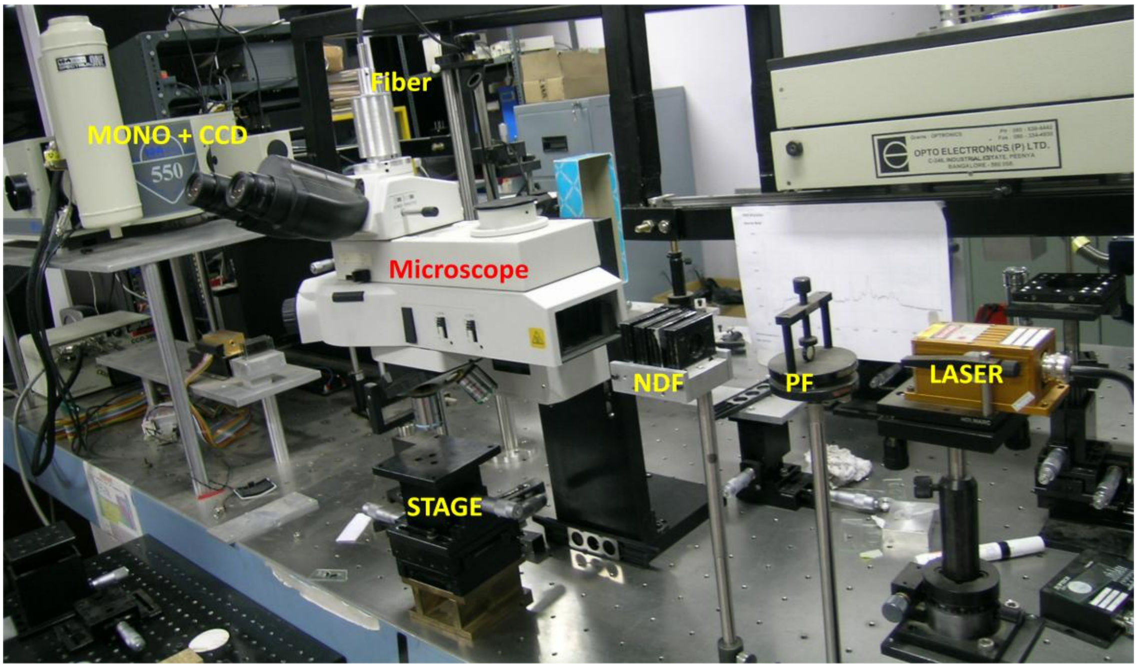

Figure 2-2 : Photograph of the Fabricated Raman spectrometer.

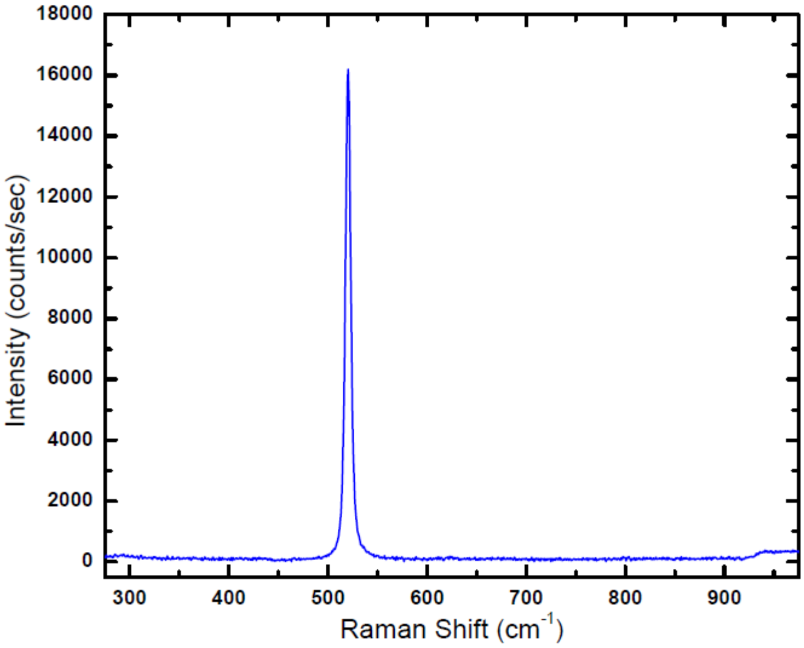

Figure 2-3: Raman spectra of silicon.

The silicon wafer proved to be invaluable in the aligning of spectrometer optics on some occasion. The same piece of silicon wafer was always used for the purpose of quick calibration check. Another quick method of calibration is to check the peak arising due to emission line of mercury that occurs at 546.074 nm. This can be easily achieved by taking spectra with the room lights (mercury fluorescent tube) on. The accurate and exact calibration is always done using the emission lines of neon.[14]

This spectrometer has some disadvantages. The use of edge filters (EF) does not permit the recording of the anti-Stokes part of the Raman spectrum. Furthermore, Rayleigh cut off frequency in these edge filters is large (>80 cm^{-1}). So observing very low frequency modes is sometimes a problem. This problem can be circumvented by using a notch filter. In this set up we have used both special mirror (SM) and a dichroic mirror (DM535, NIKON) to reflect the laser light into the microscope objective. The use of dichroic mirror gives better throughput, but larger Rayleigh background at very low Raman shifts.

2.2 Brillouin Spectrometer

In a typical Brillouin scattering experiment one measures acoustic phonon frequencies in the range 1-150 GHz. A grating based spectrometer cannot separate out this extremely small frequency shift from the huge elastically scattered component. So a high resolution, high contrast and good throughput spectrometer is required. The Fabry-Perot interferometer (FPI)[15,16] as a scanning spectrometer can be used to achieve this goal and is the heart of a Brillouin spectrometer.[17-21] The Brillouin spectrometer unlike a Raman spectrometer has the entrance and exit pinholes instead of slits and a Fabry-Perot Interferometer instead of dispersion grating. Pinholes reduce the stray light entering the spectrometer and increase the light-gathering power of the interferometer. The use of pinholes helps the imaging tolerances on the lenses; the lenses; hence simple planoconvex achromats can be used. The details of the FPI are discussed below.

2.2.1 The Fabry-Perot interferometer

The Fabry-Perot interferometer is used as a scanning spectrometer. In most applications, a plane parallel Fabry-Perot (PFP) interferometer is used. It consists of two very flat mirrors mounted accurately parallel to each other with a spacing L_1 which may be varied. For a given spacing L_1 the interferometer will transmit only certain wavelengths λ_1 as determined by

$$T = \frac{\tau_0}{1 + (4F^2/\pi^2)\sin^2(2\pi L_{1/}/\lambda)} \tag{2.1}$$

where $\tau_0 (< 1)$ is the maximum possible transmission determined by losses in the system, and F, the finesse, is a quality factor depending primarily on the mirror reflectivity and flatness. So according to Eq. (2.1), only those wavelengths satisfying

$$L_1 = \frac{p\lambda_1}{2} \tag{2.2}$$

where p is an integer, will be transmitted. The instrument thus acts as a tunable filter whose peak transmission is close to unity over a narrow spectral interval, falling to a very low value outside this interval. Two incident signals of wavelength λ_1 and $\lambda_1 + \Delta\lambda$ will be simultaneously transmitted (see Fig. 2-4), but in adjacent interference orders, if

$$p\lambda_1 = (p+1)(\lambda_1 + \Delta\lambda) \tag{2.3}$$

This is illustrated in Fig. 2-4.

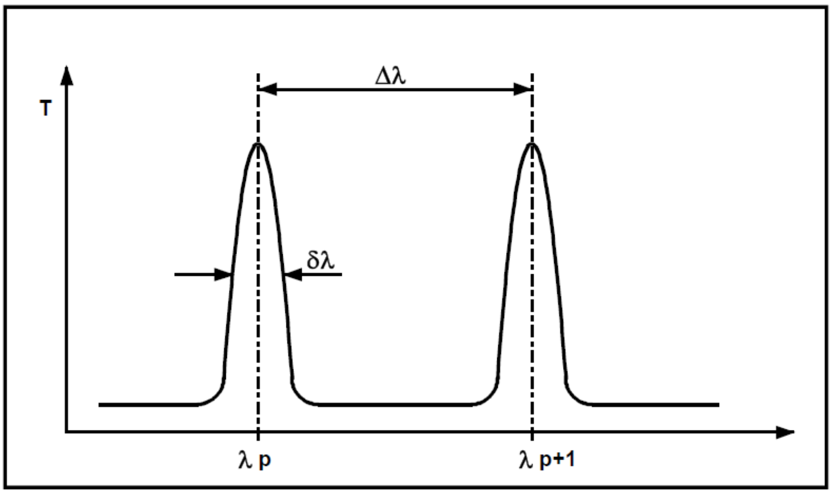

Figure 2-4 : Transmission of a Fabry-Perot interferometer

The finesse F is related to the spacing between successive transmitted wavelengths Δλ (known as the free spectral range, FSR) and the width δλ of a given transmission peak and is given by

$$F = \frac{\Delta\lambda}{\delta\lambda} \tag{2.4}$$

FSR (Δλ) is given by

$$\Delta\lambda = \frac{1}{2L_1} \tag{2.5}$$

The FPI is used as a spectrometer by varying the spacing L_1 so as to scan the light intensity at different wavelengths. However, it is clear that the measured intensity at a given spacing is the sum of the intensities at all wavelengths satisfying Eq. 2.2. The width of the transmission peak determines the resolution of the instrument. The finesse is primarily a function of mirror reflectivity, although instrumental aperture and mirror flatness are also important parameters. In practice, the finesse is limited to values less than about 100 and this places an upper limit on the possible contrast, where the contrast C is the ratio of maximum to minimum transmission given by[22]

$$C = 1 + \frac{4F^2}{\pi^2} \sim \frac{4F^2}{\pi^2} \leq 10^4 \tag{2.6}$$

It is apparent that this contrast will be insufficient for measuring in situations where the elastically scattered component of the scattered light exceeds the intensity of the Brillouin component by more than a factor of 10^4 to 10^5. For backscattering measurements on opaque materials, this is generally the case and it is necessary to increase the spectral contrast. An effective way to increase the spectral contrast is by the multi-pass operation,[23] *i.e.*, by sending back a few times the light through the same interferometer. By this process, the contrast can be increased up to 10^{10}, which is sufficient for most of the Brillouin scattering experiments on opaque materials. Though the contrast is improved by multi-pass technique, there is a problem of interference from neighboring orders, which can be achieved only by extending the FSR. This is done by using two interferometers with unequal mirror spacing are combined to work in a tandem mode as shown in Fig. 2-5.

The first interferometer of spacing L_1 transmits wavelengths

$$\lambda_1 = \frac{2L_1}{m_1} \tag{2.7}$$

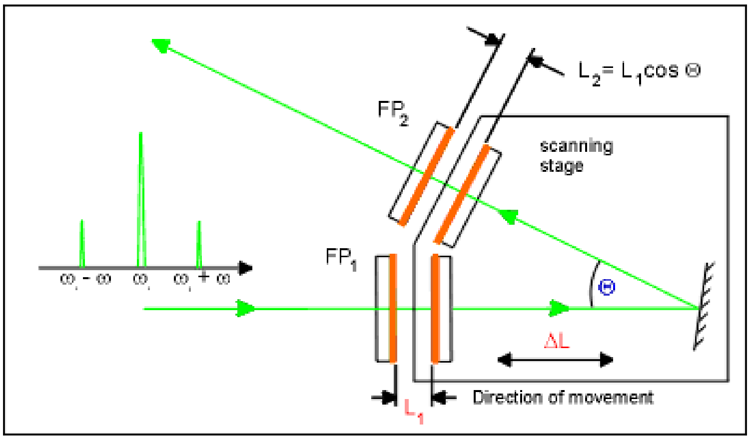

Figure 2-5 : Schematic diagram of an interferometer in tandem opearation

where m_1 is an integer, while the second interferometer of spacing L_2 transmits wavelengths

$$\lambda_2 = \frac{2L_2}{m_2} \tag{2.8}$$

Only if $\lambda_1 = \lambda_2$, light will be transmitted through the combination. The practical limitation in the use of tandem interferometer has been due to the problem of scan synchronization. Thus, to scan the transmitted wavelength, it is necessary to increment the mirror spacing L_1 and L_2 by δL_1 and δL_2 such that.

$$\frac{\delta L_1}{\delta L_2} = \frac{L_1}{L_2} \tag{2.9}$$

In the Sandercock-type interferometer, this condition is achieved by mounting the interferometers on the same scanning stage.[23,24] In one interferometer, the scan direction is kept parallel to the mirror axis, the other one is mounted by little offset with a small angle $\alpha = 18^0$ (see Fig. 2-5). It can be seen that the spacings of the two interferometers satisfy the equation $L_2 = L_1 \cos\theta$.The synchronization condition given by Eq. 2.9 is thus satisfied. In this way it is possible to increase the FSR by a factor of 10 to 20 over that of the single interferometer, although small ghosts remain of the suppressed orders (as shown in Fig. 2-6).

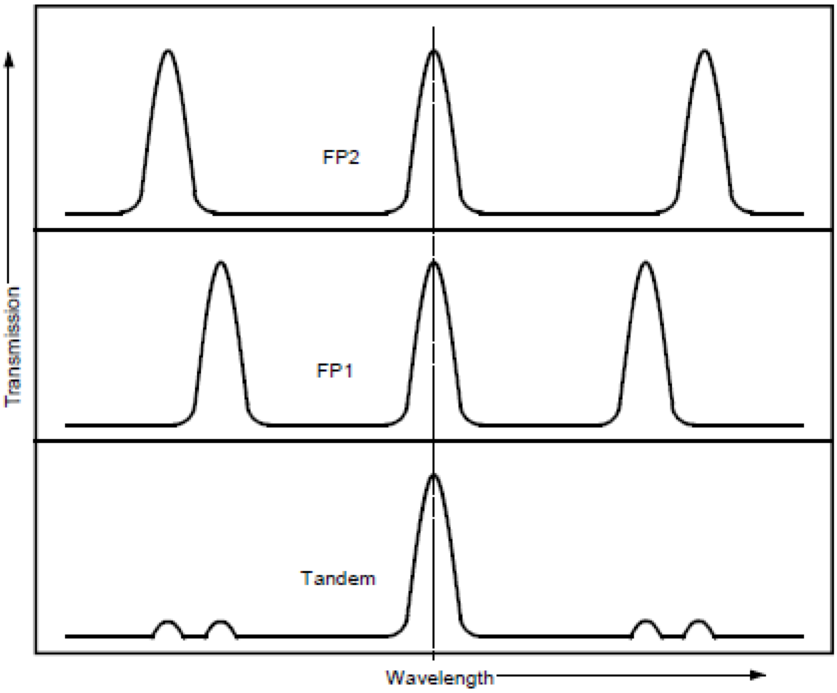

Figure 2-6 : Transmission from a Fabry-Perot interferometer operated in Tandem

2.2.2 Interferometer Construction

A scanning stage[24] consisting of a deformable parallelogram rides on top of a roller translation stage. The former, actuated by a piezoelectric transducer, provides completely tilt-free movement of the interferometer mirror over scan lengths up to 10 μm or more. The latter enables the coarse mirror spacing to be set to the desired value in the range 0-50 mm. The roller translation stage is sufficiently collinear that a movement of several mm leaves the mirrors aligned parallel to better than one fringe across the total mirror diameter. The scanning mirrors of two interferometers are mounted on the same scanning stage; one with the mirror axis parallel to the scan direction, the other offset by an angle θ. A novelty of the construction is the use of a small parallel plate capacitor to measure the scan displacement. The associated electronics produces a voltage accurately proportional to the capacitor spacing, this voltage being used in a feedback loop in order to linearize the scan displacement with respect to the applied scan voltage. The advantages of this construction system are[24]

a. completely tilt-free scan
b. highly linear scan (less than 5Å nonlinearity over $5\text{-}\mu\text{m}$ scan)
c. ability to change mirror spacing without losing alignment
d. stable against temperature change.

In order to scan a Fabry-Perot through a single transmission peak a change in mirror spacing of about $25\,\text{Å}$ is required. It is apparent that any external influence which distorts the mirror spacing by more than a few Å seriously degrades the spectrum. Therefore, the tandem interferometer is mounted on two dynamical vibration isolation systems mounts with feedback control[25]. For correct operation the interferometer must maintain dimensional stability to within a few Å. This is difficult to achieve by purely passive means (e.g., temperature stabilized environment) and the usual procedure is to scan the interferometer rapidly while making continuous corrections to maintain correct mirror spacing and parallelism. A multichannel storage device is used to sum the spectrum over successive scans. In order for a given spectral feature to occur always at the same point in the scan, a small correction is made to the scan voltage offset. The mirror parallelness and correct relative spacing for synchronization are maintained by making small alignment corrections so that a dominant spectral feature has either maximum amplitude or, equivalently, minimum linewidth. The above mentioned corrections are performed automatically in a feedback loop. Fig. 2-7 shows a lay out of a Brillouin spectrometer.

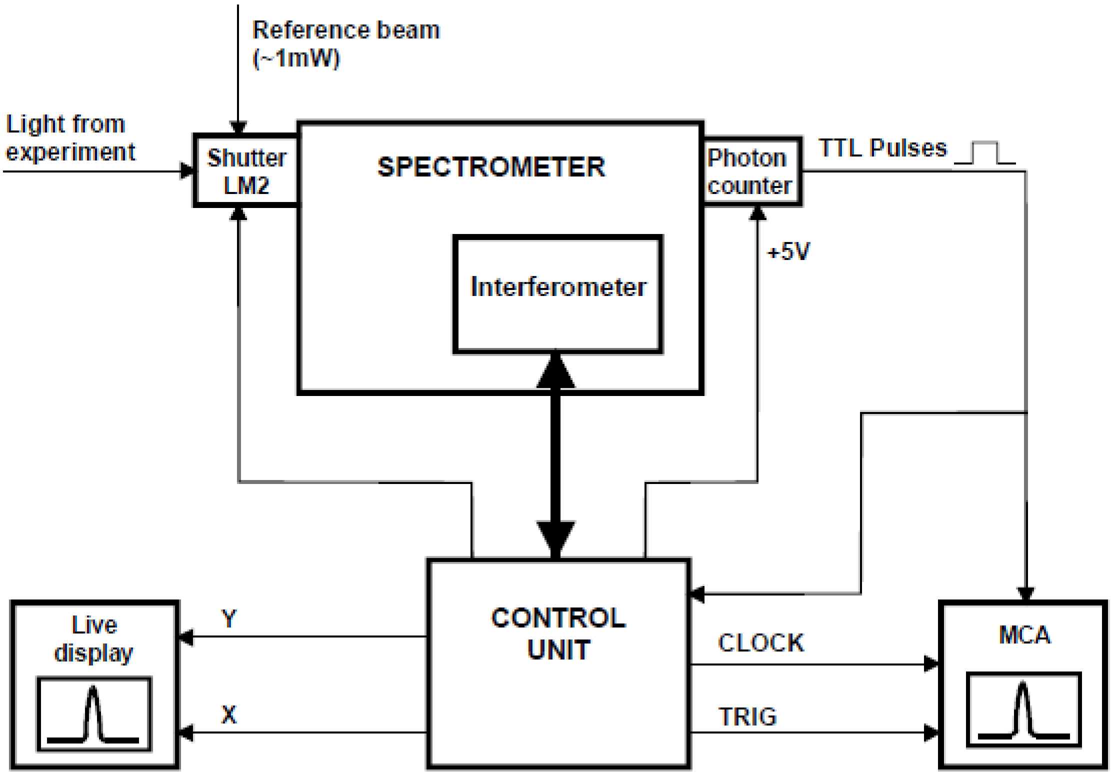

Figure 2-7: Lay out of the Brillouin spectromter.

2.2.3 Alignment of the interferometer

The interferometer is normally used in a multi-pass tandem mode.[19,20,23] The system can only be made to operate in this mode if both interferometers have been pre-aligned parallel and with the correct relative spacing. The procedure described below uses the signal from the measurement photon counter for pre-alignment.

As shown in Fig. 2-8a, light is passed through a beam-splitter onto the first interferometer FP1. The reflected light passes via a second beam-splitter onto FP2 whence the doubly reflected beam is directed to the photo avalanche diode (PAD). The pre-alignment method is based on the fact that when a Fabry-Pérot is transmitting, the reflected intensity tends to zero, a minimum value being obtained when the interferometer is optimally aligned. On scanning the interferometer the photon counter signal will, therefore, show a background intensity punctuated by minima whenever either FP1 or FP2 transmits. This is illustrated for a poorly aligned interferometer in Fig. 2-8b. Two clearly distinct series of peaks are seen. On independently optimizing the alignment of FP1 and FP2 the minima approach zero, as seen in Fig. 2-8c. An adjustment of the relative spacing L_1-L_2 will now bring a pair of peaks into coincidence and the pre-alignment of the tandem interferometer is complete. On switching the optical system back to the multi-pass measurement configuration, transmission will be observed with only minor adjustments necessary to optimize the transmission.

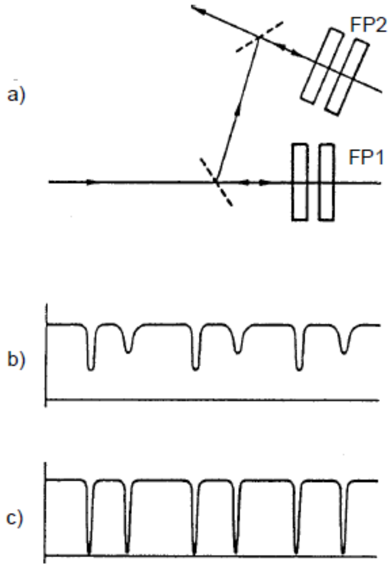

The basic optical system used for achieving alignment in the reflection mode

The measured reflected intensity for two imperfectly aligned interferometers

The intensity after correct alignment but before synchronization

Figure 2-8: Alignment procedure for the interferometer

2.2.4 Stabilizing the interferometer

In order to obtain long time stability of an interferometer it is necessary to apply some form of dynamic control in order to maintain both parallel alignment of the mirrors and correct spacing. Exact means by which this is achieved for a single interferometer is described in depth elsewhere.[20] Four successive scans are required in order to obtain error and correction signals for the two axes X and Y to maintain parallelism in a single interferometer. A tandem interferometer system requires many more scans in order to obtain the appropriate correction signals because now correct alignment involves adjustments about 5 axes, namely X1, Y1, X2, Y2 and ΔZ, where ΔZ is a change in the relative mirror spacing L_1-L_2. Of these alignments the ΔZ axis (synchronization axis) is the most critical and so more time is spent on stabilizing this axis. A Z stabilizer is also employed by the Interferometer Control Unit in order to maintain a peak exactly at the midpoint of the scan.

2.2.5 Detection of the scattered light

The Brillouin signals are very weak. Thus, a single-photon counting detector is necessary to detect such weak signals. For this purpose, a very low-background noise silicon photo avalanche diode (SPCM-AQR-16, Perkin Elmer, Canada) with a quantum efficiency higher than 65% is used in our case. The photodiode is both thermoelectrically cooled and temperature controlled, ensuring stabilized performance despite ambient temperature changes. As each photon is detected, a TTL pulse of 5 Volts is generated and counted using multichannel analyzer (MCA). The MCA (GHOST multi channel analyzer MCA1, JRS Scientific Instruments, Switzerland) is interfaced to a computer and data acquisition is done using the GHOST 6.06 software. In our case the spectra was recorded in 512 channels with a dwell time of 1.5 ms.

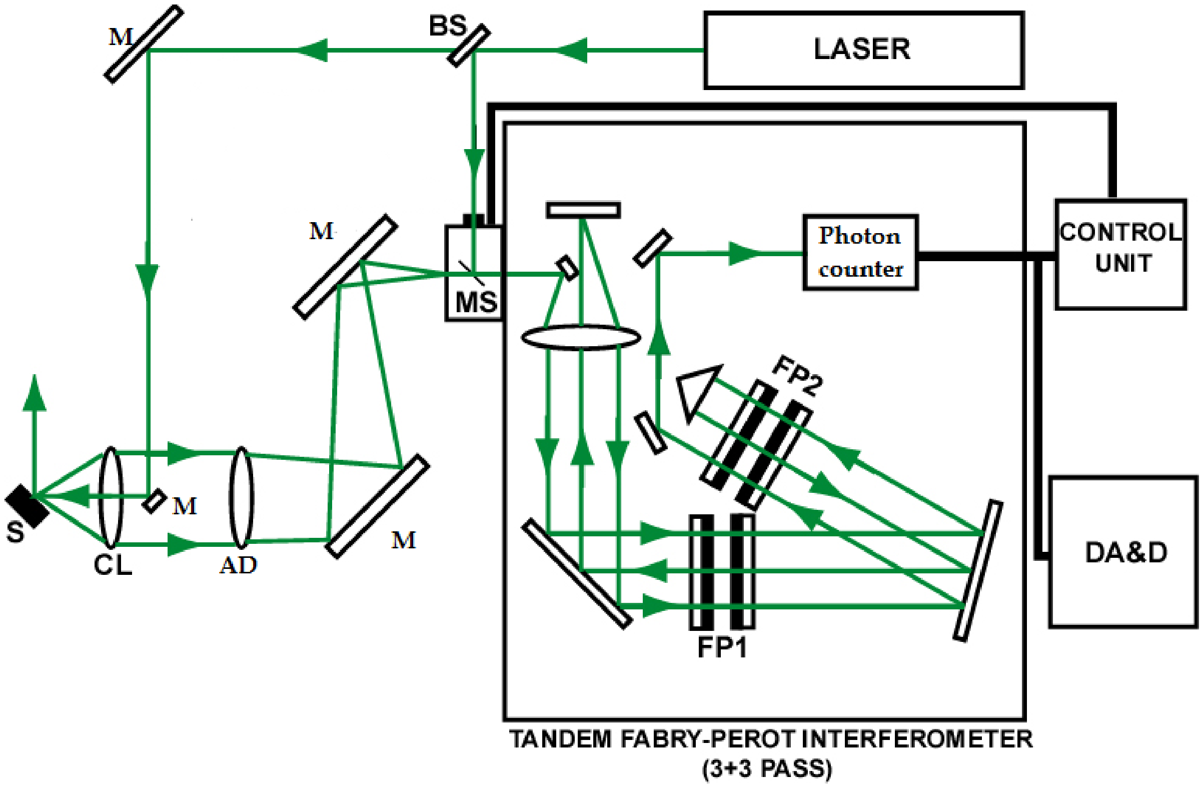

Figure 2-9: Schematic of representation of the experimental setup in the backscattering geometry used for the present study. BS – Beam Splitter, M- Mirror, CL- camera lens, S-Sample, AD – Achromatic doublet, MS- Mechanical shutter, FP1, FP2 – Fabry- Perot etalon pair, DA&D- Data Acquisition and display

2.2.6 180° backscattering geometry

Fig. 2-9 illustrates the 180° backscattering geometry used in the Brillouin scattering experiments in this thesis. The p-polarised 532 nm line of single mode (TEM$_{00}$ solid-state diode pumped frequency doubled Nd:YAG laser (Model COMPASS 315M-150, Coherent Inc., USA) is used as the excitation source and is focused into the sample (S) by means of a long focal length (80 mm) camera lens (CL). The angle between the incident light and the normal to the sample surface is the angle of incidence ($\theta_{\max}$). The focal region defines the interaction region volume ***V*** and the phonon wave vector *q*. The scattered light is collected by the same lens and focused into the input pin hole of the 3+3 pass tandem Fabry-Perot interferometer[20] (JRS Scientific Inc., Switzerland) using an achromatic doublet of focal length 200 mm. Since the lens aperture has a nonzero size, there will be a spread in wave vector k_s, of the scattered light. The total solid angle Ω subtended by the circular aperture of the lens is determined by the maximum acceptance angle $\theta_{\max}$, which is specified by the *f*-number (*f*/#) of the lens: $\theta_{\max} = \tan^{-1}[(1/(2f/\#)]$; *e.g.*, $\theta_{\max}$ = 19.7 for *f*/1.4. Before starting an experiment, depending on the frequency range to be probed (decided by the FSR $\delta\nu = c/2L$), the mirror spacing (*L*) is changed appropriately.

2.3 High Pressure Techniques

The application of pressure as a fundamental thermodynamic parameter for tuning properties of materials has already been discussed in Chapter 1. Here we discuss about the pressure generation and related techniques. The principle of pressure generation is based on the basic definition of pressure

$$P = F/A \tag{2.10}$$

where P is the pressure generated and F is the force applied to an area A. This relation implies that high pressure in an opposed anvil device may be achieved by employing a large force or a small area. Reduction of the effective area of highest pressure between flat faces of anvils is generally the smarter way of achieving higher pressures than simply to increase the force on them. Increasing of the applied force may exceed the compressive strength of the anvils to withstand the stress and would lead to failure of the anvils. Therefore, to achieve hydrostatic high-pressure, anvils with smaller faces are required. This is the basis and underlying reason for the success of the diamond anvil cell.[26-28]

2.3.1 Diamond Anvil Cell

Among all the anvil materials used so far the most widely known high-pressure research equipment today is the diamond anvil cell (DAC). This is because diamond is recognized as the hardest and least compressible material, has the important property of being transparent to the most of the spectrum of electromagnetic radiation, including γ-ray, X-ray, visible light and most of the infrared and ultraviolet region. These radiations provide probes for a wide range of properties for materials *in-situ* at high-pressures. The DAC thus provided the first opportunity for high-pressure researchers to observe visually the effects of pressure, and it allowed convenient access for many kinds of experimental techniques, notably x-ray, gamma-ray (Mössbauer spectroscopy), Raman spectroscopy and other optical spectroscopies.[29,30] Fig. 2-10 gives a schematic diagram of a diamond anvil mechanism. DAC is based upon the opposed diamond configuration, in which a sample is placed between the polished culets of two diamonds and is contained on the side by a metal gasket. In this configuration, very little force is required to create extremely large pressures in the sample chamber. The different kinds in the design of the DAC arise mostly from the differences in the mechanisms for generating force and for anvil alignment and can be classified into five major types of DACs. [31-35]

1. NBS Cell
2. Basset Cell
3. Mao-Bell Cell
4. Syassen-Holzapfel Cell
5. Merrill-basset Cell

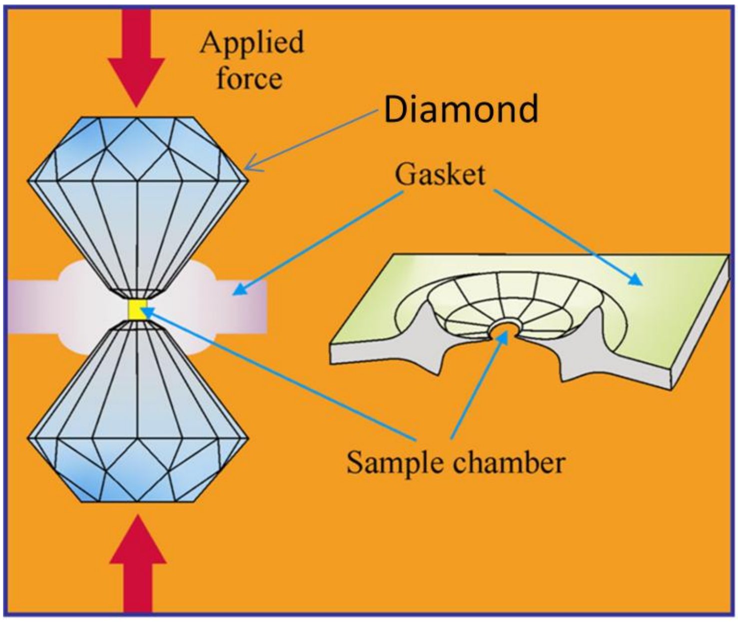

Figure 2-10: - Schematic of a diamond anvil mechanism.

In this thesis work, we have used a Mao-Bell[33] type DAC fabricated in house, for doing the high pressure Raman experiments. A Mao-Bell type piston cylinder DAC with a 1:6 lever arm was used to generate the pressure.

2.3.2 Mao-Bell Diamond Anvil Cell

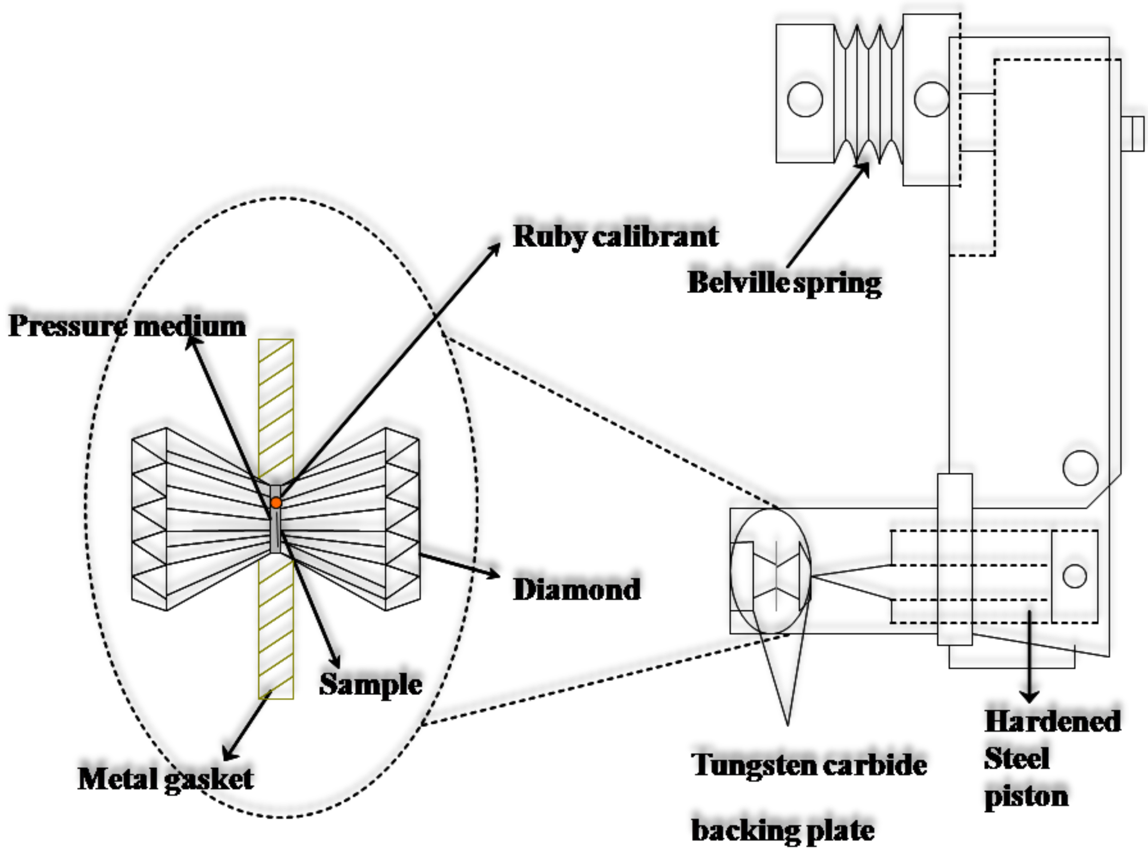

Figure 2-11 : Schematic diagram of the Mao-Bell diamond anvil cell.

Fig. 2-11 shows a schematic of the Mao-Bell DAC used in this thesis. The main components are, a) piston-cylinder assembly, b) diamonds mounted on tungsten carbide rockers, c) hardened stainless steel lever arm based on a nut cracker or scissor mechanism, d) hardened stainless steel gaskets to hold the sample in between the anvils and e) a lead screw with Belleville spring to squeeze the lever. Fig. 2-12 shows a photograph of the DAC that is used for our experiments. On the right side an exploded view of the DAC is shown.

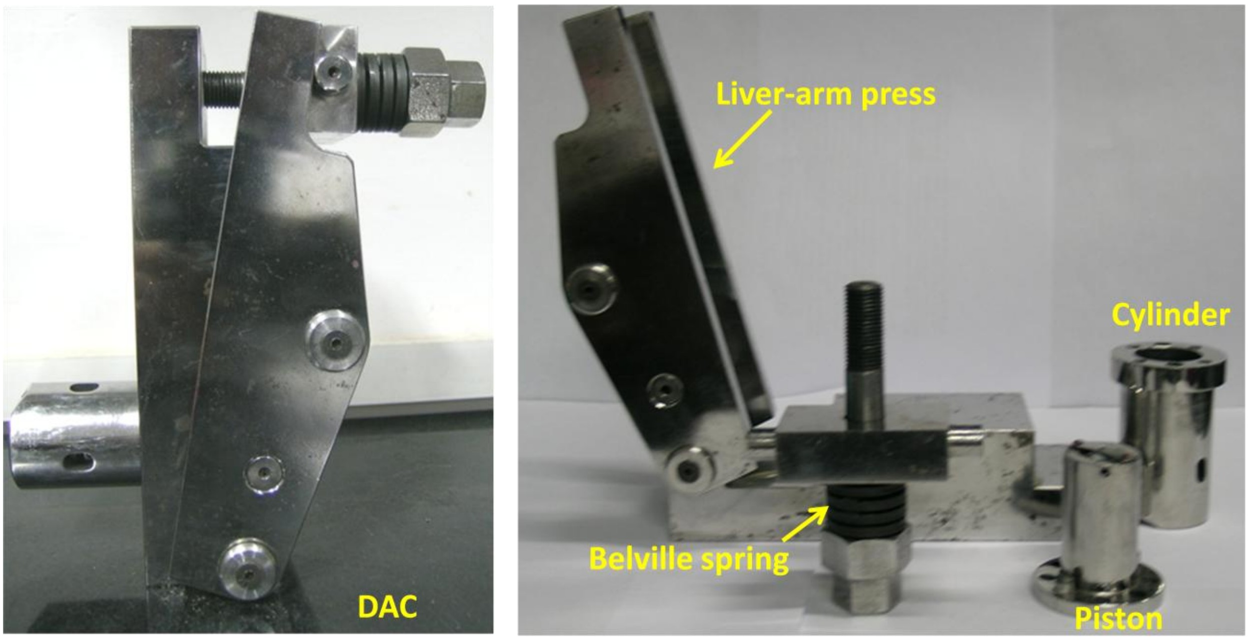

Figure 2-12 Photograph of the DAC used (left) and an exploded view of the DAC (right)

The main factors that determine the maximum pressure generated in a high-pressure cell depend on the type of anvils, the hardness of the material which the cell body and backing plates are made from, gasket material to confine the sample, alignment of the anvils and pressure transmitting medium. Each of these factors is discussed below.

2.3.3 Diamond

The first and foremost step for fabricating an anvil is selecting the appropriate diamond. The four important things to be noted are cut, color, clarity and carat. Gem quality, brilliant cut diamond stones are generally used as anvils. The purest type II diamond is transparent to all electromagnetic radiation and throughout the IR region. However, it is difficult to get and expensive, hence are sparingly used in ultra high pressure. Diamond containing evenly dispersed Nitrogen platelet impurity (type I) is commonly used, but has very strong absorption in the mid IR region. Diamonds with large culet diameter are generally limited to lower pressure and diamonds with small culet diameter are needed for pressures in the megabar regime. An approximate formula to calculate the maximum attainable pressure ($P_{\max}$) that can be achieved using an diamond anvil with culet diameter d is given by[36]

$$P_{\max} = \frac{12.5}{(d(mm))^2} \tag{2.11}$$

The diameter of the table of the diamonds in high-pressure experiments determines the stress applied to the backing plates and thus the maximum attainable pressure. The pressure-bearing culet of the anvil should be much smaller than the table of the anvil to intensify the low-pressure applied to the table for high-pressure generation at the culet. The ratio of the table area to the culet area gives the pressure intensification. The shape of the diamond anvil is important for achieving ultra high pressures.[37]

2.3.4 Backing plates

The material supporting the diamonds is the most important factor after the diamonds for limiting the maximum useful pressure. If the stress in the backing plate exceeds that needed for plastic deformation, then the diamond alignment can be upset resulting diamond breakage. Tungsten carbide and boron carbide materials are usually used for mounting the diamond for the high pressure experiments. These flat metallic plates are provided with tapered holes. The culet of the diamond is centered on the tapered hole of the backing plate. The top surface of the plate is polished well before placing the diamond. The holes of the backing plates for optical and x-ray radiation access behind the diamonds also limit the maximum pressure. They should not have a diameter greater than about one-third of the diameter of the diamond table. These holes are usually cut with a cone angle. Larger cone angles,[38] however, weakens the backing plates to withstand the stress. In order to allow viewing of the anvil faces during alignments, the hole diameter should always be greater than the diameter of the culets of the diamonds.

2.3.5 Diamond alignment

The most important aspect of the DAC for high-pressure experiment is the need for careful alignment of the two high-pressure diamond culets. These two stressed surfaces must be laterally aligned and absolutely parallel to each other during loading to prevent severe gasket deformation and diamond breakage. Different diamond cells need different alignment mechanism depending on their mode of operation and design. For the perfect alignment of our Mao-Bell type DAC, we adopt the following steps strictly. The parallelism of diamond anvils is matched by translation of the rockers along the X and Y axes to position both the culets one above the other. The piston is inserted into the cylinder, and this assembly rested on a V-block, the diamonds is viewed under optical microscope along the four perpendicular directions through the hole in the wall of the cylinder. The gap between the anvil is reduced (but not touched) to estimate the offset of the culets along the X and Y directions. Adjustment is done using the set screws through the ports in the cylinder wall. The process is repeated until the culets are aligned in the X-Y direction. The angular orientation of the culet is adjusted by the screws on the top of the cylinder. The final alignment is obtained by light fringe technique (Newton's ring). For this purpose, the piston is inserted in the cylinder very carefully, so that the diamond culets touch without banging into each other. Using optical microscope, interference fringe pattern is observed through the top of the cylinder. The presence of color fringes or dark striations suggests that the culets are not parallel to each other. Single dark/bright fringe (zero fringe condition) covering the whole cullet confirms that the culets are parallel. Parallelism is achieved by alternatively adjusting the Allen-head screws on the top of the cylinder till the zero fringe condition is achieved. This is the signature of the perfect alignment of DAC. It should be noted that every now and then the X-Y alignment of the culets needs to be checked.

2.3.6 Gasket

Introduction of a gasket in between the anvils is to provide a chamber for the sample confinement and pressure-transmitting medium for hydrostatic pressure distribution throughout the sample chamber. But apart from providing containment for the sample and pressure-transmitting medium, it is proved that the gasket extrudes around the diamonds on compression and acts as a supporting ring for the diamond culets. The commonly used metallic foils are inconel, hardened stainless steel (T-301), tungsten, rhenium and copper-beryllium alloy. It is necessary to pre-indent the gasket before drilling hole for loading the sample into the Diamond anvil cell. Pre-indentation of the gasket work hardens it and will prevent the premature failure of the diamonds and reduces the hole deformation during experiment. There is an equal and opposite force acting inwards between gasket material and the surface of the culet. This is the indication of the stability of the gasket. If the thickness of the gasket is sufficiently small, the destabilizing outward force is smaller than inward stabilizing force, as a result shrinkage of the gasket hole happens. On the other hand, if the thickness of gasket is very large, consequently the outward destabilizing force will be larger than the inward stabilizing force, and hence causes elongation of the gasket hole. It is very important to watch the shape of the gasket hole each time the pressure is changed. If there is asymmetric elongation of the gasket, the experiment should be terminated. We have used stainless steel gaskets of initial thickness of 250 µm which is preindented to a thickness of 70 µm. After the preindentation, using a micro drill equipment with the aid of miniature drill bit, a hole is drilled at the centre of the preindentation area. Fig. 2-13 shows a photograph of a 250 µm hole drilled at the centre of 250 µm thick gasket which was preindented to a thickness of 70 µm.

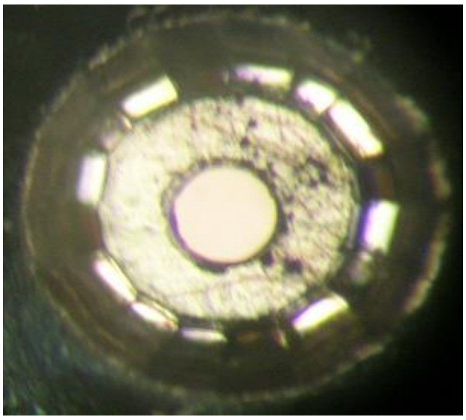

Figure 2-13: A hole drilled in a preindented gasket.

2.3.7 Pressure medium

To achieve hydrostatic pressure[39] (zero shear stress) on the sample, it has to be immersed in a medium. The use of an encapsulating fluid as a pressure transmitting medium generally fulfils this requirement. Various fluids have been reported to be good hydrostatic pressure transmitting media.[39,40] A mixture of 4:1 methanol-ethanol is found to remain hydrostatic up to 10 GPa at room temperature.[41] Addition of a small amount of water in the proportion 16:3:1 methanol-ethanol-water appears to extend the hydrostatic limit of the mixture to 15 GPa.[29] Further increase in pressure beyond the above limits solidifies the fluids but they remain as a very soft solid and nearly hydrostatic even up to a pressure of 20 GPa. Beyond 20 GPa the fluids transform to glass phase with non-hydrostatic properties.[42] Table 1 lists different fluids and their hydrostatic pressure limits. We have used methanol-ethanol-water mixture (16:3:1) as pressure medium in all of our high pressure studies.

TABLE I: Different fluid/ fluid mixtures and their hydrostatic limit.

Pressure medium	**ratio**	**Hydrostaticity at room temperature (GPa)**
Methanol : Ethanol : water	16:3:1	14.5
Methanol : Ethanol	4:1	10.4
Methonol		8.6
Pentane : isopentane	1:1	7
Silver chloride		<7
Water (ice VII)		<7
Sodium chloride		<7
Hydrogen		177
Helium		60 - 70
Neon		16
Argon		9
Xenon		55
Nitrogen		13

2.3.8 Pressure measurement

In static high pressure work using diamond anvils, the ruby fluorescence method is the most widely used pressure calibration technique.[43] Ruby is well suited for pressure sensor in high pressure work because of its strong, sharp R-emission lines. Fluorescence from ruby crystals (5% Cr^{+3}-doped Al_2O_3) is known to exhibit pressure dependence.[44] The R-line luminescence spectrum consists of two sharp lines (R_1, R_2). The R_1 and R_2 lines originate from the splitting of degenerate d-orbitals caused by octohedral distortion due to the oxygen environment around Cr^{3+} ion and spin–orbit coupling. The R lines lie at ~ 694.2 nm (R_1) and ~ 692.7 nm (R_2). The wave length shift of R_1 line is mainly used for pressure calibration under static high pressure.[45] The two R-lines shift equally and no change in $R_1 – R_2$ splitting occurs under hydrostatic pressure. This can be written as[46]

$$\mathrm{P(GPa)} = \frac{1904}{B}\left[\left(1+\frac{\Delta\lambda}{\lambda_0}\right)^{B} - 1\right] \qquad (2.12)$$

where $\Delta\lambda = \lambda_P - \lambda_0$, λ_P is the wavelength at a pressure P and λ_0 is the wavelength at ambient pressure, B = 7.665 and 5 for quasi hydrostatic and non-hydrostatic conditions respectively. The broadening of the spectra from a single ruby chip in static measurements indicates a substantial non-uniformity of stress[44] over the dimension of the ruby chip. In this thesis, ruby fluorescence method has been used for determining the pressure of the samples loaded in the diamond anvil cell. To determine the pressure gradients several small ruby chips were loaded along with the sample and the measurement is taken from the chips in different locations of the hole. At higher pressure, the average of this gives a more accurate pressure value.

2.4 Temperature dependent studies

The low temperature Brillouin scattering experiments (described in Chapter 5) were carried out using a closed cycle helium cryostat (CTI Cryogenics, USA). The temperatures of the sample were maintained with an accuracy of $\pm 1\text{K}$ using a temperature controller (Conductus: model LTC-10, USA) with a silicon diode sensor. To determine the actual temperature of the sample the thermal sensor was kept in contact with the sample on the copper sample holder. The sample was mounted on the copper cold finger using a thermally conducting grease (N-grease) and was immersed in a helium bath inside the cryostat to provide better thermal stability.

The high temperature Raman scattering experiments (described in Chapter 4) were carried out using a heating stage unit (Linkam THMS 600, Linkam Scientific, UK) equipped with a temperature-controller (Linkam TMS 94) The temperature was controlled with an accuracy of $\pm.1\text{K}$. The sample stage (silver block) is electrically heated and a thermocouple monitors the temperature. Sample is placed on the silver block in a quartz crucible. The external control unit (Linkam TMS 94) maintains the set temperature and can also perform ramping up and down of the temperature at user specified rates (up to 30^{o}/min). We have used a ramp rate of 2^{o}/min.

2.5 References

1. W. Hayes, Contemporary Physics **16,** 69 (1975).

2. C. V. Raman and K. S. Krishnan, Nature **121,** 501 (1928).

3. C. D. ALLEMAND, Applied Optics **9,** 1304 (1970).
4. A. Feofanov, S. Sharonov, P. Valisa, E. Da Silva, I. Nabiev, and M. Manfait, Review of Scientific Instruments **66,** 3146 (1995).
5. G. A. Gachko, V. K. Zybel't, L. N. Kivach, S. A. Maskevich, and S. G. Podtynchenko, Journal of Applied Spectroscopy **49,** 1084 (1989).
6. S. Kint, R. H. Elsken, and J. R. Scherer, Applied Spectroscopy **30,** 281 (1976).
7. J. Noh, Y. D. Suh, Y. K. Park, S. M. Jin, S. H. Kim, and S. I. Woo, Review of Scientific Instruments **78,** (2007).
8. W. Rauch, K. Kelbert, and H. Bettermann, Review of Scientific Instruments **59,** 376 (1988).
9. G. Tejeda, J. M. Ferníndez-Sínchez, and S. Montero, Applied Spectroscopy **51,** 265 (1997).
10. G. E. Walrafen, Applied Spectroscopy **29,** 179 (1975).
11. G. Kavitha, S. R. C. Vivek, A. Govindaraj, and C. Narayana, Proceedings of the Indian Academy of Sciences-Chemical Sciences **115,** 689 (2003).
12. G. V. P. Kumar and C. Narayana, Current Science **93,** 778 (2007).

13. J. H. Parker, D. W. Feldman, and M. Ashkin, Physical Review **155,** 712 (1967).

14. S. B. Kim, R. M. Hammaker, and W. G. Fateley, Applied Spectroscopy **40,** 412 (1986).

15. C. Fabry and A. Perot, Ann. Chim. Phys. **12,** 459 (1897).

16. G. Hernandez, Fabry-perot Interferometers, Cambridge University Press, New York, USA (1986).

17. T. Blachowicz, R. Bukowski, and Z. Kleszczewski, Review of Scientific Instruments **67,** 4057 (1996).

18. J. G. Dil, N. C. J. A. van Hijningen, F. van Dorst, and R. M. Aarts, Applied Optics **20,** 1374 (1981).

19. B. Hillebrands, Review of Scientific Instruments **70,** 1589 (1999).

20. R. Mock, B. Hillebrands, and R. Sandercock, Journal of Physics E: Scientific Instruments **20,** 656 (1987).

21. K. Weishaupt, S. H. Anders, R. G. Eberle, and M. Pietralla, Review of Scientific Instruments **68,** 3996 (1997).

22. J. R. Sandercock, Light scattering in solids III, Topics in Applied Physics **51,**

173 (1982).

23. S. M. Lindsay, M. W. Anderson, and J. R. Sandercock, Review of Scientific Instruments **52,** 1478 (1981).
24. S. M. Lindsay and I. W. Shepherd, Review of Scientific Instruments **48,** 1228 (1977).
25. J. R. Sandercock, M. Tgetgel, and E. Meier, R. C. A. Review **46,** 70 (1985).
26. C. E. Weir, E. R. Lippincott, A. Van Valkenburg, and E. N. Bunting, J. Res. Natl. Bur. Stand. **63 A,** 55 (1959).
27. W. A. Bassett, High Pressure Research **29,** CP5 (2009).
28. J. C. Jamieson, A. W. Lawson, and N. D. Nachtrieb, Review of Scientific Instruments **30,** 1016 (1959).
29. A. Jayaraman, Reviews of Modern Physics **55,** 65 (1983).
30. A. Jayaraman and S. K. Sharma, Current Science **74,** 308 (1998).
31. W. A. Bassett, T. Takahash, and P. W. Stook, Review of Scientific Instruments **38,** 37-& (1967).
32. G. Huber, K. Syassen, and W. B. Holzapfel, Physical Review B **15,** 5123

(1977).

33. H. K. Mao and P. M. Bell, Carnegie Inst. Washington Yearbook **77,** 904 (1975).
34. G. J. Piermarini and S. Block, Review of Scientific Instruments **46,** 973 (1975).
35. L. Merrill and W. A. Bassett, Review of Scientific Instruments **45,** 290 (1974).
36. D. J. Dunstan and I. L. Spain, Journal of Physics E: Scientific Instruments **22,** 913 (1989).
37. H. K. Mao and P. M. Bell, Science **200,** 1145 (1978).
38. L. Merrill and W. A. Bassett, Review of Scientific Instruments **45,** 290 (1974).
39. S. J. You, L. C. Chen, and C. Q. Jin, Chinese Physics Letters **26,** (2009).
40. S. Klotz, J. C. Chervin, P. Munsch, and G. Le Marchand, Journal of Physics D-Applied Physics **42,** (2009).
41. G. J. Piermarini, S. Block, and J. D. Barnett, Journal of Applied Physics **44,** 5377 (1973).
42. A. Jayaraman, Review of Scientific Instruments **57,** 1013 (1986).
43. J. D. Barnett, S. Block, and G. J. Piermarini, Review of Scientific Instruments **44,** 1 (1973).

44. R. A. Forman, G. J. Piermarini, J. Dean Barnett, and S. Block, Science **176,** 284 (1972).

45. K. Syassen, High Pressure Research **28,** 75 (2008).

46. H. K. Mao, P. M. Bell, J. W. Shaner, and D. J. Steinberg, Journal of Applied Physics **49,** 3276 (1978).

Chapter 3[*]

High Pressure Raman Scattering Investigations on $Zn_{1-x}Be_xSe$ (x = 0.112, 0.16 and 0.24) Ternary Alloy

A paper based on this work has appeared Physical Review B **81**, 115207 (2010)

---

[*] The author’s main contribution in this chapter is in doing the high pressure Raman experiments, analyzing and interpreting the data. The samples used in this study were grown by Franciszek Firszt (Institute of Physics, N. Copernicus University, Toruń, Poland) and Wojtek Paszkowicz (Institute of Physics, Polish Academy of Sciences, Warsaw, Poland). Theoretical support was provided by Olivier Pagès, Abedalhasan Breidi, Jihane Souhabi, Andrei Viktor Postnikov of Laboratoire de Physique des Milieux Denses – IJB, Université Paul Verlaine, Metz, France.

3.1 Introduction

Wide band gap II–VI compounds are promising for short-wavelength optoelectronic applications in laser diodes and light emitting diodes which display in the spectral region from green to ultraviolet.[1,2] They find potential applications in optoelectronics as these lasers could revolutionize areas such as optical information storage and color displays. Apart from the high-density digital optical storage, other possible applications for the compact blue-green lasers will be in areas ranging from flat panel displays to multicolor printing to medical diagnostics. In this direction, the developments of ZnSe based semiconducting compounds and heterostructures are of particular interest[3,4]. However, devices based on these materials have shorter lifetime compared to III-V based devices due to defect formation favoured by the high ionicity and the smaller bond energies of conventional II-VI materials. Degradation of devices based on these materials because of shorter lifetimes has been a major challenge. The use of Be in ZnSe based mixed crystals (i. e. $Zn_{1-x}Be_xSe$ ternary alloy) has been suggested[5,6] to improve the device lifetime because of dominant covalent bonding and high cohesive energy of BeSe. The high degree of covalent bonding of Be chalcogenides leads to an increase of their shear modulus.[7-9] Therefore, mixing of Be chalcogenides with ZnSe would impart rigidity to the lattice and increase the resistance of the structure to defect generation and propagation. These alloys are especially interesting in the context of the possibility of an additional control of elastic properties, band gap energies, lattice constants as well as conduction and valence band offsets in heterostructures. So they offer more flexibility in controlling the band gap and lattice constant that are matched to different substrates such as GaAs, InP, and Si. The variation of the composition in $Zn_{1-x}Be_xSe$ (ZBS) alloy induces significant changes of the physical properties such as bond polarity, electronic band structure and lattice dynamics.[10,11]

The information on vibrational properties of alloys is crucial in realization of disordered systems and understanding the physical mechanisms governing the alloy formation. Recently, considerable efforts have been put to study of the vibrational properties of $Zn_{1-x}Be_xSe$ ternary alloys.[12-18] A unified understanding of the phonon behaviour of ternary $A_{1-x}B_xC$ semiconductor alloys with tetrahedrally coordinated zincblende (ZB) structure, as observed by Raman scattering and infrared absorption, was achieved within the percolation model.[19] In this model, the crystal is viewed as a composite of the AC- and BC- like regions, where A-C and B-C bonds are more self-connected, each region providing one phonon per bond (1-bond→2-mode) giving rise to the percolation doublet (PD). So this opens the way for a basic understanding beyond that given by the traditional and more crude 1-bond→1-mode 'macroscope' of Chang and Mitra,[20,21] based on a description of an alloy as a uniform continuum via the virtual crystal approximation (VCA). This reveals that phonons provide a natural and deeper insight into the alloy disorder at the unusual mesoscopic scale through the PD acting as a 'mesoscope'. Frequency dependence on any external perturbation of each 1-bond→2-mode mesoscope (AC- and BC-like) can unveil very interesting and useful information regarding the alloy formation mechanism.

The effect of pressure is of fundamental interest in altering the structural, electrical and optical properties of semiconductors. High-pressure studies on semiconductors have led to a basic understanding of their electronic band structure, crystal structure and the role of strains in heterostructures because pressure directly tunes the energy levels and alters the band offset and the strain in the heterostructures. The pressure dependence of the vibrational modes provides additional insight into the nature of the lattice vibrations. Such information is important in characterizing strained-layer superlattices and heterostructures. In view of this, high pressure Raman spectroscopy is a very powerful and popular technique to study the lattice dynamics, electronic structure and phase transition of semiconductor materials related to their structural stability.

In this work, we explore the role of the PD ‘mesoscope’ on the pressure-induced structural phase transition of ternary semiconductor alloys. The aim is to understand whether the dynamics of the AB- and AC-like regions are affected in the same way by pressure (hydrostatic), or one specific region is preferred. An alloy of choice to address such issue is $Zn_{1-x}Be_xSe$ (ZBS) which exhibits large contrast in the physical properties of the constituting bonds/atoms (i.e. bond length, bond force constant, bond ionicity, radii and masses of the substituting atoms, etc.). While ZnSe adopts the usual six-fold coordinated rocksalt (RS) phase under pressure (a metallic one),[22-25] BeSe is one of the few exceptional systems that transforms to the six-fold coordinated hexagonal NiAs structure.[26,27] Furthermore, the BeSe transition pressure (~56 GPa) is much higher than that of ZnSe (~13 GPa). An interesting question then is what happens to weak Be-Se bonds in ZBS when the host Zn-Se bonds undergo their natural ZB→RS transition? We investigate this by taking advantage of the well-resolved Be-Se PD (with splitting Δ ~40 cm^{-1}) ‘mesoscope’ in ZBS. We have performed Raman measurements at increasing pressure up to the ZB→RS transition using a series of alloys with moderate Be content, and attempt to achieve consistent understanding of the observed effects at both the mesoscopic (percolation scheme) and microscopic (*ab initio* calculations) scales.

3.2 Experimental

$Zn_{1-x}Be_xSe$ single crystals were grown by the high-pressure Bridgman method with compositions x = 0.11, 0.16 and 0.24. The composition was determined by high resolution x-ray diffraction (HRXRD) assuming that the lattice parameter of the alloys obeys the Vegard's law. For each sample, a (111)-oriented cleaved piece was polished to a ~25 µm thick platelet and placed together with ruby chips into a 200 µm hole of a stainless steel gasket (pre-indented to 65 µm) inserted between the diamonds of a Mao-Bell type diamond anvil cell. Methanol-ethanol-water (16:3:1) was used as pressure transmitting medium, the pressure being measured via the ruby fluorescence linear scale.[28] Unpolarized Raman spectra were collected in the backscattering geometry on the (111) crystal face using the non-resonant 532.0 nm excitation using a custom built Raman spectrometer (details described in chapter 2). Laser power at the sample was ~15 mW and a typical spectrum acquisition took ~ 2-3 minutes at low pressure. The spectral resolution was 2 cm^{-1}. The spectral profile was fitted using Lorentzian functions after appropriate background correction. In the discussed geometry, both the transverse optical (TO) and longitudinal optical (LO) modes are Raman-active.

3.3 *Ab initio* calculation

Ab initio calculations of the zone-centre (Γ) TO density of states (DOS) at the Brillouin zone-centre (ZC TO-DOS, that compares to Raman spectra) were done with the SIESTA code[29] using a prototype 64-atom supercell that contains the 'ultimate' percolation motif, i.e. a pair of impurities (say A) sitting aside (2-imp. motif) immersed in the environment of the other species (BC-like). The basis of (Zn,Be,Se) pseudopotentials used is taken from Ref. [18] and [19]. After performing the full relaxation of lattice parameters and atomic positions within each supercell, the dynamical matrix was constructed by probing small individual displacements of atom from their equilibrium positions and collecting the forces induced on all sites. The diagonalization of the dynamical matrix yielded the frequencies of TO phonons and the corresponding eigenvectors. A subsequent projection of eigenvectors onto the uniform translation pattern of each species throughout the crystal, as explained in Ref. [19], permits to single out the vibrations of genuinely zone-center character. The correspondingly weighted (and artificially broadened) spectrum of discrete vibration frequencies can then be compared with the TO Raman spectrum. It should be noted that the matrix elements of Raman scattering were not taken into account in the calculation, so that the relative magnitudes of different peaks do not always mimic those in the experiment.

3.4 Results and Discussions

Raman spectra for $Zn_{1-x}Be_xSe$ (x=0.112, 0.16 and 0.24) at ambient conditions of temperature and pressure are shown and assigned in Fig. 3-1. The spectrum looks similar in nature for all three Be concentrations. Pages *et al* have done a detailed and systematic room temperature Raman investigations on these systems using the percolation approach. [12-14,30,31] Hence the origin and behaviour of the various Raman modes is briefly discussed here. We recall that in a crystal AB(C), a transverse (longitudinal) optical TO (LO) mode in the Raman/IR spectra corresponds to vibration of the rigid *A* sublattice against the rigid (B, C)

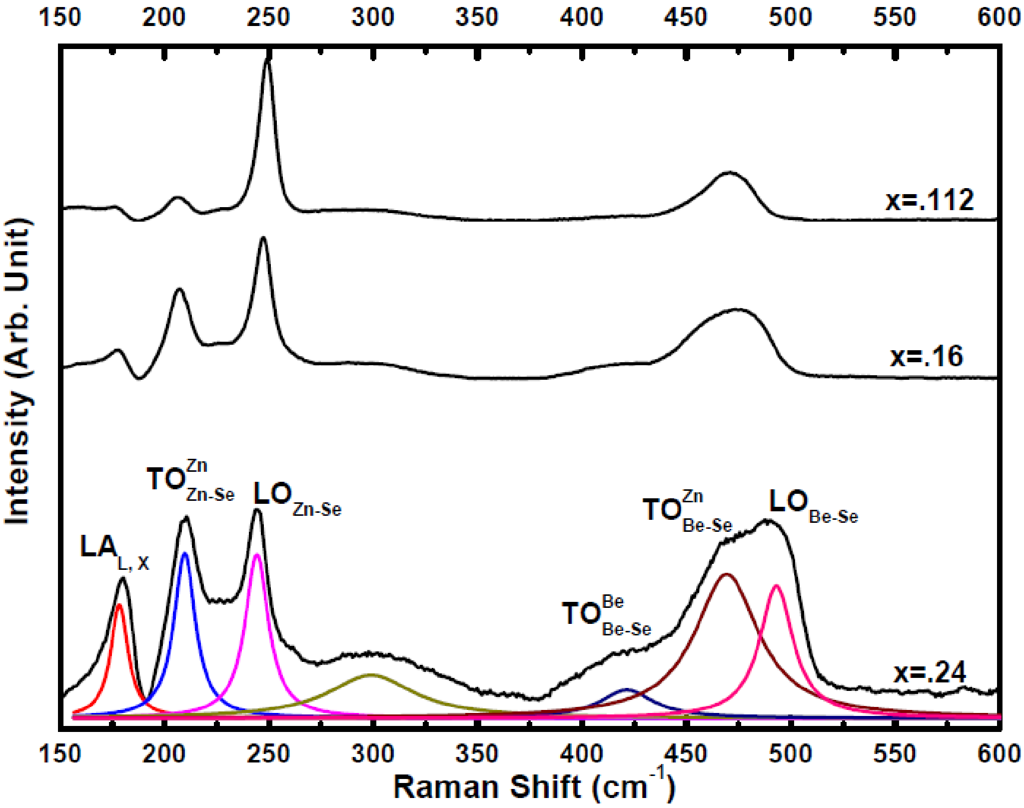

Figure 3-1: Raman spectra of $Zn_{1-x}Be_xSe$ (x = .112, .16 and .24) at ambient conditions of temperature and pressure.

sublattice perpendicular to (along) the direction of propagation. In a polar crystal, a LO mode differs from a TO mode in that it carries a Coulombian field *E* due to the ionicity of the bond. In a pure crystal, this is just responsible for an additional restoring force, with the result that a LO mode occurs at a higher frequency than a TO mode. In an alloy, the Coulombian field *E* is well known to act as a carrier of coherence and the individual modes with close frequencies couple to *E*.

In the percolation model, the crystal is viewed as a composite of the ZnSe (soft) and BeSe (hard)-like regions, where Zn-Se and Be-Se bonds are self-connected, each region providing one phonon per bond (1-bond→2-mode) giving rise to the percolation doublet (PD). A basic rule of the percolation model is that the bonds are longer when they stay in the environment of the short species (thereby vibrating at a lower frequency), and vice versa. With this, the TO modes from the BeSe-like region vibrate at a lower frequency than those from the ZnSe-like region in both the Zn-Se and Be-Se spectral ranges and at any alloy composition. The close LO modes of each percolation doublet couple via their common Coulombian field, building up a unique LO mode (the percolation doublet thus disappears in the LO symmetry), blue-shifted from its native TO basis. So Be-Se TO is bimodal, giving rise to the new mode TO_{Be-Se}^{Zn} in addition to the original TO_{Be-Se}^{Be}. In the labelling of the modes the subscript and superscript refer to the bond species and to the host region, respectively. However, the bimodal response of the Zn-Se region is not very clear due to presence of asymmetry and disorder induced zone-edge modes. This will be discussed in more detail later.

Furthermore, in alloys, the wave vector conservation selection rule is relaxed as a result of the violation of translational invariance, and the first-order Raman peaks correspond to phonons in regions of the Brillouin zone (BZ) where the phonon density of state has a maximum, that is, at the edge of the BZ. Therefore, apart from the zone centre (Γ) modes, $LA_{L,\ X}$ mode assigned as longitudinal acoustical bands at edge L, X of the BZ is also seen. In the discussion we focus on TO modes, because such mechanical vibrations give reliable insight into the individual percolation-type oscillators present in the crystal.[14,19]

Figs. 3-2, 3-3 and 3-4 show the pressure evolution of the Raman spectra at representative pressures for x = 0.112, 0.16 and 0.24, respectively. For the discussion, we focus on intermediate x value (x=0.24), that corresponds to well-resolved Zn-Se and Be-Se Raman signals, but as can be seen that the trends are general in nature. Representative pressure-dependent Raman spectra for x=0.24 are shown in Fig. 3-4. The frequency versus pressure variations of the main features are shown in the inset. A 2TO+1LO percolation-type signal is obvious in the Be-Se spectral range (400–500 cm^{-1}).

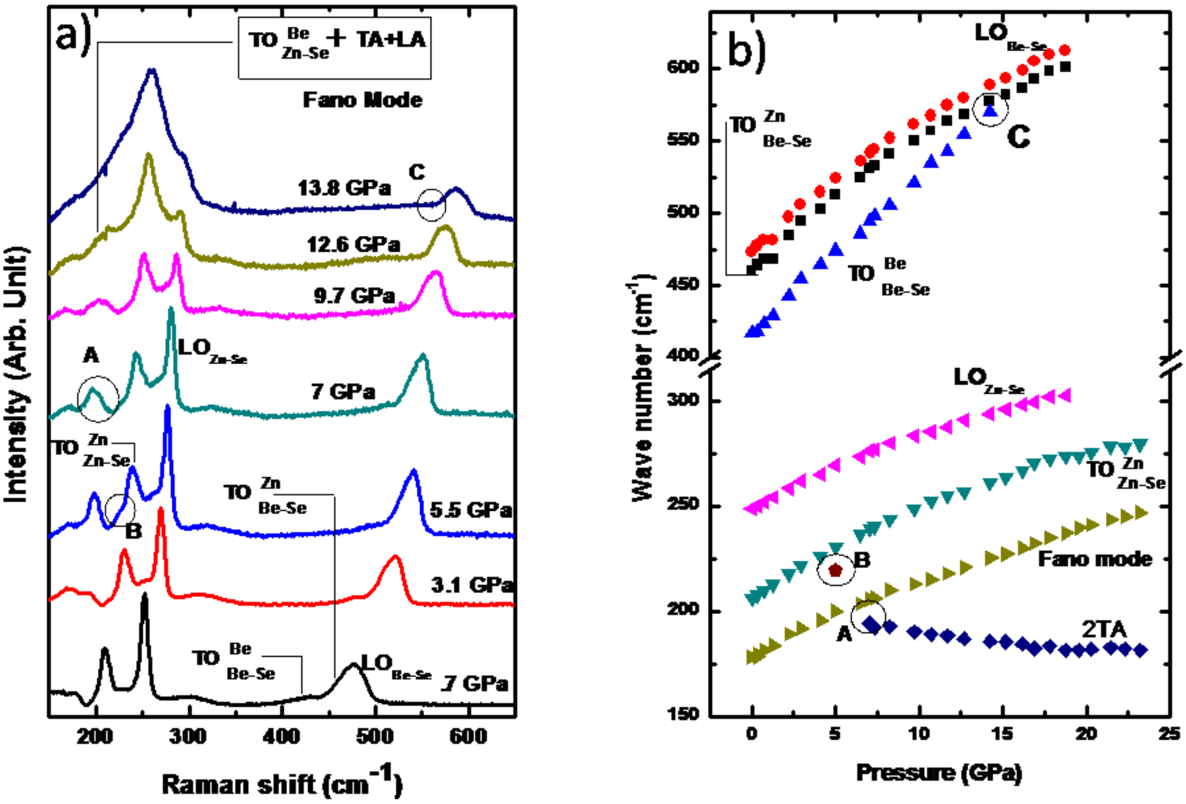

Figure 3-2: a)- Pressure-dependent Raman spectra of Zn$_{0.88}$Be$_{0.112}$Se. b)-The frequency versus pressure variations of the main features are shown in the inset. Remarkable trends (A,B,C) are marked by circles.

The situation is not as clear in the Zn-Se one (~200–250 cm^{-1}). There, many modes coexist, whose number increases with pressure. Initially, a basic 1TO+1LO Zn-Se scheme (Δ~0 cm^{-1}) with additional features was proposed by Pages *et al*. However, the present pressure studies demand greater attention and a more careful assignment (see below).

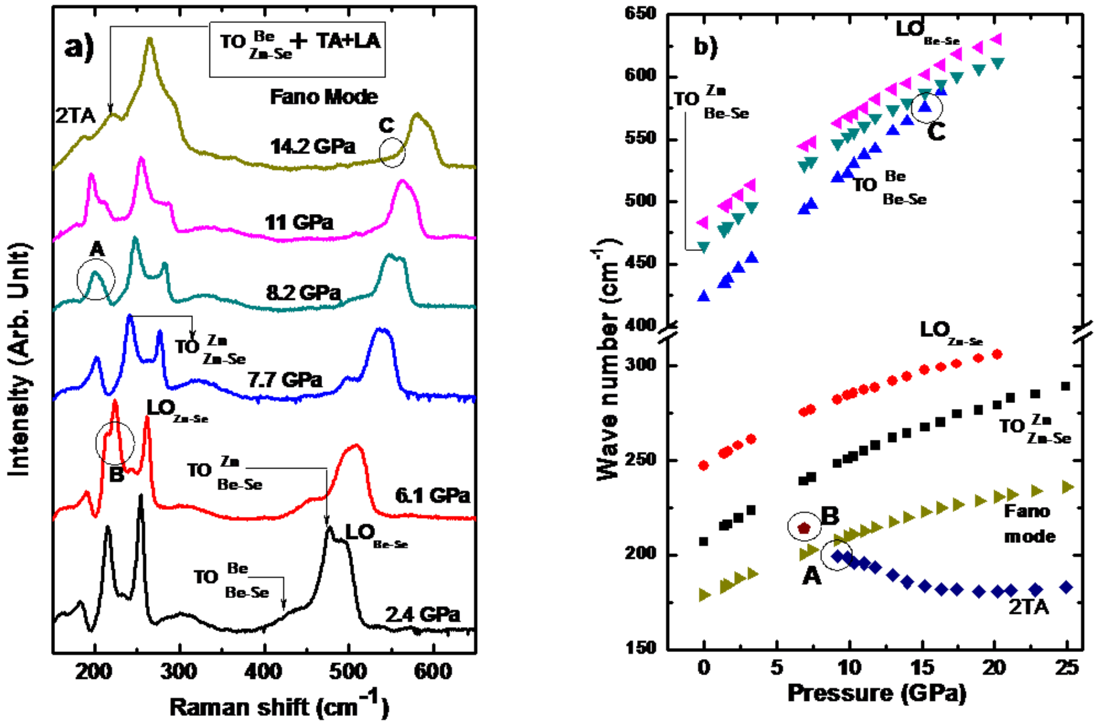

Figure 3-3: a) Pressure-dependent Raman spectra of $Zn_{0.84}Be_{0.16}Se$. b)-The frequency versus pressure variations of the main features are shown in the inset. Remarkable trends (A,B,C) are marked by circles.

By increasing pressure, the LO mode intensity diminishes gradually. The total LO-extinction occurs at ~23 GPa, coinciding with the ZB→RS transition as detected by x-ray diffraction.[32] (not shown). Incidentally, the X-ray diffraction data indicate that the ZB→RS transition is very sharp and that the crystal adopts the RS structure as a whole. Indeed no signal due to a residual ZS phase was detected beyond the transition pressure.[32] More fascinating effects related to TO modes occur as marked by capitals in Fig. 3-4 (similar trend applies for x = .112 and .16, see Figs. 3-2 and 3-3), i.e. the splitting of the lower Zn-Se branch (A), transient appearance of a weak mode in-between the two lower Zn-Se branches (B), and the convergence of the lower Be-Se TO branch onto the upper one (C).

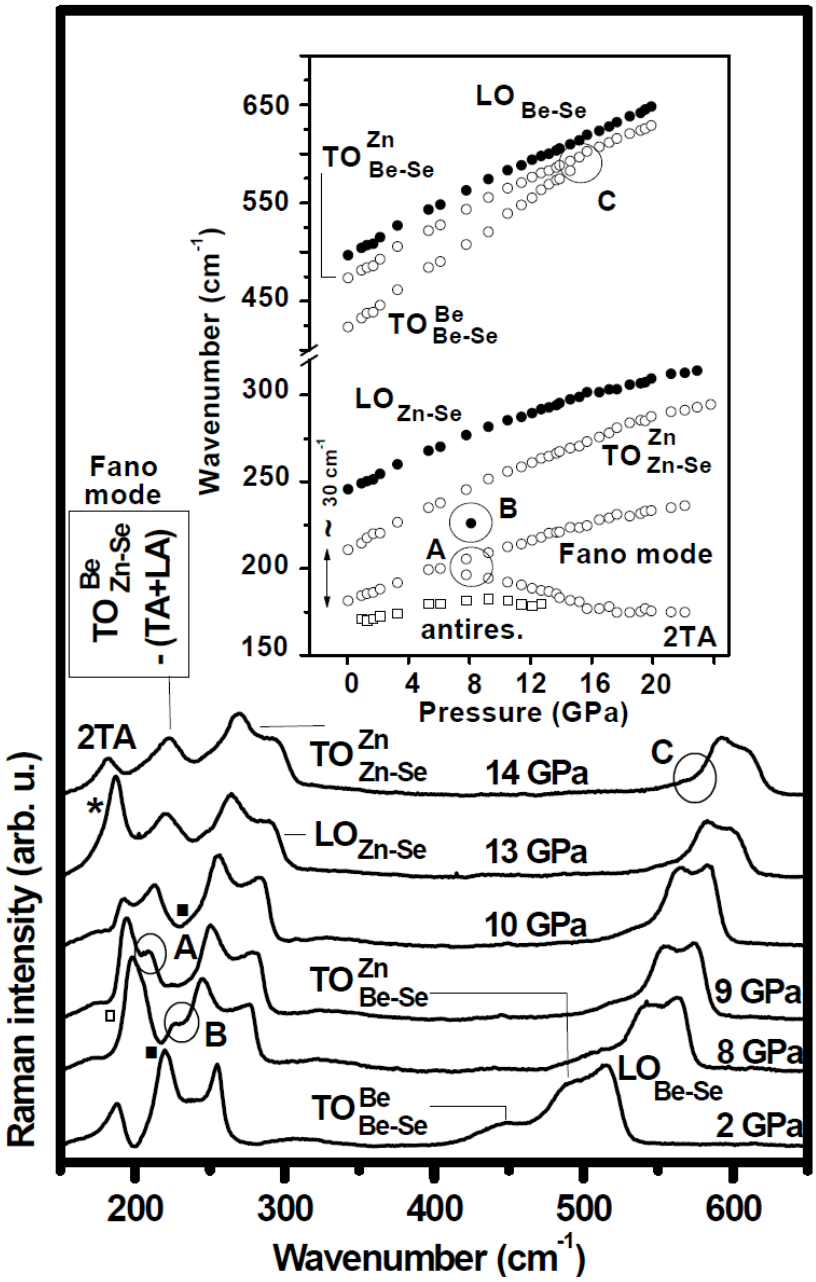

Figure 3-4 : Pressure-dependent Raman spectra of Zn$_{0.76}$Be$_{0.24}$Se. The frequency versus pressure variations of the main features are shown in the inset. Remarkable trends (A,B,C) are marked by circles. The antiresonances (squares) and the strong peak (star) are characteristic of anharmonic coupling.

3.4.1 Zn-Se spectral range

First, we focus on the Zn-Se spectral range. A natural reference is the pressure dependence of the Raman modes in pure ZnSe,[22] as reproduced in Fig. 3-5 (symbols, digitalized from Ref. [22]). Intermediate phases in between the ZB and RS phases have been inferred from the splitting of the TO mode at ~2.5 and ~7 GPa. However, such intermediate phases could not be identified so far, neither experimentally nor by *ab initio* calculations.[33] We suggest that the entire ZnSe spectrum results from an anharmonic decay of the discrete (zone centre) TO into a variety of two-phonon continua, at least two (corresponding to the two subbranches). Characteristic Fano features are discussed below.

In such a decay process, conservations of the momentum and energy impose equal and opposite wave vectors of the two phonons, and quasi-resonance of the discrete TO and two-phonon continua. Referring to the phonon DOS of pure ZnSe,[34] the likely continua are the 2TA and TA+LA originating from the transverse (TA) and longitudinal (LA) acoustical branches at the K and L Brillouin zone edges, respectively. Under pressure, the discrete TO and two-phonon continua decouple because different pressure dependencies lead to a departure from resonance conditions. In ZnSe the zone edge TA ‘softens’ under pressure, while the zone-centre TO and zone edge LA ‘hardens’ fast.[35] The TA trend reflects in the 2TA continuum, while TA+LA is partly compensated by the opposing LA trend. Thus we reassign the two branches that proceed from the TO mode at ~2 and ~7 GPa in ZnSe, with large-negative and small-positive pressure coefficients, as the 2TA and TA+LA continua, respectively.

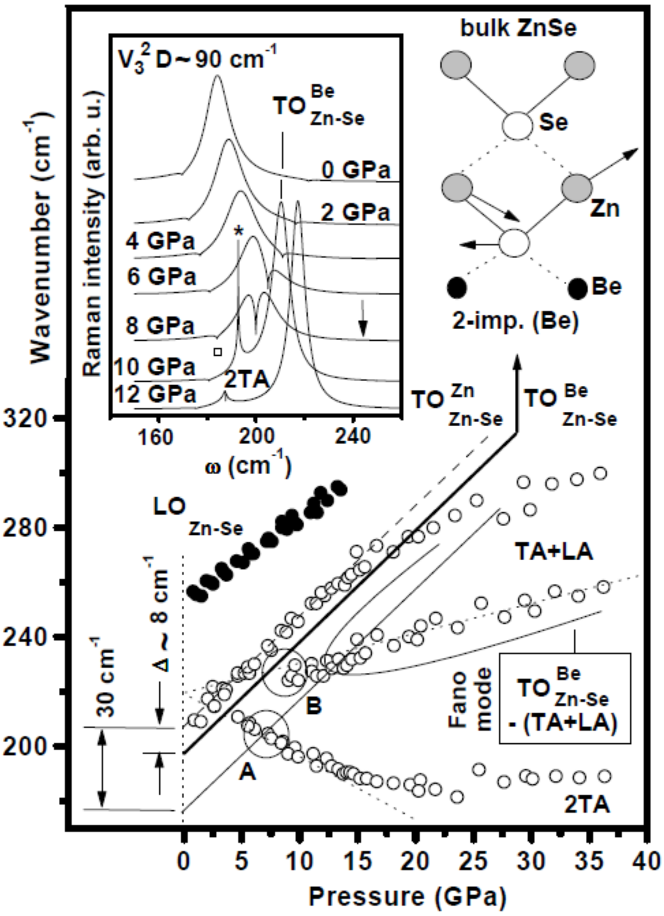

Figure 3-5: Schematic explanation of features A and B (circles) by referring to pure ZnSe (symbols, digitalized from Ref. [22]). In the alloy the weak TO^{Be}_{Zn-Se} (thick line – in the vibration pattern the dotted and plain lines indicate perpendicular planes) appears on top of the strong TO^{Zn}_{Zn-Se} (pure- ZnSe like, dashed line). The natural splitting of ~8 cm^{-1} is magnified to ~30 cm^{-1} by an anharmonic coupling that downshifts the weak mode from the thick line to the thin one. The lineshapes of the weak mode over its decoupling process are shown in the inset. The star and squares mark features characteristic of anharmonic coupling, as in Fig. 3-4. At 8 GPa an arrow marks the position of the harmonic mode, for reference purpose.

The A and B features in Fig. 3-4 can then be simply explained by considering that in the alloy a weak extra TO appears and substitutes for the strong (pure-ZnSe like) TO for the anharmonic decay into the 2TA continuum. The principle is outlined in Fig. 3-5. The weak TO is represented by a thin line downshifted from the strong TO (dashed line) by ~30 cm^{-1}.

With this, the 2TA-decoupling is delayed from ~2 GPa in pure ZnSe (from the strong TO, see the dotted arrow) to ~7 GPa in the alloy (from the weak TO), in reference to A, while B at ~7 GPa is due to transient appearance of the TA+LA continuum just after decoupling from the strong TO and before re-coupling with the weak TO (see the oval). In fact the coupling-related antiresonance in-between the two TO (solid squares in Fig. 3-4) disappears in this intermediate decoupling regime (see the spectrum at ~9 GPa in Fig. 3-4).

Altogether, this implies a well-resolved Zn-Se percolation doublet (weak plus strong TO) in ZnBeSe, instead of a singlet as earlier presumed.[19] The splitting of the Zn-Se doublet (Δ~30 cm^{-1}, refer to the inset in Fig. 3-4), almost as large as the Be-Se one, is puzzling though.[19] For example, in ZnBeTe[36] the Zn-Te (Δ~6 cm^{-1}) and Be-Te (Δ~35 cm^{-1}) splittings scale in the ratio 1:6. For independent insight we performed *ab initio* calculations with the 2-imp. (Be) motif in ZnSe. The short Be-Se bonds create a local tension in ZnSe, giving rise to a local Zn-Se mode around Be (TO_{Zn-Se}^{Be}, weak – see the vibration pattern in Fig. 3-5) at a lower frequency than the bulk Zn-Se one, away from Be (TO_{Zn-Se}^{Zn}, strong). As expected, the *ab initio* splitting is small, of ~8 cm^{-1}, corresponding to a position of the harmonic (uncoupled) weak TO_{Zn-Se}^{Be} renormalized to the thick line in Fig. 3-5. We infer that the anharmonic coupling induces a massive frequency downshift of the weak TO_{Zn-Se}^{Be} with respect to the *ab initio* prediction (by ~22 cm^{-1}), the strong TO_{Zn-Se}^{Zn} remaining unaffected. This suggests that the continua couple strongly to the weak TO and weakly to the strong one.

For a quantitative insight, we perform analysis of the TO line shapes using the formula[37] $I(\omega) \sim \left[\alpha + \Gamma(\omega)\right]^2 . \left[\left(\omega - \omega_0 - \Delta(\omega)\right)^2 + \left(\alpha + \Gamma(\omega)\right)^2\right]^{-1}$, where ω_0 and α are the frequency and natural damping of the harmonic TO, $\Delta(\omega)$ and $\Gamma(\omega)$ relate to the two-phonon

DOS and its Kramers-Krönig's transform, respectively. The two-phonon DOS is designed as a semi-ellipse, its position, magnitude and spectral extension being fixed by its upper end ω_c, and its semi-axes D and a, respectively.[37] The model includes a fourth-order coupling V_4 (between pairs of phonons in the two-phonon continuum) on top of the third-order one V_3 (between the TO and the two-phonon continuum). To make it physically more meaningful, only one parameter is adjusted per TO mode, i.e. the strength $V_3^2 D$ of the cubic coupling, the criterion for validation being the ability to reproduce the TO-decoupling process (at P~7 GPa for both TO modes).

For the strong TO_{Zn-Se}^{Zn}, ω_0 is taken as the observed peak position, since anharmonic effects are presumably small, while for the weak TO_{Zn-Se}^{Be}, we use the *ab initio* value. As for the two-phonon DOS, the pressure dependence of the upper ends (ω_c) are derived by linear interpolations of the pressure dependencies of the decoupled 2TA (for TO_{Zn-Se}^{Be}) and LA+TA (for TO_{Zn-Se}^{Zn}) bands in pure ZnSe (refer to the dotted lines converging to ~220 cm^{-1} at 0 GPa in Fig. 3-5), after small translations (by less than 2 cm^{-1}) needed to mimic alloying effects. The lower end, monitored by a once known ω_c, provides an antiresonance on the low-frequency tail of the coupled TO (coupling regime) or uncoupled-two-phonon-DOS (decoupling regime). The 2TA-antiresonance is clearly visible in our Raman spectra (refer to open squares in Fig. 3-4). For an insight into the (TA+LA) - related antiresonance, we resort to the pure-TO Raman spectrum (24%Be, 0 GPa) available elsewhere[38] (top curve of Fig. 2 in ref[38]). Clear antiresonances on each side of the strong TO therein, spaced by ~15 cm^{-1}, correspond to a~5 cm^{-1}, taken constant for all pressures. Lastly, the strength V_4D of the fourth order coupling is constrained to the α value (within 5%), taken as ~2.5 cm^{-1} for all pressures.

As expected, $V_3^2 D$ is larger for the weak TO_{Zn-Se}^{Be} mode (with a value of ~ 90 cm^{-1}) than the strong TO_{Zn-Se}^{Zn} one (stable at ~10 cm^{-1}). The pressure dependent line shapes of the weak TO (the strongly coupled one) over its decoupling process are shown in the inset of Fig. 3-5. The main features are well-reproduced, i.e. the deepening of the antiresonance at ~180 cm^{-1}, just when decoupling occurs (open square in Fig. 3-4 and in the inset of Fig. 3-5 – the arrow marks the frequency of the harmonic TO mode therein), and the subsequent appearance of the uncoupled 2TA band as an intense peak (refer to the star in Figs 3-4 and 3-5) before it collapses into a damped feature away from the TO mode.

In brief, an anharmonic coupling greatly magnifies (by ~4) the natural splitting (Δ~8 cm^{-1}) of the Zn-Se percolation doublet, giving a chance to observe its dependence on pressure. The two ZnSe-like TO branches are quasi-parallel in Fig. 3-4 (spaced by ~30 cm^{-1}, refer to the inset), indicating a constant Zn-Se splitting. *Ab initio* calculations at 0 and 10 GPa with the 2-imp. (Be) motif in ZnSe confirm the trend. We conclude that, as far as the Zn-Se bonds are concerned, the BeSe- and ZnSe-like regions of the crystal show similar behaviour under pressure.

3.4.2 Be-Se spectral range

Unlike the Zn-Se bonds, it is a different case for the Be-Se bonds, as testified by C in Fig. 3-4. It is remarkable that this(C) occurs at the same critical pressure of 14±1 GPa for all the samples (see Figs. 3-2, 3-3 and 3-4) independent of the topology of the BeSe-like region. Apparently no effect is seen on whether the sample consists of a dispersion of finite-size clusters ($x<x_{Be}$), of the as-formed pseudo-infinite continuum (x just above x_{Be}) or of the dominant percolation cluster (x just above 0.5). This indicates a local origin at the bond scale. It can be recalled that pure ZnSe undergoes to the RS phase at around the same pressure. In

fact, the *ab initio* ZC TO-DOS curves per Be atom obtained at 0 and 10 GPa with the ultimate 2-imp. (Be) motif in ZnSe, as shown in the body of Fig. 3-6, does exhibit the C-type behaviour. The curves are shown in the body of Fig. 3-6, specifying the vibration pattern per mode. In view of this, we identify the microscopic mechanism behind C as the progressive transformation of the TO_{Be-Se}^{Be} mode (Be-Se vibration along the Be-Se-Be chain, || chain) from the bond-stretching type to the bond-bending type under pressure (see the vibration patterns in Fig. 3-6). The nature of the doubly-degenerate TO_{Be-Se}^{Zn} mode (Be-Se vibrations perpendicular to the chain, in-plane and out-of-plane, ⊥ chain), remains the same i.e. of the bond-bending type.

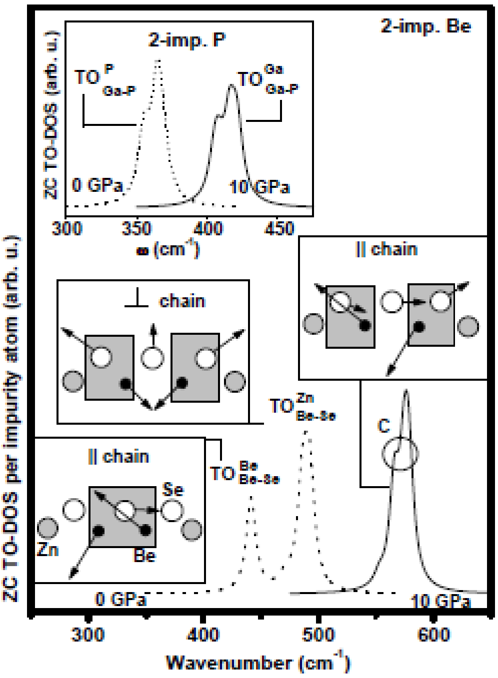

Figure 3-6: *Ab initio* ZC TO-DOS per impurity of the 2-imp. Be (main curves) and P (inset) motifs in ZnSe- and GaAs-like supercells, respectively. The Be-Se vibration patterns are indicated, emphasizing the bond-stretching modes (dashed areas) in reference to feature C (circle).

For further insight we performed similar *ab initio* calculations with the 2-imp. (Zn) motif in BeSe (Zn-dilute limit). The long Zn-Se bonds create a local compression in BeSe, leading to a local Be-Se mode close to Zn, i.e. TO_{Be-Se}^{Zn} (the vibration pattern is shown in Fig. 3-5, where Zn and Be are exchanged), at a higher frequency than the bulk BeSe mode, i.e. TO_{Be-Se}^{Be}. This gives a clear Be-Se doublet, though the splitting is less than in the Be-dilute limit, of ~11 cm^{-1}. Now, we observed the same splitting value at 0 and 10 GPa, indicating that C-type behaviour disappears when the Be-Se bonds are dominant in the crystal, and thus not influenced by the Zn-Se bonds.

A further instructive case is that of GaAsP. Its short bond (Ga-P) exhibits a distinct percolation doublet (Δ ~12 cm^{-1}),[19] as in ZBS, but, the parents (GaAs, GaP) adopt the same phase under pressure (ZB→Cmcm) but at nearly the same critical pressure (~15±3 GPa). The ZC TO-DOS curves per P atom obtained at 0 and 10 GPa with the 2-imp. (P) motif in GaAs are shown in the inset of Fig. 3-6. The Ga-P percolation doublet is shifted upwards as a whole when approaching the phase transition without any C- type convergence.

It emerges that C-type convergence is not intrinsic to short bonds in alloys but specific to the Be-Se bonds in ZnBeSe, especially when their fraction is such (low or moderate) that they are forced to adopt the ZnSe-like rocksalt phase under pressure.

For an intuitive discussion of the feature C, we turn to the percolation model. Note that such phenomenological model relies on a scalar description of the alloy (linear chain approximation), so that everything comes down to a question of bond-stretching forces only, by construction. Still, a parallel between the percolation model (mesoscopic scale) and *ab initio* calculations (microscopic scale) can be drawn by realizing that *'bond-bending within a given impurity motif corresponds to bond- stretching of the (like) surrounding bonds from the* *host matrix, and vice versa*’. If we refer to the 2-imp. (Be) motif in ZnSe, this comes down to discuss the low and high-frequency Be-Se modes in terms of Be-Se stretching within the BeSe and ZnSe-like regions, respectively (see the shaded areas in the vibration patterns, Fig. 3-6), consistent with the terminology of the percolation model. Within such stretching-type model, feature C can thus be understood as due to the progressive ‘freezing’ of the Be-Se bonds from the minor BeSe-like region when this is forced to adopt the unnatural RS phase of the host ZnSe-like region. The oscillator strength is transferred to the close Be-Se bonds of the latter region.

3.5 Conclusions

In summary, the percolation doublet PD mesoscope reveals that the lattice dynamics of the ZnBeSe crystal changes when approaching the ZB→RS, ZnSe-like transition under pressure, an unnatural one for the Be-Se bonds. Within the scope of the percolation model, the highly self-connected Be-Se bonds from the BeSe-like region ‘freeze’, the oscillator strength being channelled to the less self connected Be-Se bonds of the surrounding ZnSe-like region. This process is transparent for the Zn-Se dynamics, and completed (~14 GPa) before the transition to RS occurs (~23 GPa at 24%Be). Generally this work shows how the percolation approach may help to achieve further understanding of the pressure dependence of phonons in alloys beyond the usual VCA paradigm.

3.6 Reference

1. M. A. Haase, J. Qiu, J. M. DePuydt, and H. Cheng, Applied Physics Letters **59,** 1272 (1991).
2. A. Ishibashi, Journal of Crystal Growth **159,** 555 (1996).
3. F. Fischer, G. Landwehr, T. Litz, H. J. Lugauer, U. Zehnder, T. Gerhard, W. Ossau, and A. Waag, Journal of Crystal Growth **175-176,** 532 (1997).
4. F. Vigue, E. Tourni, and J. P. Faurie, IEEE Journal of Quantum Electronics **37,** 1146 (2001).
5. A. Waag, et al., Applied Physics Letters **70,** 280 (1997).
6. A. Waag, et al., Journal of Crystal Growth **184-185,** 1 (1998).
7. C. Verie, Semiconductors Heteroepitaxy, Eds. B. GIL and R. L. Aulombard, World Scientific Publ. Co, Singapore **73** (1995).
8. C. Verie, Journal of Crystal Growth **184-185,** 1061 (1998).
9. C. Verie, Journal of Electronic Materials **27,** 782 (1998).
10. V. Wagner, J. J. Liang, R. Kruse, S. Gundel, M. Keim, A. Waag, and J. Geurts, Physica Status Solidi (B) Basic Research **215,** 87 (1999).

11. C. Chauvet, E. Tournie, and J. P. Faurie, Physical Review B **61,** 5332 (2000).
12. O. Pages, M. Ajjoun, J. P. Laurenti, D. Bormann, C. Chauvet, E. Tourni, and J. P. Faurie, Applied Physics Letters **77,** 519 (2000).
13. O. Pages, M. Ajjoun, D. Bormann, C. Chauvet, E. Tourni, and J. P. Faurie, Physical Review B **65,** 352131 (2002).
14. O. Pages, M. Ajjoun, T. Tite, D. Bormann, E. Tourni, and K. C. Rustagi, Physical Review B **70,** (2004).
15. A. V. Postnikov, O. Pages, T. Tite, M. Ajjoun, and J. Hugel, Phase Transitions **78,** 219 (2005).
16. M. Szybowicz, M. Kozielski, F. Firszt, S. Legowski, and H. Meczynska, Crystal Research and Technology **38,** 359 (2003).
17. C. S. Yang, W. C. Chou, D. M. Chen, C. S. Ro, J. L. Shen, and T. R. Yang, Physical Review B **59,** 8128 (1999).
18. A. V. Postnikov, O. Pages, and J. Hugel, Physical Review B **71,** 1 (2005).
19. O. Pages, A. V. Postnikov, M. Kassem, A. Chafi, A. Nassour, and S. Doyen, Physical Review B **77,** (2008).

20. I. F. Chang and S. S. Mitra, Physical Review **172,** 924 (1968).

21. I. F. Chang and S. S. Mitra, Adv. Phys. **20,** 359 (1971).

22. W. C. Chou, et al., Chinese Journal of Physics **35,** 266 (1997).

23. R. G. Greene, H. Luo, and A. L. Ruoff, Journal of Physics and Chemistry of Solids **56,** 521 (1995).

24. G. Itkin, G. R. Hearne, E. Sterer, M. P. Pasternak, and W. Potzel, Physical Review B **51,** 3195 (1995).

25. S. Ves, K. Strossner, N. E. Christensen, C. K. Kim, and M. Cardona, Solid State Communications **56,** 479 (1985).

26. H. Luo, K. Ghandehari, R. G. Greene, A. L. Ruoff, S. S. Trail, and F. J. Disalvo, Physical Review B **52,** 7058 (1995).

27. A. Mujica, A. Rubio, A. Munoz, and R. J. Needs, Reviews of Modern Physics **75,** 863 (2003).

28. J. D. Barnett, S. Block, and G. J. Piermarini, Review of Scientific Instruments **44,** 1 (1973).

29. J. M. Soler, E. Artacho, J. D. Gale, A. Garcia, J. Junquera, P. Ordejon,

and D. Sanchez-Portal, Journal of Physics Condensed Matter **14,** 2745 (2002).

30. M. Ajjoun, O. Pages, J. P. Laurenti, D. Bormann, C. Chauvet, E. Tournie, J. P. Faurie, and O. Gorochov, Thin Solid Films **403-404,** 530 (2002).
31. M. Ajjoun, T. Tite, A. Chafi, J. P. Laurenti, O. Pages, and E. Tournie, Journal of Alloys and Compounds **382,** 271 (2004).
32. A.Polian, T.Ganguli, and S.K.Deb *private communication*.
33. C. M. Lin, D. S. Chuu, T. J. Yang, W. C. Chou, J. A. Xu, and E. Huang, Physical Review B **55,** 13641 (1997).
34. B. D. Rajput and D. A. Browne, Physical Review B **53,** 9052 (1996).
35. B. A. Weinstein, Solid State Communications **24,** 595 (1977).
36. O. Pages, T. Tite, D. Bormann, O. Maksimov, and M. C. Tamargo, Applied Physics Letters **80,** 3081 (2002).
37. M. L. Shand, H. D. Hochheimer, M. Krauzman, J. E. Potts, R. C. Hanson, and C. T. Walker, Physical Review B **14,** 4637 (1976).
38. O. Pages, M. Ajjoun, J. P. Laurenti, D. Bormann, C. Chauvet, E. Tournin, and J. P. Faurie, Applied Physics Letters **77,** 519 (2000).

Chapter 4[*]

High Temperature Raman Studies on a Novel Fast Ion Conductor, $Na_2Cd(SO_4)_2$

A paper based on this work has been published in Journal of Physical Chemistry A, **113** 1505–1507 (2009)

---

[*] The author's main contribution in this chapter is in doing the high temperature Raman experiments, analyzing and interpreting the data. The samples used in this study were grown by Diptikant Swain of Indian Institute of Science, Bangalore, India.

4.1 Introduction

Solid electrolytes (fast ion conductors) have been a subject of considerable attention due to their potential use in various electrochemical devices such as batteries, fuel cells, sensors and reactors.[1-3] This class of materials exhibits high ionic conductivity (approximately 10^{-3}-10^{-1} S/cm) at relatively modest temperatures (500-700 °C) and has been one of the major themes in material design. Of late, microporous materials have been used to mobilize extra framework cations and thus induce high ionic conductivity.[4] Extensive work on crystalline solid electrolytes like, for example, NASICON and LISICON,[5-7] Bimivox,[8,9] and rock salts[10] has resulted in generating several potential ionic conductors. The ions that normally conduct are Li^+, Na^+, H^+, K^+, Ag^+, O^{2-}, and F^-. Room temperature conductivity of 0.3 S/cm has been observed in Ag and Cu halide systems.[11,12] Furthermore, binary lithium halide systems (for example, LiI-RbI[13]) have been investigated for high ionic conductivity. Recently, bimetallic sulfates, which are intercalation compounds of alkali ions generated by frameworks of tetrahedral and octahedral moities, have been shown to achieve high ionic conductivity. One of the examples is $Na_2Cd(SO_4)_2$ (NCSO), which has been investigated as a possible ionic conducting material.[14] NCSO is a bimetallic sulphate where Cd atom is at 2-fold rotational symmetry having a Wyckoff position 4e in the space group *C*2/*c*.[14] Fig. 4-1 shows the packing diagram as viewed down the z-axis. The structure (see Fig. 4-1) is built of alternating sulfate tetrahedra linked to Cd octahedra forming a chain along the [110] direction, which in turn is cross-linked with a chain running 90° to this plane, effectively generating a two-dimensional framework (see Fig. 4-2). Every Cd atom has two short, two medium, and two long bonds with symmetry-related oxygen atoms. Likewise, every S atom has one short, two normal, and one long tetrahedral bond, while the Na atom located in the two-dimensional framework generates a weak eight-coordinated link that extends along the *z*-axis, forming a channel-like structural motif (see Fig. 4-2). Indeed, the Na atoms are located in the space generated by the combination of covalently bound octahedra and tetrahedra. This suggests the possibility of facile Na^+ ion migration through the framework, and the rather high ionic conductivity of 10^{-2} S/cm at 600 °C appears as a consequence. Furthermore, the dielectric and conductivity data showed two possible transitions around 280 and 555 °C.[14]

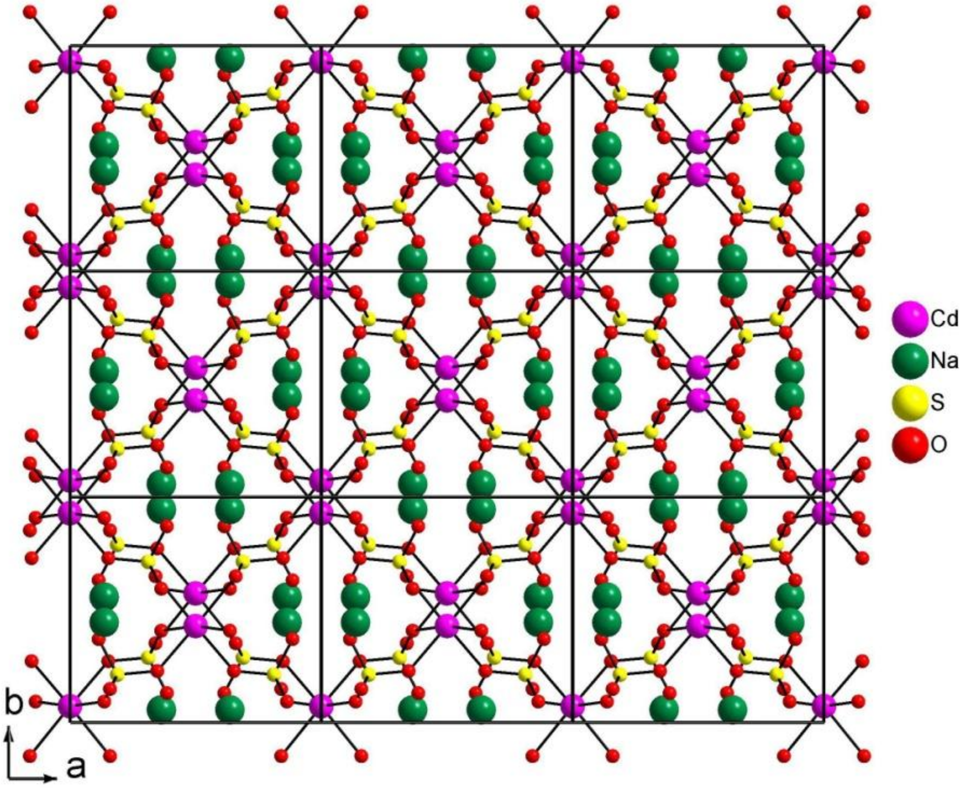

Figure 4-1: Packing diagram of $Na_2Cd(SO_4)_2$, view down the *z*-axis.

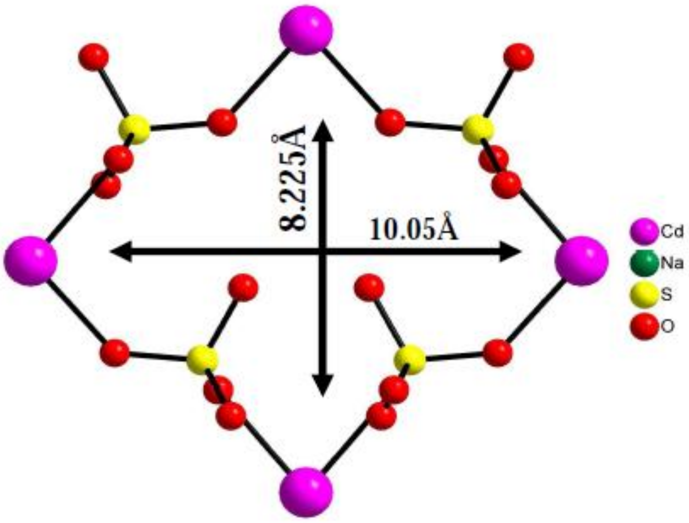

Figure 4-2: Channels of $Cd_4(SO_4)_4$

To understand the relationship between conductivity and NCSO structure, a detailed investigation on ionic conductivity and phase transformations is very much essential. We have carried out a Raman spectroscopic study of NCSO as a function of temperature to probe these changes across the phase transition. It is well-known that Raman scattering is sensitive to variations of local structure/environment and thus can give information on aspects such as short-range versus long-range structural order. The sensitivity of this technique to local environments makes it an ideal probe to answer questions related to short or medium range mobility. In this work, temperature dependent Raman spectroscopy was used to probe the dynamics of the SO_4 tetrahedra around the phase transformation by studying the internal modes of SO_4 tetrahedra and their line shapes, which are shown to be sensitive to molecular reorientation.[15-18]

4.2 Experimental Details

Single crystals of NCSO were grown by slow evaporation from aqueous solution containing equimolar quantities of the $3CdSO_4 \cdot 8H_2O$ and Na_2SO_4, based on the method described in ref 13. The temperature evolution of the Raman spectra of NCSO was recorded in the 180° backscattering geometry, using a 532 nm excitation from a diode pumped frequency doubled Nd- YAG solid state laser (model GDLM-5015 L, Photop Suwtech Inc., China) and a custom-built Raman spectrometer equipped with a SPEX TRIAX 550 monochromator and a liquid nitrogen cooled CCD (Spectrum One with CCD 3000 controller, ISA Jobin Yovn-SPEX). The details of the spectrometer are described in Chapter 2. Laser power at the sample was ~15 mW, and a typical spectral acquisition time was 1-2 min. The spectral resolution was 2 cm^{-1}. The temperature was controlled with an accuracy of (0.1 K by using a temperature-controller (Linkam TMS 94) equipped with a heating stage unit (Linkam THMS 600). The spectral profile was fitted using Lorentzian functions with the appropriate background.

4.3 Results and Discussion

The normal-mode analysis of a free tetrahedral SO_4 ion in a T_d symmetry predicts four modes, v_1(A1), v_2 (E), v_3 (F2), and v_4 (F2).[19] All of these modes are Raman active, whereas v_3 and v_4 modes are IR active.[19] In the crystalline environment, the tetrahedral symmetry of SO_4 may be lowered, and as a result band positions will shift and also split.[20] The nondegenerate symmetric stretching mode (v_1) appears as a very intense band in the Raman spectrum.[16] The triply degenerate asymmetric stretching mode (v_3) of the SO_4 ion appears with large splitting in both Fourier transform infrared (FTIR) and Raman spectra.[16] Fig. 4-3 shows a comparison of room temperature Raman and FTIR spectra in the SO_4 internal vibration region. On the basis of the assignments discussed earlier, we have labeled the internal vibration modes v_1, v_2, v_3, and v_4 of the tetrahedral SO_4 group in Fig. 4-3.

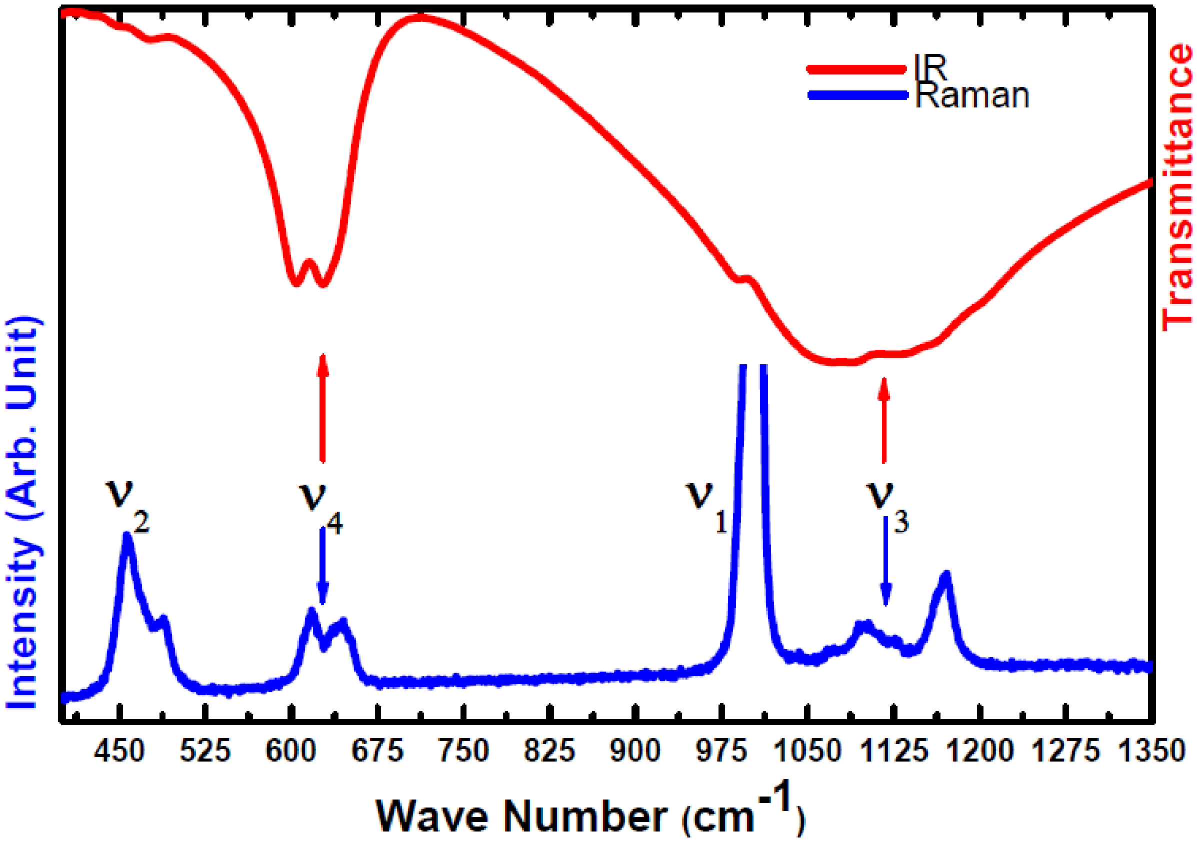

Figure 4-3: Room-temperature infrared and Raman spectra of $Na_2Cd(SO_4)_2$ showing the SO_4 internal vibrational modes.

Wu and Frech, who recorded the vibrational spectra of several sulfate crystals, suggest that in the case of SO_4 groups, v_1, v_2, v_3, and v_4 range between 985-1017, 455-473, 1097-1217, and 611-670 cm^{-1}, respectively.[21] Hence, the strong Raman band at ~993 cm^{-1} is indeed the v_1 mode. Similarly, the Raman bands associated with v_2 region appear at 458 cm^{-1} (v_{2a}) and 487 cm^{-1} (v_{2b}). The Raman and infrared bands around 1092 and 1161 cm^{-1} are assigned to the v_{3a} and v_{3b}, respectively. Also, the bands occurring at 623 cm^{-1} (v_{4a}) and 651 cm^{-1} (v_{4b}) are assigned to the v_4 vibration. As expected, the infrared spectra show stronger absorption in the v_3 and v_4 regions.

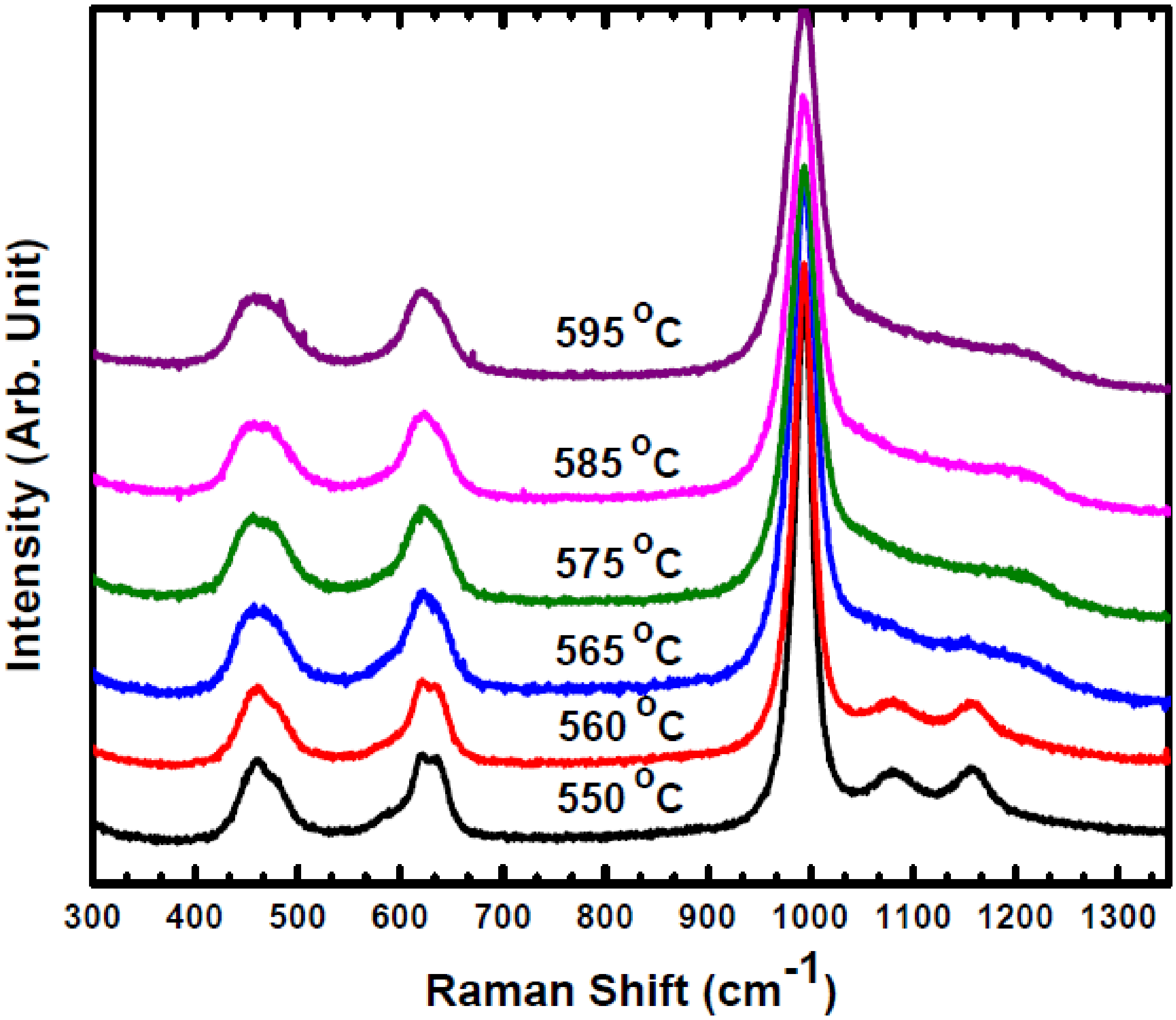

Figure 4-4: Temperature evolution of the Raman spectra of $Na_2Cd(SO_4)_2$ in the temperature interval 550-595 °C.

The temperature evolution of the Raman spectra of NCSO measured in the SO_4 internal vibration region in the temperature interval from 24 to 550 °C does not show any large-scale changes in the spectral profile. Hence, in Fig. 4-4 we have shown the temperature dependence of the Raman spectra in the temperature interval 550-595 °C. Significant changes in the spectra are observed beyond ~565 °C. The splitting of the ν_3 band disappears, and a broadband centred at around 1180 cm^{-1} appears. At the same time, the ν_1 mode also showed an appreciable broadening during this transformation. The temperature dependence of the full width at half-maximum (FWHM) of the ν_1 stretching mode measured in the temperature interval from 24 to 600 °C is shown in Fig. 4-5.

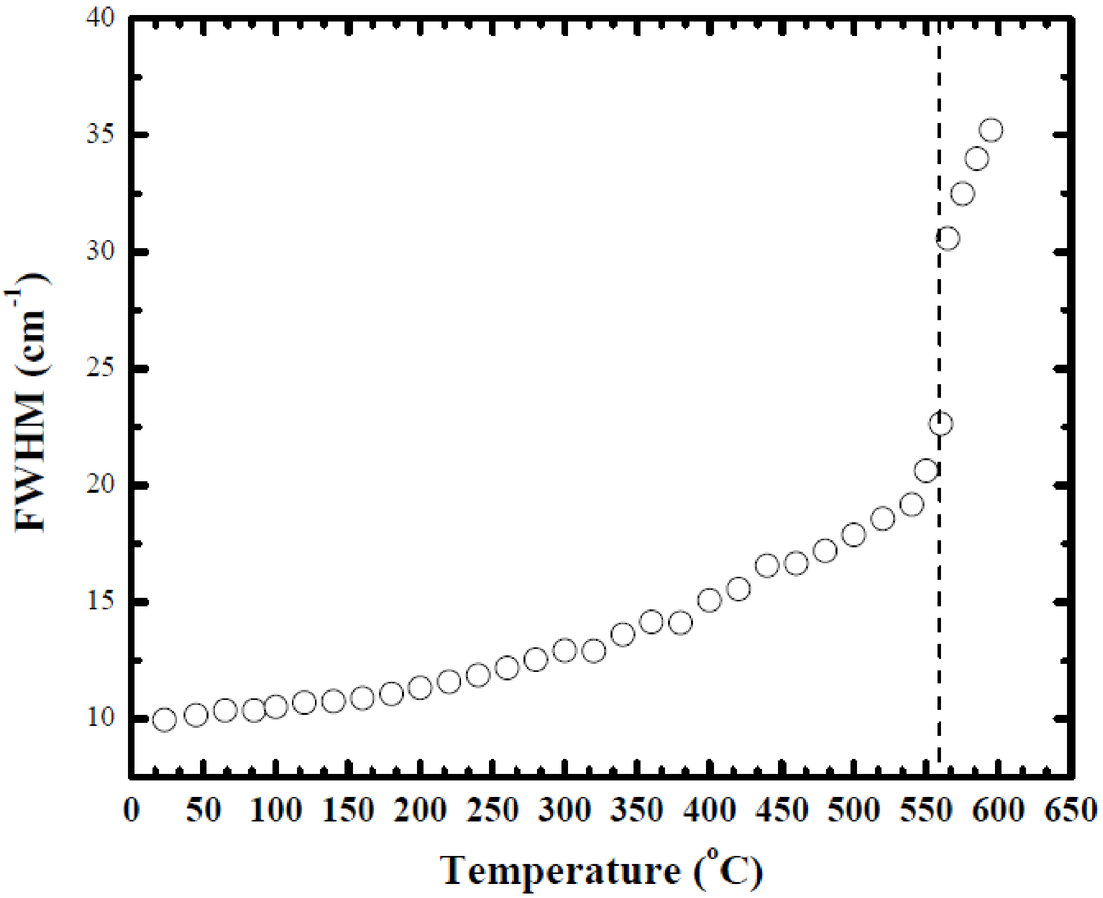

Figure 4-5: Temperature dependence of the fwhm of the ν_1 mode of the SO_4 ion in the temperature interval 24-595 °C.

The width of this band is around 10 cm^{-1} at room temperature, but it gradually broadens to 23 cm^{-1} at 560 °C. However, the line width of this band increased abruptly from 23 to 31 cm^{-1} in the temperature interval 560-565 °C. The reason for this abrupt change is discussed below. Fig. 4-6 shows the temperature dependence of the v_2 and v_4 mode frequencies. There is a change in slope ($d\omega/dT$) around 260 °C for both v_2 and v_{4b} modes. The changes in mode frequency associated with the v_2 and v_4 mode could be associated with tilting of the SO_4 tetrahedra, which could prevent the smooth migration of the Na^+ ion. This will result in a small decrease in conductivity as observed earlier as shown in the conductivity data where there is a small kink at 280 °C.[14] Small discontinuities were observed at 565 °C for both v_2 and v_4 modes.

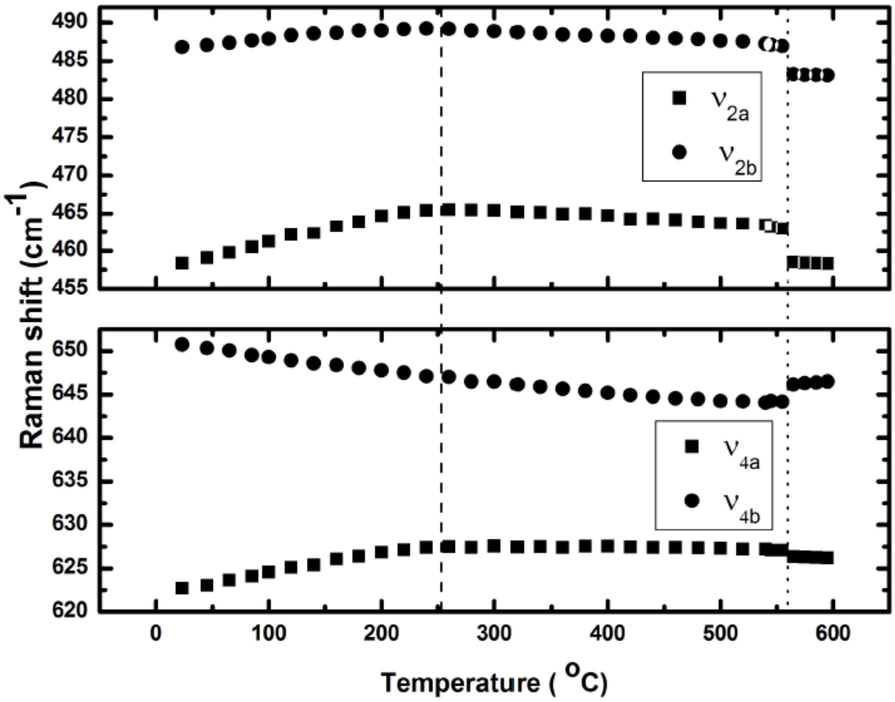

Figure 4-6: Temperature dependences of the v_2 and v_4 modes of the SO_4 ion in the temperature interval 24-595 °C.

This we attribute due to the reorientation of the SO_4 tetrahedra. The abrupt jump in the line width of ν_1 mode, major changes in the spectral profile in the ν_3 mode, and discontinuities in the frequencies for both ν_2 and ν_4 modes observed in the temperature interval between 560 and 565 °C could arise due to an increase in the rotational degree of freedom of the SO_4 ion at high temperatures. The reduction of the mode frequencies of most of the modes (ν_1, ν_2 and ν_4 modes) signifies that mobility of Na^+ in the channel makes the oxygens in the SO_4 units move away from the sulfur, decreasing the bond strength of the S-O bonds in the SO_4 units. The role of sulfate internal modes in Li_2SO_4[22] and $LiKSO_4$[23] has long been investigated in a similar context. Also, similar high-temperature behaviour was reported in Na_3PO_4,[18] which has been attributed to rotational motion (anion reorientation) of the translationally fixed PO_4. Moreover, coherent quasielastic neutron scattering study[24] and careful X-ray analysis[25] probing oxyanion reorientation revealed a 3-fold symmetry distribution of the SO_4 tetrahedron orientations around the crystallographic *c*-axis. The introduction of some disorder in the sulfate orientations or the cation positions can cause the observed increase in the phonon damping versus temperature, which in principle will depend on the particular eigenvector of any vibration.[22] It is possible that a particular eigenmode assists the jumps between the different configurations and this relatively stronger coupling to the disordering process causes an abrupt change in the phonon lifetime and hence the width of ν_1 mode. We believe that rapid rotational motion of the disordered SO_4 tetrahedra defines the channel better, hence enhancing the Na^+ migration and resulting in high conductivity across this transition. This is corroborated in the conductivity data measured earlier.

4.4 Conclusion

From the temperature evolution of the Raman spectra of NCSO, we confirm the change in conductivity observed in the earlier conductivity measurement[14] is associated with the local structural distortions of the SO_4 tetrahedra due to increased rotational degree of freedom as a function of temperature. The sudden jump in the conductivity across the transition at the high-temperature phase is attributed to the rapid rotational motion of the SO_4 tetrahedra. The rotational motion of the SO_4 ions enhances the Na+ migration, resulting in high conductivity during the transition. The reorientational motion of the SO_4 ions revealed by temperature-dependent Raman spectroscopy studies and their coupling with sodium ion motion inferred from electrical conductivity measurements strongly suggest that there is a correlation between the structural and dynamic changes across this phase transformation.

4.5 References

1. B. Zhu, I. Albinsson, B. E. Mellander, and G. Meng, Solid State Ionics **125,** 439 (1999).
2. B. Zhu, Solid State Ionics **125,** 397 (1999).
3. N.P.Brandon, S.Skinner, and B.C.H.Steele, Annu. Rev. Mater. Res. **33,** 183 (2003).

4. S. H. Park, J. B. Parise, H. Gies, H. Liu, C. P. Grey, and B. H. Toby, Journal of the American Chemical Society **122,** 11023 (2000).
5. P. G. Bruce, Solid-State Electrochemistry, Cambridge University Press: Cambridge (1997).
6. T. Takahashi Ed., High Conductivity Solid Ionic Conductors: Recent Trends and Applications; World Scientific, Singapore (1989).
7. S. Chandra, Super Ionic Solids: Principles and Applications, North-Holland Publishing: Amsterdam (1981).
8. K. R. Kendall, C. Navas, J. K. Thomas, and H. C. Zur Loye, Chemistry of Materials **8,** 642 (1996).
9. J. C. Boivin and G. Mairesse, Chemistry of Materials **10,** 2870 (1998).
10. J. B. Goodenough, Nature **404,** 821 (2000).
11. B. B. Owens and G. R. Argue, Science **157,** 308 (1967).
12. P. Lacorre, F. Goutenoire, O. Bohnke, R. Retoux, and Y. Lallgant, Nature **404,** 856 (2000).
13. X. Wei and D. F. Shriver, Chemistry of Materials **12,** 2528 (2000).

14. D. Swain and T. N. Guru Row, Chemistry of Materials **19,** 347 (2007).

15. V. Devarajan and E. Salje, Physics and Chemistry of Minerals **13,** 25 (1986).

16. S. Kreske and V. Devarajan, Journal of Physics C: Solid State Physics **15,** 7333 (1982).

17. J. A. Moreira, A. Almeida, M. R. Chaves, M. L. Santos, P. P. Alferes, and I. Gregora, Physical Review B - Condensed Matter and Materials Physics **76,** (2007).

18. G. Raje, B. J. Kalaiselvi, D. Shanmukaraj, R. Sridarane, B. Palanivel, and R. Murugan, Ionics **10,** 263 (2004).

19. G. Herzberg, Infrared and Raman Spectra of Polyatomic Molecules, Van Nostrand: New York (1966).

20. D. M. Adams, Coordination Chemistry Reviews **10,** 183 (1973).

21. G. J. Wu and R. Freeh, The Journal of Chemical Physics **66,** 1352 (1977).

22. E. Cazzanelli, A. Fontana, F. Rocca, and R. Frech, Physica Status Solidi (B) Basic Research **140,** 621 (1987).

23. S. B. Kim and R. Frech, The Journal of Chemical Physics **88,** 2216 (1988).

24. D. Wilmer, K. Funke, M. Witschas, R. D. Banhatti, M. Jansen, G. Korus, J. Fitter, and R. E. Lechner, Physica B: Condensed Matter **266,** 60 (1999).

25. H. Schulz, U. Zucker, and R. Frech, Acta Crystallographica **B41,** 21 (1985).

Chapter 5[*]

Temperature Dependent Brillouin Scattering Investigations of the Acoustic Phonons in Pyrochlores $RE_2Ti_2O_7$ (RE = Sm, Dy, Ho and Lu)

A paper based on this work has been communicated to Physical Review B

---

[*] The author's main contribution in this chapter is in doing the low temperature Brillouin experiments, analyzing and interpreting the data. The problem was envisaged by Ajay K. Sood of Indian Institute of Science, Banagalore, India. The samples used in this study were grown by Surjit Singh, A Revcolevschi and R. Suryanarayanan of Laboratoire de Physico-Chimie de l'Etat Solide, Université Paris-Sud, Orsay, France.

5.1 Introduction

Materials with the pyrochlore ($A_2B_2O_7$) lattice structure have unique properties that make them ideal candidates for applications ranging from high-permittivity dielectrics[1], to ceramic thermal barrier coatings,[2] potential solid electrolytes in solid-oxide fuel cells[3], or immobilization hosts of actinides in nuclear waste[4]. A subclass of the pyrochlores is formed in the rare earth titanate ($RE_2Ti_2O_7$) family, if the ratio of ionic radii of the cations RE^{3+} and Ti^{4+} lies within the "pyrochlore stability field",[5] defined as $1.46 < (\xi = r^{3+} / r^{4+}) < 1.80$. This condition is satisfied for RE = Sm → Lu in the lanthanide series.

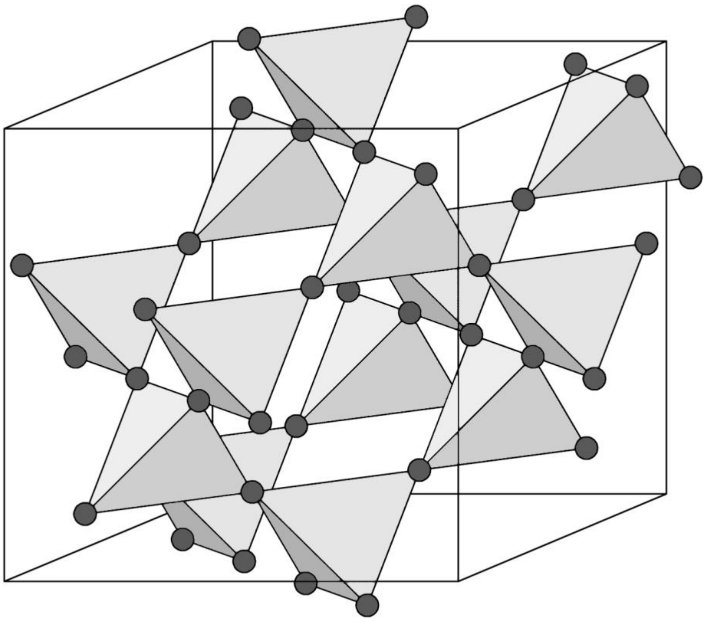

Figure 5-1: Structure of the Pyrochlore lattice

The pyrochlore structure, which is a derivative structure of fluorite, has a face-centred cubic lattice (space group *Fd*3*m*) with a stoichiometry $RE_2Ti_2O_6O'$. Following the Wyckoff notations, in this structure the RE^{3+} and the Ti^{4+} ions occupy, respectively, the 16*c* and the 16*d* sites, whereas O is at the 48*f* and O′ is at the 8*b* sites. The cubic unit cell consists of a lattice made up of TiO_6 octahedra and RE_4O' tetrahedra. Fig. 5-1 shows the corner sharing tetrahedral sublattices, where the rare earth (RE^{3+}) resides at the corner. Due to this special structure, the interplay between spins and lattice has a significant role in the novel properties of these frustrated geometries. For example, in $RE_2Ti_2O_7$ (RE = Gd → Yb) , depending on the interaction between the neighbouring RE spins, they exhibit geometrical frustration leading to many interesting and rather unconventional complex magnetic phenomena[6-11] like spin liquid and spin-ice effects that present challenges to the modern understanding of co-operative phenomena. Recently, the vibrational properties of some of these rare earth titanate pyrochlores $RE_2Ti_2O_7$ have been investigated by several groups.[12-19] These studies reveal that phonons in the titanate pyrochlores are highly anomalous. $Ho_2Ti_2O_7$ (HTO) and $Dy_2Ti_2O_7$(DTO), owing to their spin-ice behaviour, have been the subject of many studies.[9,11,14,20-23]

Extended x-ray absorption fine structure (EXAFS) and x-ray diffraction studies showed that HTO is well ordered and the cubic structure remains stable down to liquid helium temperature.[20,21] Recent powder x-ray diffraction and Raman studies[16] of $Dy_2Ti_2O_7$ suggested that this material undergoes a subtle structural deformation, with no change of space group, near 110 K. Since these rare earth titanates are well ordered insulating materials, the anomalous change, if any, , in phonon wave numbers and its damping with temperature is expected to arise mainly from spin-phonon anharmonic contribution (when RE is magnetic, i.e. $Sm^{3+}(4f^5)^6I_{5/2}$, $Dy^{3+}(4f^9)^6H_{5/2}$, $^5I_8$ $Ho^{3+}(4f^{10})$), crystal field-phonon coupling and phonon-phonon anharmonic effects. However, similar anomalous phonon behaviour in the nonmagnetic ($Lu^{3+}(4f^{14})^1S_0$) analogue $Lu_2Ti_2O_7$(LTO) ruled out the possibility of spin-phonon coupling.[16] From other Raman studies,[12] it was suggested that the only relevant terms to explain the temperature dependence of both linewidths and wave numbers are those due to lattice anharmonicity, either of quasiharmonic type, related to the temperature evolution of structural parameters, or true anharmonicity, arising from third- or fourth-order anharmonic decay and crystal field transitions. The anomalous phonon behaviour in these pyrochlores was attributed to a strong bond-bending character in $RE_2Ti_2O_7$ pyrochlores, and an existence of a free coordinate (the oxygen parameter *x*) that allows the distortion of TiO_6 octahedra without affecting the long-range cubic structure.[12] However, it is still not clear if the appearance of a new peak in DTO at 110K is due to local symmetry lowering (i.e. a subtle structural distortion[16]) or due to crystal field transitions.[12] It is important to mention here that since since RE^{3+} and Ti^{4+} cations occupy sites with inversion symmetry, only O and O´ atoms participate in Raman scattering. So investigations by independent techniques are necessary to address this issue. If there is a subtle distortion to the lattice, this should also be reflected in the elastic properties. Brillouin scattering, which involves acoustic phonons (long wavelength vibration of the lattice), can be an excellent probe in studying the elastic properties.

In the present study, we probe the acoustic phonons using temperature dependent Brillouin scattering from 300 to 25K to study any structural distortions in the $RE_2Ti_2O_7$ (RE= Sm, Dy, Ho and Lu). It is important to mention that $Sm_2Ti_2O_7$ (STO) is located on a borderline between the stable pyrochlore structure and the monoclinic structure of the lighter ions (La, Pr, and Nd) and LTO is nonmagnetic. So STO gives us a chance to investigate the stability of the pyrochlore lattice and LTO for investing the role of spin-acoustic phonon coupling, if any, in the temperature range of 300-25K.

5.2 Experimental details

Stoichiometric amounts of Sm_2O_3/ Ho_2O_3/ Dy_2O_3/ Lu_2O_3 (99.99%) and TiO_2 (99.99%) were mixed thoroughly and heated at 1200 °C for about 15 h. The resulting mixture was well grounded and iso-statically pressed into rods of about 8 cm long and 5 mm diameter. Rods were sintered at 1400 °C in air for about 72 h. This procedure was repeated until the compounds STO/DTO/HTO/LTO were formed, as revealed by powder x-ray-diffraction analysis. Using such rods, single crystals of STO/DTO/HTO/LTO were grown by a floating zone method using an infrared image furnace. Small cylindrical samples were cut from the resulting single crystal boules and were oxygen annealed at 1100 °C for a period of 100 h. X-ray diffraction, carried out on powder obtained by crushing part of a single crystalline sample indicated a pure pyrochlore phase. Another part of the crystal was examined by scanning electron microscope equipped with an energy dispersive x-ray analyzer. The composition of the sample was found to be very close (within 1% accuracy) to that of the starting composition. Several small crystals cut from the grown boules were checked by x-ray Laue photographs in order to determine their orientation. The samples were characterized and supplied to us by our collaborators; hence we have not provided these data here and have given the reference to their paper.[16,19]

Brillouin spectra on a (111) cut polished single-crystalline slice of STO, DTO, HTO and LTO grown using the above technique were recorded in the back-scattering geometry with an incident angle $\theta_i = 55^o$ with respect to the surface normal. The p-polarised 532 nm line of single mode solid-state diode pumped frequency doubled Nd:YAG laser (Model COMPASS 315M-150, Coherent Inc., USA) was used as the excitation source. The scattered light was analyzed using a 3+3 pass tandem Fabry-Perot interferometer (JRS Scientific Inc., Switzerland), which has a finesse ~ 100 and is equipped with a photo avalanche diode (Perkin Elmer, Canada) as the detector. The spectra were collected at a free spectral range of 75 GHz, equivalent to an etalon spacing of 2 mm. Temperature-dependent measurements were carried out using a closed cycle helium cryostat (CTI Cryogenics, USA). The sample temperature was measured with an accuracy of ±1 K. The line-shape parameters-peak frequency, ω, full width at half maximum (FWHM) Γ, and intensity were extracted by a non-linear least square fitting of the data with a Lorentzian function, along with an appropriate background.

5.3 Results and discussions

Fig. 5-2 shows the typical room temperature Brillouin spectra from STO, DTO, HTO and LTO. We could observe both longitudinal acoustic (LA) and transverse acoustic (TA) modes. We observed the splitting in the TA mode into TA_1 and TA_2 for DTO, HTO and LTO, whereas we couldn't see any splitting in case of STO. The Laue diffraction pattern (see Fig. 5-3) for DTO did not reveal the expected 3-fold symmetry (as is the case for (111) plane), suggesting that the orientation is slightly different than (111), even though the attempt was to cut the crystal along (111) direction. This is also true in the case of HTO and LTO. The origin of splitting in the TA mode in these systems could be due to this reason.

Velocities V_i of the observed transverse and longitudinal acoustic phonons propagating in ~ [111] direction were determined. These velocities were deduced from the measured Brillouin shift $\Delta\omega_B$ using the equation discussed in Chapter 1, namely, $\Delta\omega_B = 2nk_iV_i\sin\left(\frac{\theta_i}{2}\right)$, where $\Delta\omega_B$ is the Brillouin shift, k_i is the wave vector of incident light, n is the refractive index of the crystal and θ_i is the scattering angle. In the case of back scattering (θ_i =180°), the above relation for velocity becomes $V_i = 2nk_i / \Delta\omega_B$. In determining the velocities, we have taken the refractive index values given elsewhere[24] and they were assumed to be constant over the entire temperature interval. However, it must be pointed that the actual aim of this work is not to determine the absolute values of velocities at various temperature, but to see its behavior with temperature. Hence there is a small uncertainty in values of velocities calculated arising due to the error in the value of q due to the assumption made in the case of the refractive index.

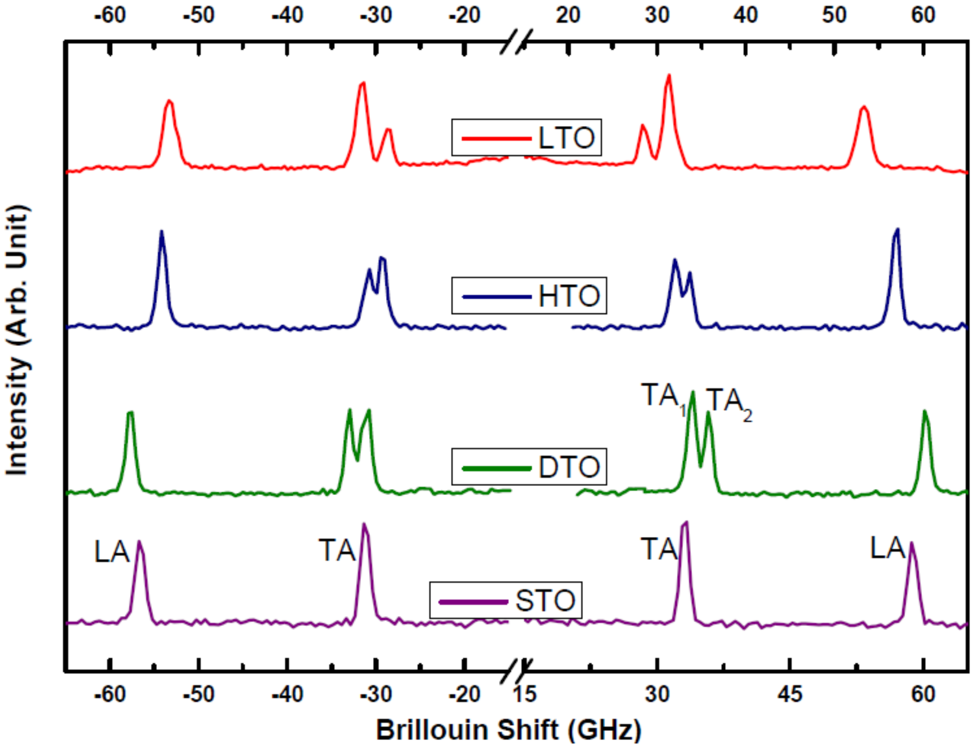

Figure 5-2: Room temperature Brillouin spectra of STO, DTO, HTO and LTO

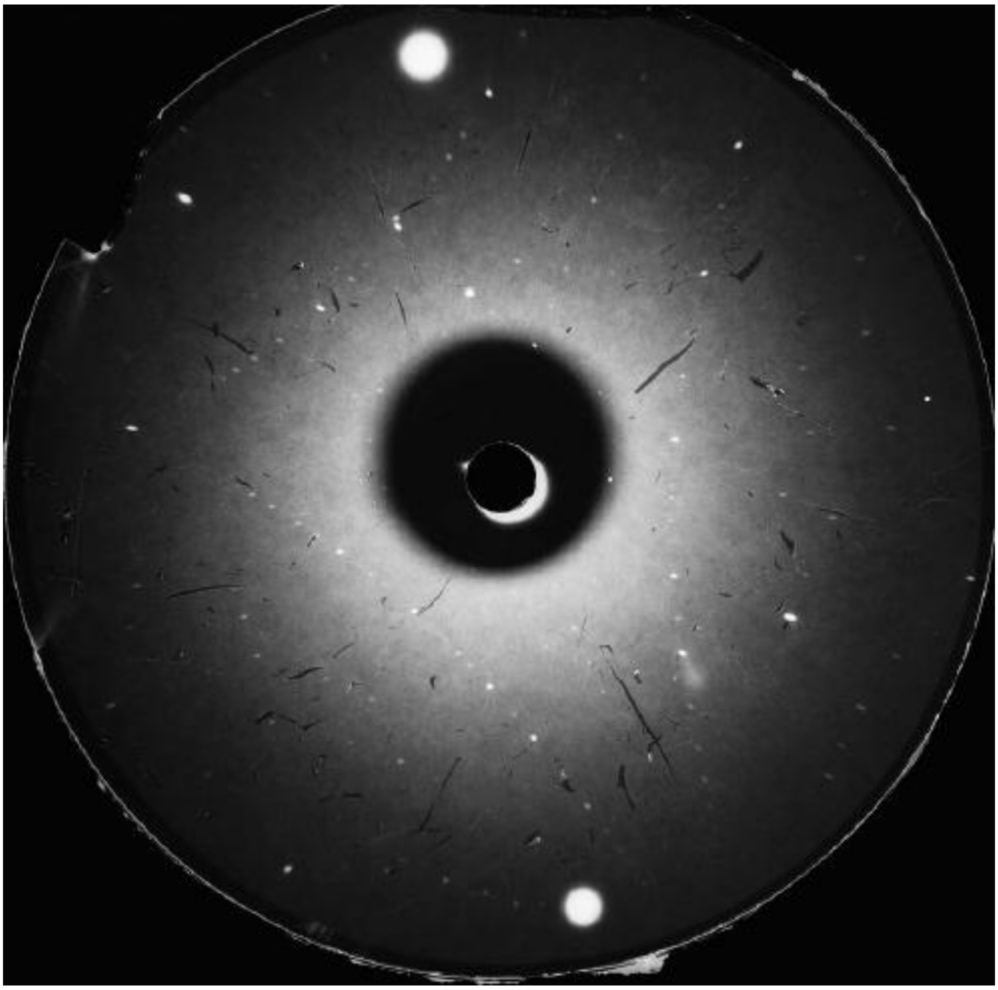

Figure 5-3: Laue photograph of DTO

Figs. 5-4, 5-5, 5-6 and 5-7 shows representative temperature evolution of the Brillouin spectra for STO, DTO, HTO and LTO. It should be noted that the spectral resolution is around 0.1 GHz. The sound velocities of both transverse and longitudinal phonons can be calculated at each temperature. We show the temperature dependence of the sound velocities in Fig. 5-8, 5-9 and 5-10.

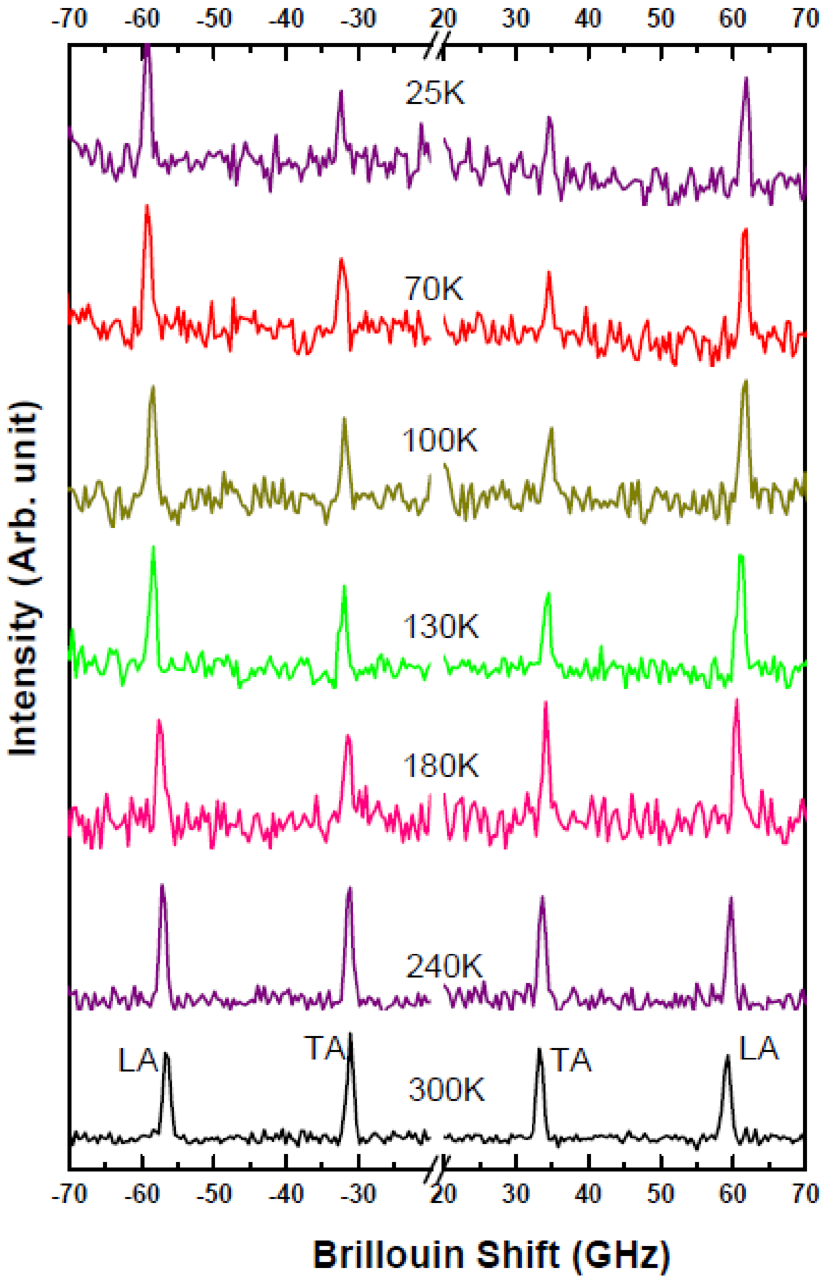

Figure 5-4: Temperature evolution of the Brillouin spectra of STO

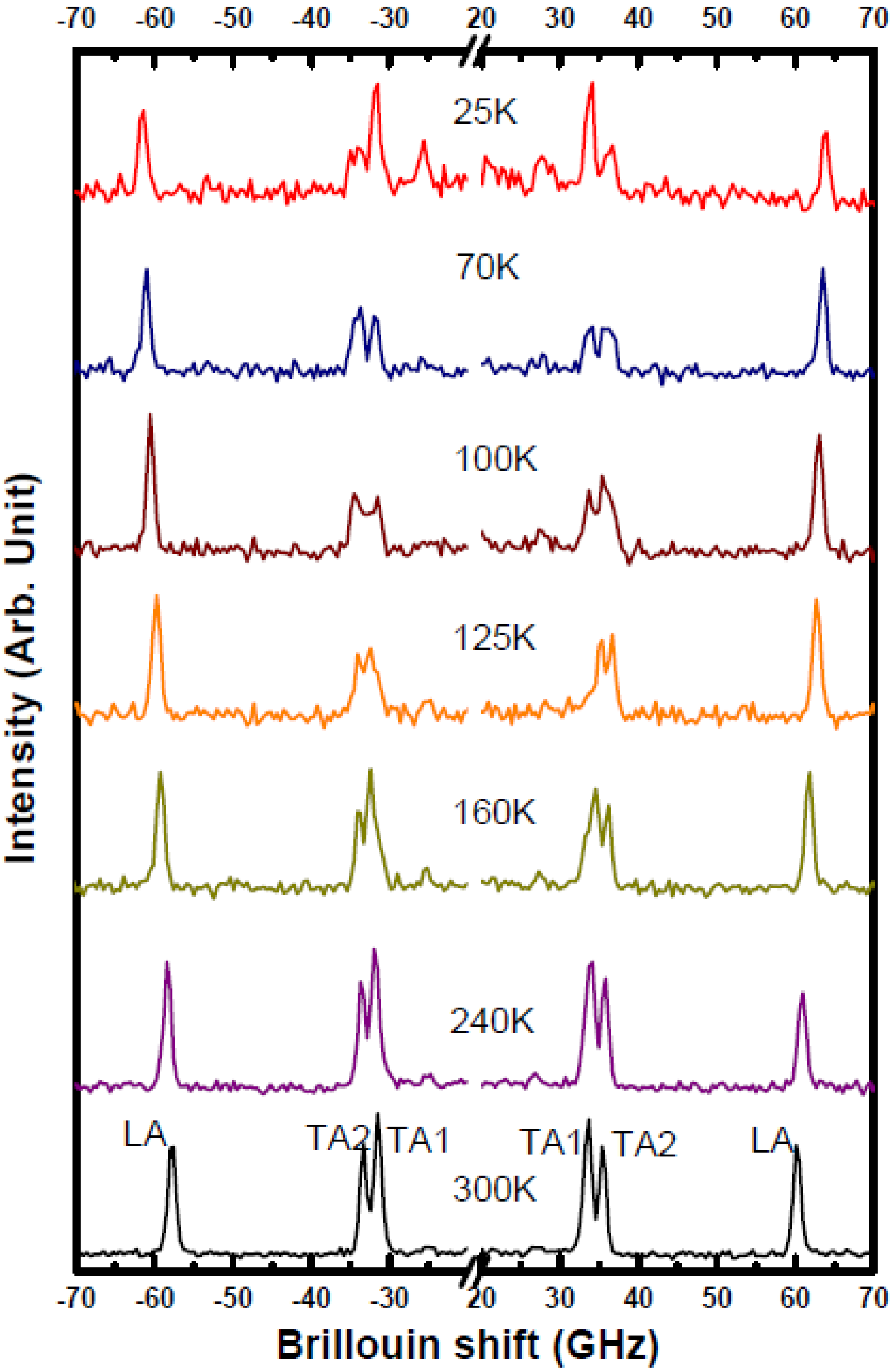

Figure 5-5: Temperature evolution of the Brillouin spectra of DTO

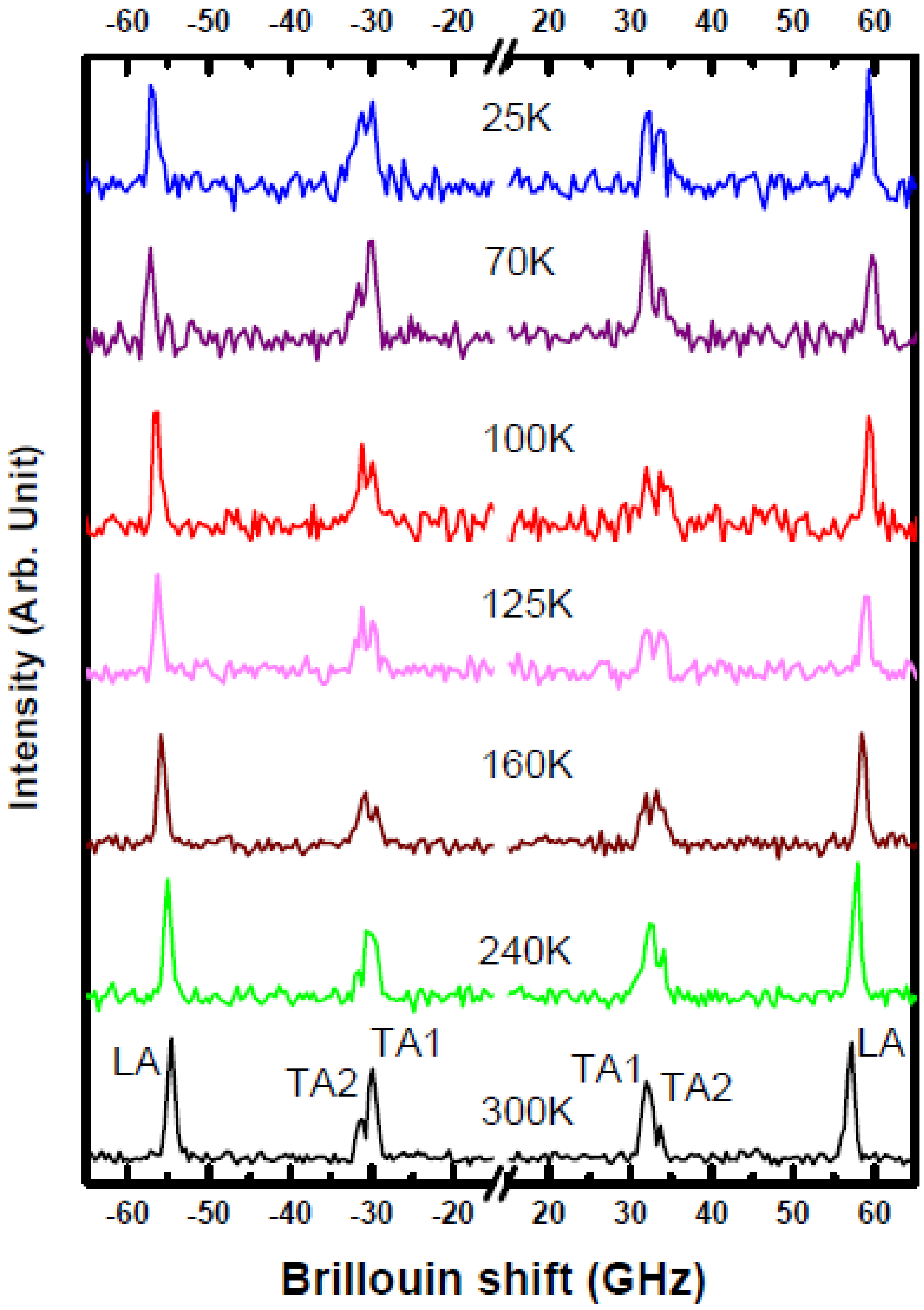

Figure 5-6: Temperature evolution of the Brillouin spectra of HTO

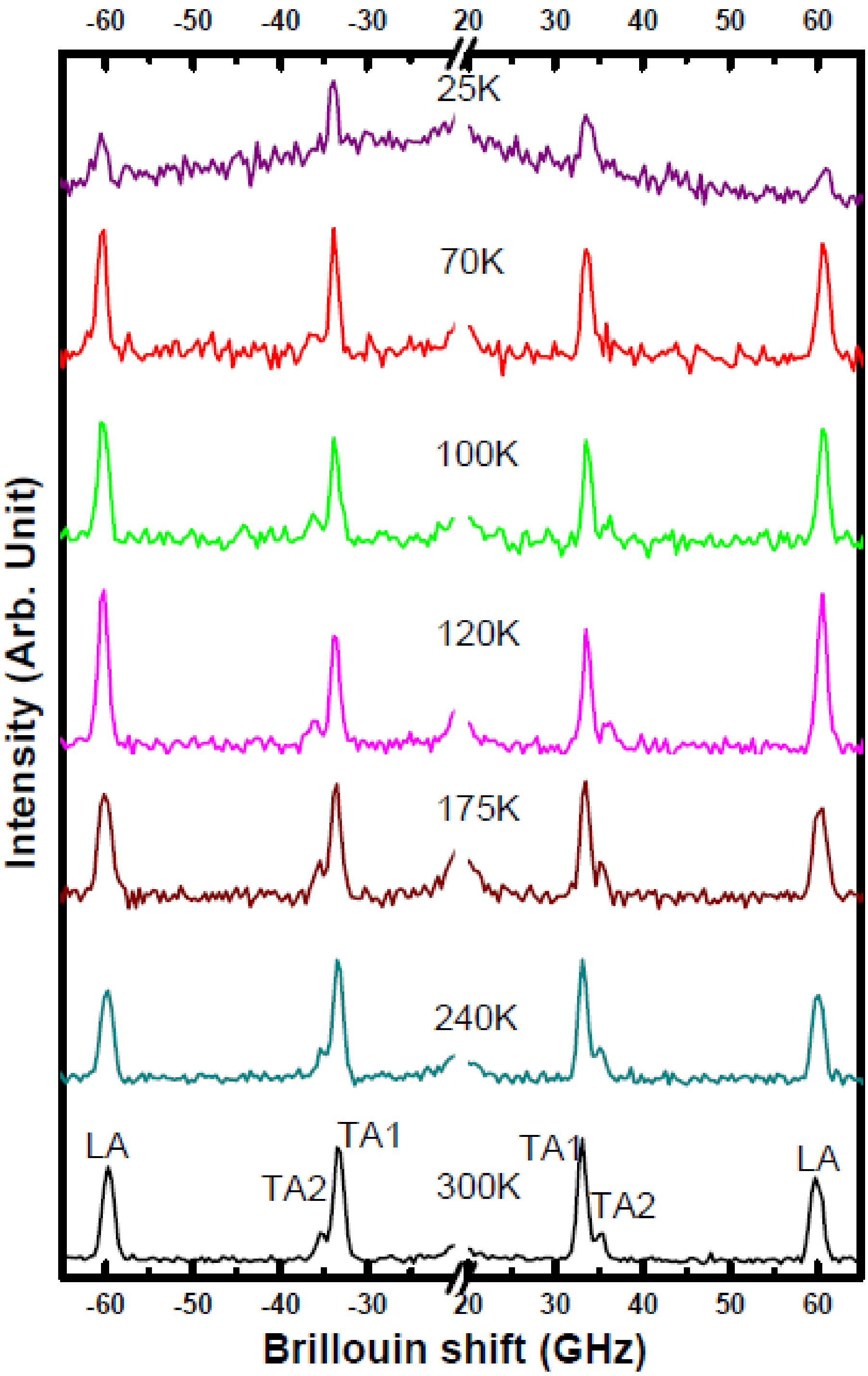

Figure 5-7: Temperature evolution of the Brillouin spectra of LTO

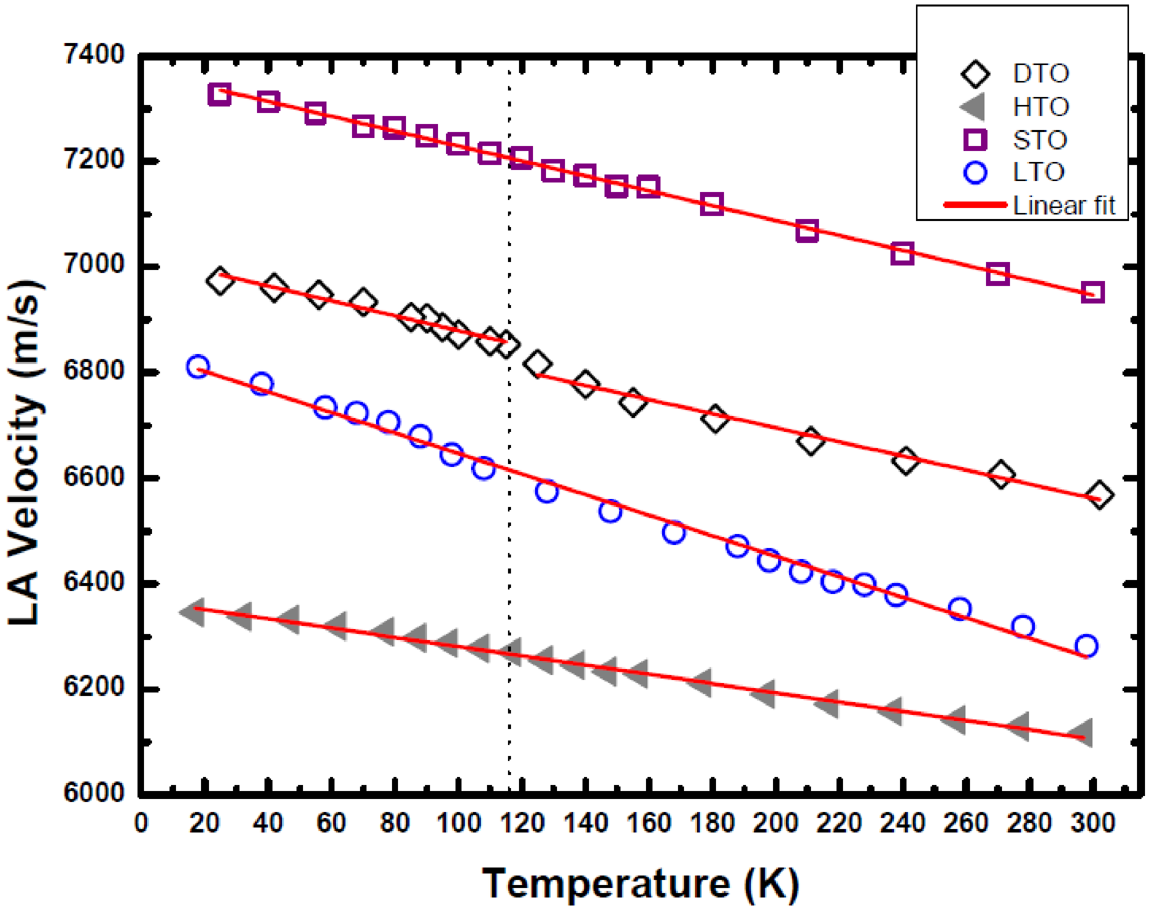

Figure 5-8: Longitudinal sound velocities of STO, DTO, HTO and LTO as a function of temperature. Solid lines are the linear fit to the data.

The solid line shown in Fig. 5-8, 5-9 and 5-10 are linear fit to the data points, given by $(V_s(T) = V_0 + aT)$ to the data points. $V_s(T)$ is the sound velocity at temperature T, V_0 is the room temperature sound velocity and a is a constant. It can be clearly seen from Fig. 5-8 that there is a discontinuity in the LA velocity at around 110K for the case of DTO. On the other hand, STO, HTO and LTO show no anomaly/discontinuity (see Fig. 5-9) over the entire temperature range. The same is true for the TA velocities.

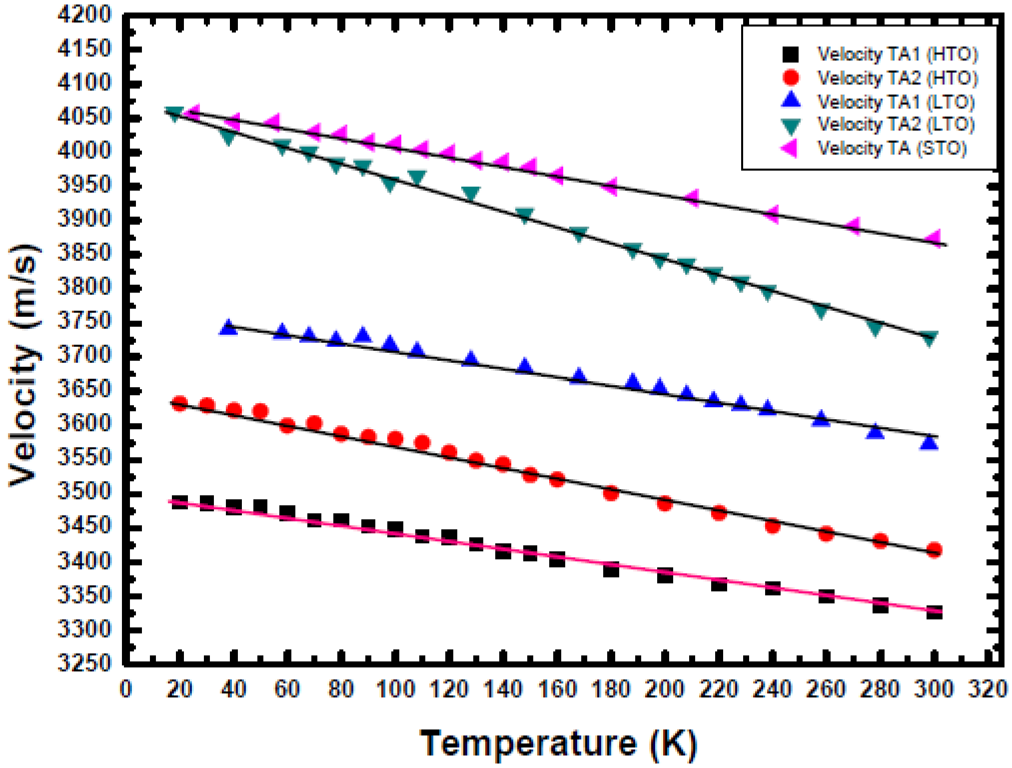

Figure 5-9 : Transverse sound velocities of STO, HTO and LTO as a function of temperature. Solid lines are the linear fit to the data

Fig. 5-10 shows the temperature dependence of the TA_1 and TA_2 phonon velocity in the case of DTO. The TA sound velocities clearly mimic the LA sound velocities in the case of DTO. It is interesting to observe that, like, in the Raman experiments the effect is manifested in long wavelength regime also.[16] Since STO and LTO do not show any changes through the temperature range of 300 to 25 K, it is clear that the effect seen in DTO is neither driven due to spin-acoustic phonon coupling in pyrochlore nor instability in the pyrochlore structure. HTO and DTO are spin ice systems and HTO behaves similar to DTO, suggests that the anomalous behavior in the case of DTO cannot be associated due to the spin-ice effects. Hence it is safe to assume that DTO's anomalous behaviour is driven due to the subtle structural transition observed around 110 K as seen in both x-ray as well as Raman experiments.[16] This in fact clears a lot of discrepancy in the literature associated with the disorder-order transition expected due to spin frustration in these system and suggests that the low temperature phase is still a disordered phase due to the spin frustrations present in the system.

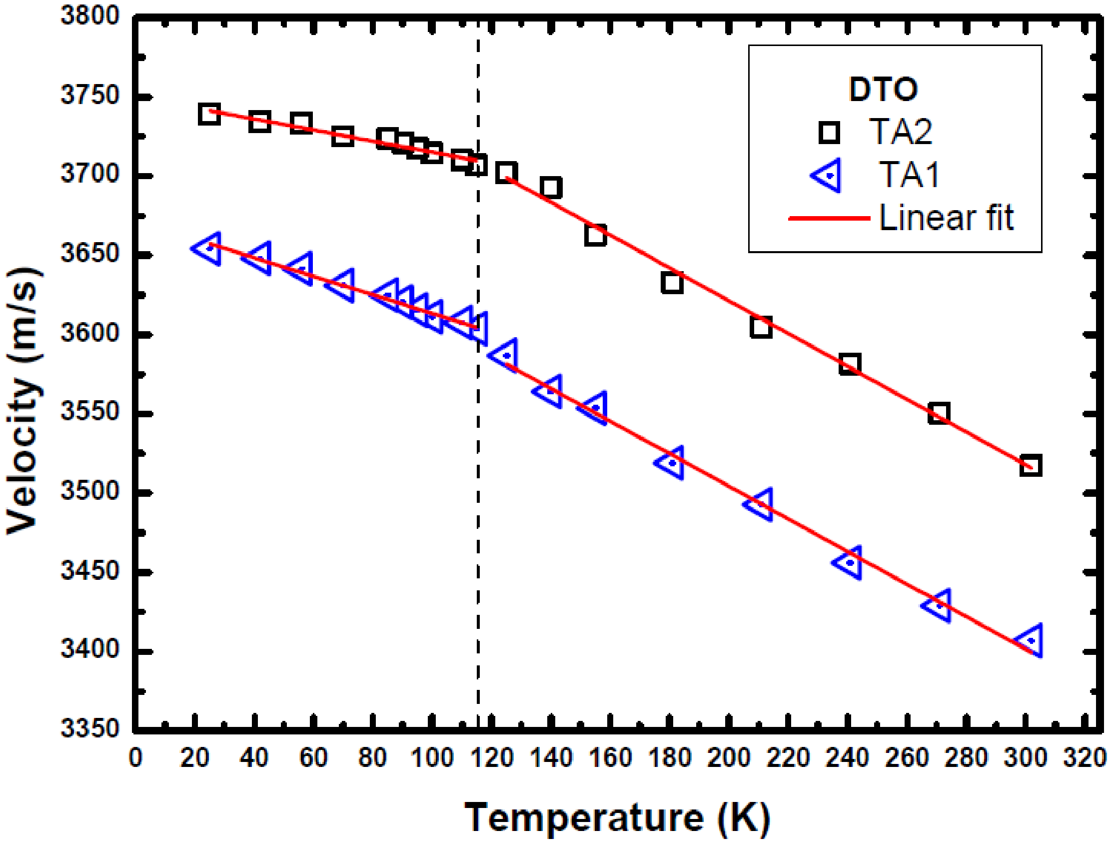

Figure 5-10: Transverse sound velocities of DTO as a function of temperature.

5.4 Conclusion

In summary, we have carried out temperature dependent Brillouin scattering studies in $RE_2Ti_2O_7$ (RE= Sm, Dy, Ho and Lu) from 300 to 25K. We have studied the temperature dependence of the sound velocities in these systems and from the acoustic anomaly in DTO we confirm that it is driven purely by a subtle structural change at ~110K. STO, HTO and LTO don't show any structural transitions in this temperature range, suggesting that there is no ordering at low temperatures up to 25 K.

5.5 References

1. D. P. Cann, C. A. Randall, and T. R. Shrout, Solid State Communications **100,** 529 (1996).
2. R. Vassen, X. Cao, F. Tietz, D. Basu, and D. Stiver, Journal of the American Ceramic Society **83,** 2023 (2000).
3. B. J. Wuensch, K. W. Eberman, C. Heremans, E. M. Ku, P. Onnerud, E. M. E. Yeo, S. M. Haile, J. K. Stalick, and J. D. Jorgensen, Solid State Ionics **129,** 111 (2000).
4. R. C. Ewing, W. J. Weber, and J. Lian, Journal of Applied Physics **95,** 5949 (2004).
5. M. A. Subramanian, G. Aravamudan, and G. V. Subba Rao, Progress in Solid State Chemistry **15,** 55 (1983).
6. J. S. Gardner, B. D. Gaulin, A. J. Berlinsky, P. Waldron, S. R. Dunsiger, N. P. Raju, and J. E. Greedan, Physical Review B - Condensed Matter and Materials

Physics **64,** 2244161 (2001).

7. S. W. Han, J. S. Gardner, and C. H. Booth, Physical Review B - Condensed Matter and Materials Physics **69,** 244161 (2004).
8. K. C. Rule, et al., Phys. Rev. Lett. **96,** 177201 (2006).
9. S. T. Bramwell, et al., Physical Review Letters **87,** 472051 (2001).
10. A. P. Ramirez, A. Hayashi, R. J. Cava, R. Siddharthan, and B. S. Shastry, Nature **399,** 333 (1999).
11. T. Fennell, O. A. Petrenko, B. Frak, S. T. Bramwell, M. Enjalran, T. Yavors'Kii, M. J. P. Gingras, R. G. Melko, and G. Balakrishnan, Phys. Rev. B **70,** 134408 (2004).
12. M. Maczka, M. L. Sanju+ín, A. F. Fuentes, L. MacAlik, J. Hanuza, K. Matsuhira, and Z. Hiroi, Physical Review B - Condensed Matter and Materials Physics **79,** (2009).
13. M. Maczka, M. L. Sanjuan, A. F. Fuentes, K. Hermanowicz, and J. Hanuza, Phys. Rev. B **78,** 134420 (2008).
14. T. T. A. Lummen, I. P. Handayani, M. C. Donker, D. Fausti, G. Dhalenne, P. Berthet, A. Revcolevschi, and P. H. M. Van Loosdrecht, Phys. Rev. B **77,** 214310 (2008).
15. S. Saha, et al., Physical Review B - Condensed Matter and Materials Physics **74,** (2006).
16. S. Saha, S. Singh, B. Dkhil, S. Dhar, R. Suryanarayanan, G. Dhalenne, A. Revcolevschi, and A. K. Sood, Phys. Rev. B **78,** 214102 (2008).
17. S. Saha, et al., Phys. Rev. B **74,** 064109 (2006).

18. S. Saha, et al., Phys. Rev. B **79,** 134112 (2009).
19. S. Singh, S. Saha, S. K. Dhar, R. Suryanarayanan, A. K. Sood, and A. Revcolevschi, Phys. Rev. B **77,** 054408 (2008).
20. L. G. Mamsurova, K. K. Pigalskii, N. G. Trusevich, and L. G. Shcherbakova, Sov. Phys. Solid State **27,** 978 (1985).
21. G. Ehlers, et al., Phys. Rev. B **73,** 174429 (2006).
22. M. J. Harris, S. T. Bramwell, D. F. McMorrow, T. Zeiske, and K. W. Godfrey, Physical Review Letters **79,** 2554 (1997).
23. M. Kanada, et al., Journal of the Physical Society of Japan **71,** 313 (2002).
24. L. G. Shcherbakova et al 48 ed., 1979), p. 228.

Chapter 6[*]

Inelastic Light Scattering from the Acoustic Modes of Double Walled Carbon Nanotubes

A paper based on this work has been communicated to Journal of Physics Condensed Matter.

---

[*] The author's main contribution in this chapter is in doing the Brillouin scattering experiments, analyzing and interpreting the data. The problem was formulated by Ajay K. Sood of Indian Institute of Science, Banagalore, India. The samples used in this study were synthesized by Alexander Moravsky and R. O. Loutfy of Materials and Electrochemical Engineering Research Corporation, Tucson, AZ, USA.

6.1 Introduction

Among the many synthesized carbon nanostructures, nanotubes[1] have proved to be the most interesting from the materials science viewpoint, due to their remarkable physical properties structural, electronic, and mechanical properties.[2] Carbon nanotube (CNT) constitutes a new form of carbon allotropes with unique and exotic physical properties. CNTs are tubular structures typically of nanometer diameter and many microns in length. They are unusual because of their very small diameters, which can be as small as 0.4 nm and contain only 10 atoms around the circumference, and because the tubes can be only one atom in thickness. The aspect (length/diameter) ratio can be very large (greater than 10^4), thus leading to a prototype one-dimensional system. These structures were first observed by Iijima[1] in the soot produced in the arc discharge synthesis of fullerenes. Carbon nanotubes promise applications in such varied fields as nanoelectronics, actuators,[3] sensors,[4] nanofluidics, hydrogen storage, and high-strength materials.

A single walled carbon nanotube (SWCNT) can be constructed by wrapping a single sheet of graphene into a seamless cylinder, one atom thick, usually with a small number of carbon atoms along the circumference and a long length (microns) along the cylinder axis.[2,5] The wrapping or the chiral vector ($C_h = \mathrm{n}a_1 + \mathrm{m}a_2$), or (n,m), where a_1 and a_2 are the unit vectors in the 2-D graphene sheet and n and m are integers, determines the symmetry of the SWCNT (see Fig. 6-1). This leads to three types of nanotubes depending on the values of n and m: the arm chair nanotubes where n = m, zigzag nanotubes where m=0, and chiral nanotubes where $n \neq m \neq 0$. A nanotube is metallic when n – m is divisible by 3, otherwise it is semiconducting. The diameter of nanotube is related to the (n, m) values by,

$d = a\sqrt{\left(\mathrm{n}^2 + \mathrm{m}^2 + \mathrm{nm}\right)}/\pi$, where the lattice constant on a graphene sheet a is taken to be 2.49 Å on a rolled up nanotube cylinder. Carbon nanotubes can exist in a variety of structures corresponding to the arrangement of the tubes. If two or more than two SWCNTs are arranged coaxially then they are known as doublewalled carbon nanotubes (DWCNT) or Multiwalled carbon nanotubes (MWCNT), respectively.

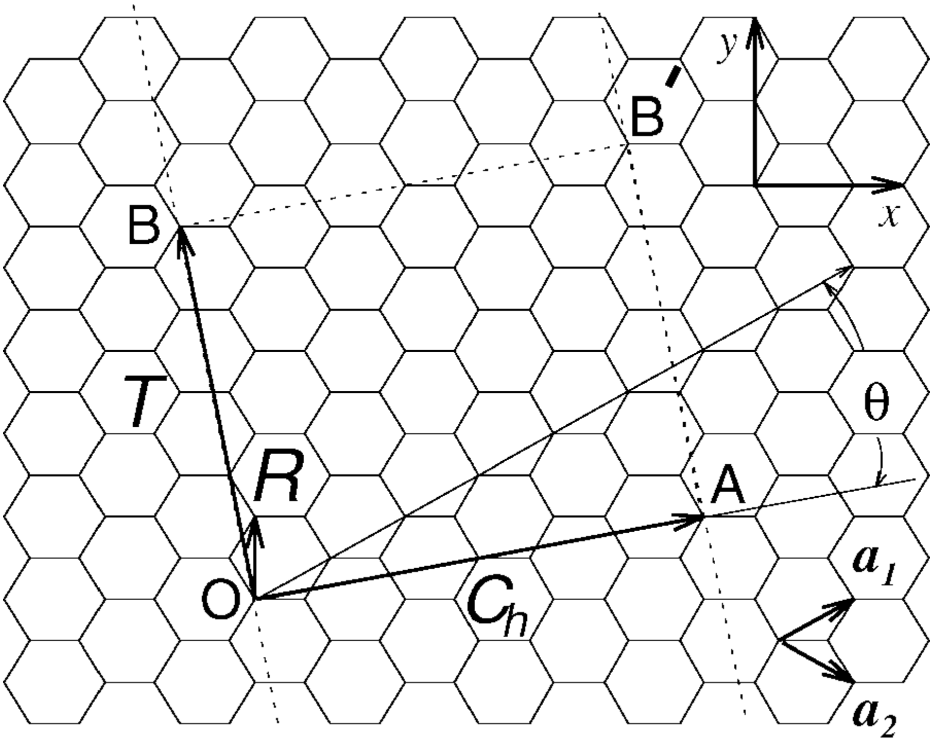

Figure 6-1: The unrolled graphene sheet (honeycomb lattice). When we connect sites O and A, and sites B and B′, a nanotube can be constructed. The vectors OA and OB define the chiral vector C_h and the translational vector T of the nanotube, respectively. The rectangle OABB′ defines the unit cell for the nanotube.

Since the discovery[1] of carbon nanotubes (CNTs), their mechanical properties have been the subject of a number of theoretical[6-11] as well as experimental studies.[12,13] Due to their specific structure, CNT's are predicted to be as stiff as graphite along the graphene layers or even reach the stiffness of diamond. This unique high stiffness along with low density make them suitable candidates for their use as nanoscale fibers in strong, light weight composite materials, high strength cables, actuators, etc and has motivated precise determination of their elastic properties.[12,13] Single wall carbon nanotubes (SWCNT) and Multiwalled carbon nanotubes (MWCNT) have been intensively studied during the past decade, however, in more recent years, increasing attention is being given to double-wall carbon nanotubes (DWCNTs) since they can be regarded as the simplest example of MWCNTs, also they bridge the gap between SWNTs and MWNTs and and thus can be studied quantitatively and systematically. Also, DWCNTs are promising for technological applications due to their robustness while retaining many of the highly desirable single-wall nanotube properties. DWCNT based molecular bearings have been proposed[14] as a fascinating candidate for MEMS and NEMS application. Also, the potential barrier to relative displacements of layers has been calculated and mechanical nano-devices based on bolt-nut pair-like motions of the layers have been proposed.[15] Recent methods[16,17] for producing high purity DWCNTS have opened new opportunities for detailed investigations on these systems.

Resonant Raman measurements from optical modes have been performed on DWCNT,[18-20] but, however, no acoustic vibrational properties measurement has been reported except studies on the acoustic phonons of magnetically aligned SWCNTs.[21] More recently, several workers have used high pressure Raman spectroscopy to study bundles of DWCNTs.[22,23] From the high pressure Raman experiments and molecular dynamics simulations,[22,23] Gadagkar *et al* have shown that the collapse pressure (p_c) of a given DWCNT bundle is greater than the p_c of both inner and the outer tubes considered as SWCNT bundles and a two fold increase in the bending stiffness of the DWCNTs as compared to SWCNT has been suggested. In addition, a two fold increase in the bending stiffness of the DWCNTs has been suggested as compared to SWCNTs

In this work, we report the first Brillouin Scattering (BS) studies from the bulk acoustic phonon modes of randomly oriented DWCNT bundles. BS is the inelastic scattering of light by acoustic phonons. Knowledge of sound velocities from the corresponding Brillouin shift, gives information of the elastic properties of a material. BS doesn't involve any non-elastic deformations during the process of measurement. It has advantages over other methods, such as the surface acoustic wave (SAW), hydrostatic pressure methods or the ultrasonic attenuation technique, as BS is a contact less measurement and probes materials in thermal equilibrium conditions, not requiring external excitation of the acoustic modes.

6.2 Experimental details

Brillouin scattering experiments were done on a sample of DWCNT, which was grown using high temperature chemical vapour deposition (CVD) and deposited on PARAFILM® "M". Electron microscopy images in Figs. 6-2, 6-3 and 6-4 illustrate the structure and bundling of the as-produced CVD DWCNT used in this work. The tubes obtained under standard production conditions are about 2.2 nm in diameter on the average, with ~0.5 nm width of diameter distribution, as assessed by TEM (see Fig. 6-4). The as produced material contains predominantly relatively thin DWCNT bundles, comprising 5–15 tubes, and also some individual tubes (~20% of the number of bundles). Bundles were found to be about 25 nm long, by SEM measurements. The as-produced DWCNT are more than 90 wt% pure in carbon, the rest 10% is represented by amorphous carbon and low volatile organic coating of the tube surface. The fraction of similar diameter SWCNT contained in the as-produced DWCNT material obtained under standard conditions does not exceed 3%. That is, the ratio of the number of DWCNT to SWCNT is >30. The nanotubes were separated from the PARAFILM® "M" by vigorously shaking the nanotube coated film in chloroform. Once the sample was separated from the film, it was washed several times in chloroform to remove any part of the film that might be still sticking to the sample.

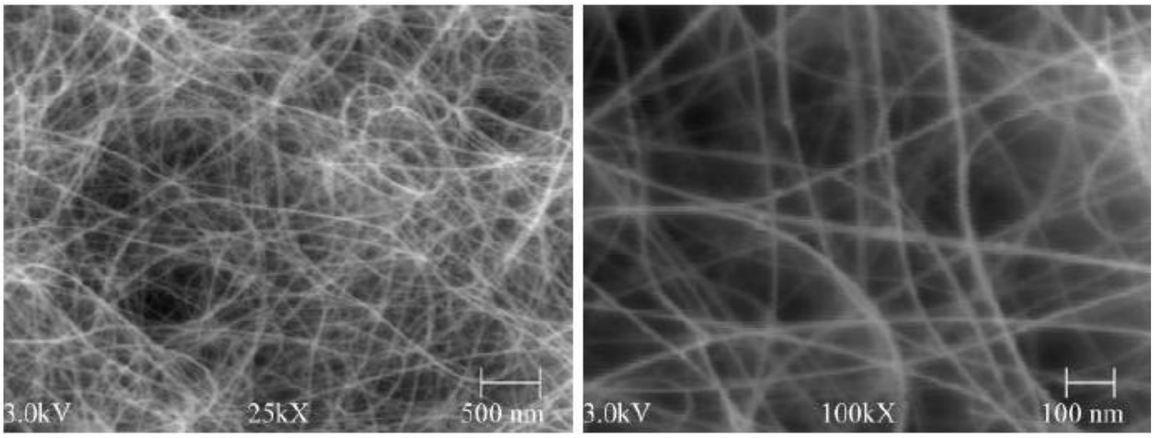

Figure 6-2: High resolution SEM micrograph of as-produced CVD DWCNT matted film used in the work.

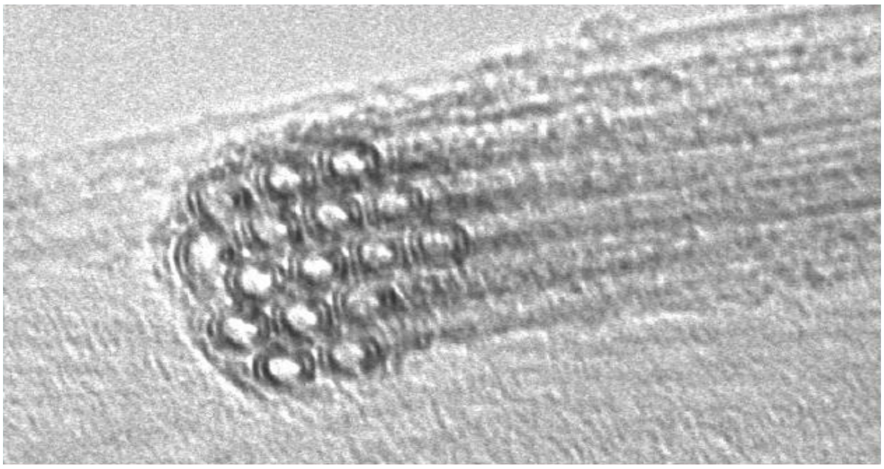

Figure 6-3: HRTEM Micrograph of a cross section of a CVD DWCNT bundle, with individual tubes about 2.2 nm in diameter.

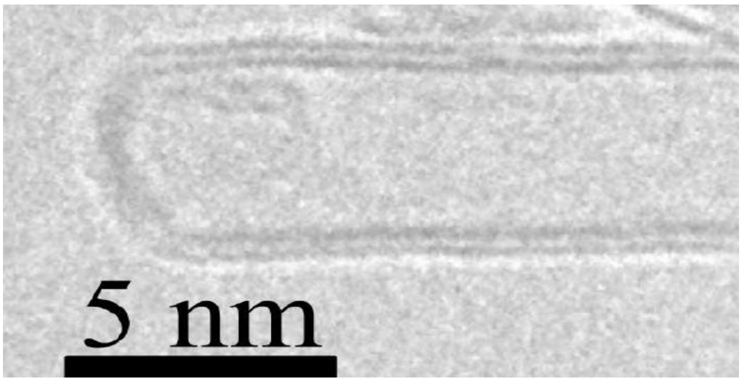

Figure 6--4: HRTEM Micrograph of a single DWCNT end

Brillouin spectra were recorded in backscattering geometry, using a 532 nm p-polarized light beam from a single-mode diode pumped Nd-YAG laser (Coherent, USA, Model No. DPSS 532-400). A low laser power (20mW) was used to avoid laser damages.

However, long accumulation times (~ 2 to 3 hours) were required to produce the spectrum. Scattered light was analyzed without polarization selection using a Sandercock-type 3+3 pass tandem Fabry–Perot interferometer, which has a finesse ~ 100 and is equipped with a photo avalanche diode (Perkin Elmer, Canada) as the detector. The spectra were collected at a free spectral range of 150 GHz, equivalent to an etalon spacing of 1 mm. Scattered light was collected at different incidence angles (θ_i) in order to vary the scattered wave vectors. Scattered light was also collected (see Fig. 6-5) for different azimuthal rotations (φ) along the surface normal keeping the angle of incidence fixed, in order to see any orientation dependence of the tubes.

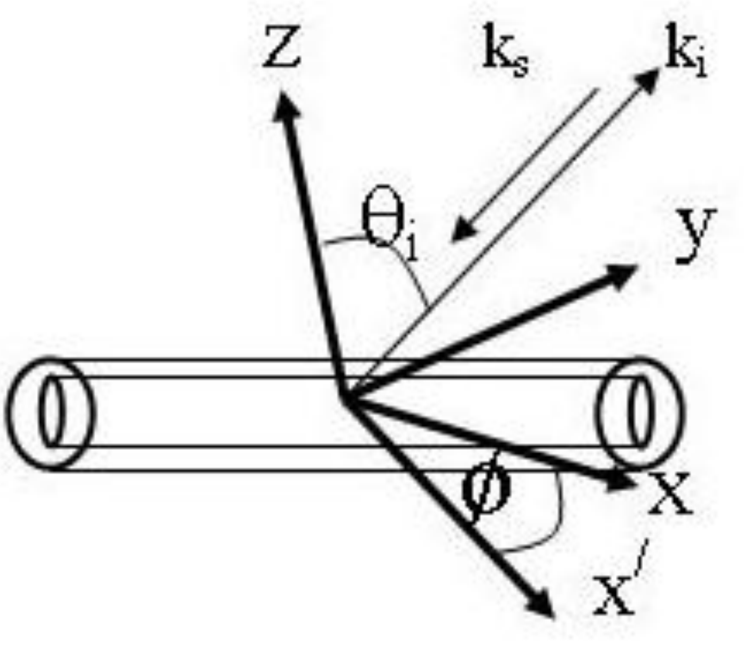

Figure 6-5: Schematic representation of the experimental geometry

6.3 Results and discussion

Fig. 6-6 shows a typical Brillouin spectrum of the DWCNT. The solid line is a Lorentzian fit with an appropriate background to the observed data points. The frequency (ν_B) of this mode was found to be ~ 53.4 GHz.

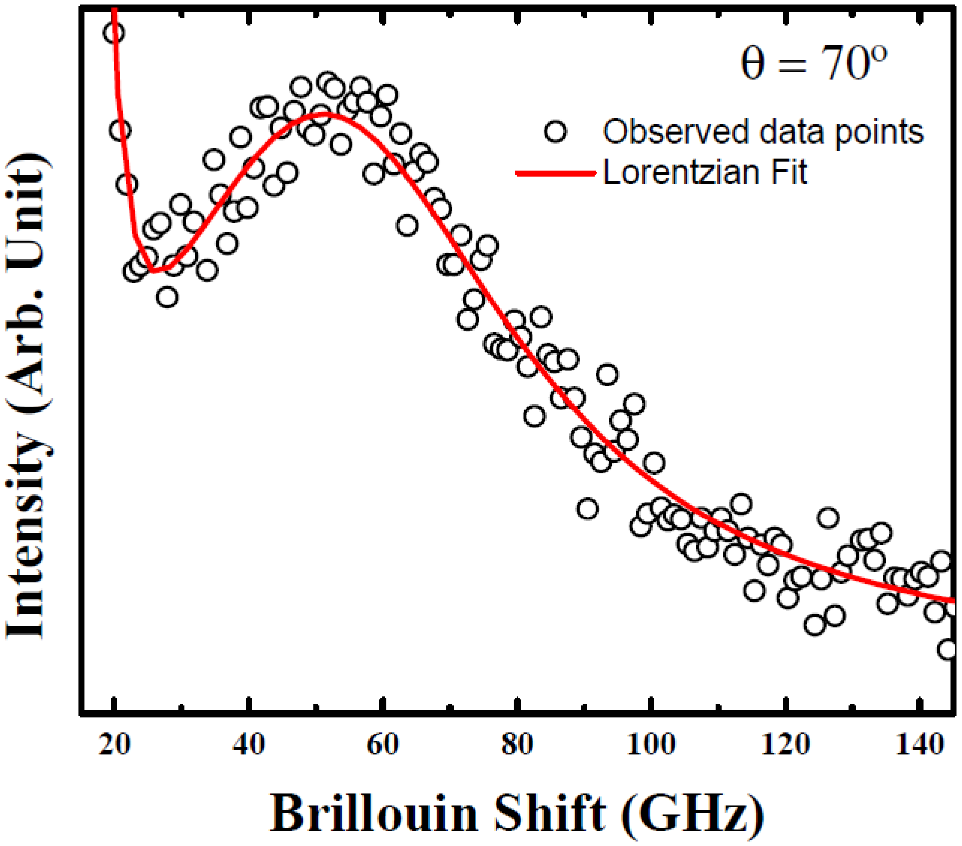

Figure 6-6: Anti-Stokes Brillouin spectra of DWCNT. The solid line is a Lorentzian fit.

This value of the measured frequency shift ν_B was used to obtain the sound velocity, V_S, using the relationship: $\nu_B = \pm\frac{2n}{\lambda}V_S \sin\left(\frac{\theta}{2}\right)$, where λ (= 532 nm) is the laser wavelength, θ (=180°) is the scattering angle and n is the effective refractive index. If all the tubes are aligned in the horizontal plane of the surface of the substrate, one expects anisotropy in the Brillouin shift by rotating the sample surface about the incident angle. From Fig. 6-7 it is interesting to note that for the same angle of incidence $\theta_i = 70^o$, no significant change occurs to the mode frequency and intensity for different in-plane orientations (φ), showing no preferential alignment of the tubes along any particular directions. This is consistent with the SEM micrographs shown in Fig. 6-2 suggesting the random orientations of the DWNT bundles. As discussed by Bottani *et al*[21] in the case of SWCNTs, the Brillouin scattering results in the case of DWNTs also can be understood as a surface elasto-optic effect which couples with the incident light to the thermal strains of both the inner and outer tube of the DWCNT giving rise to the bulk acoustic modes.

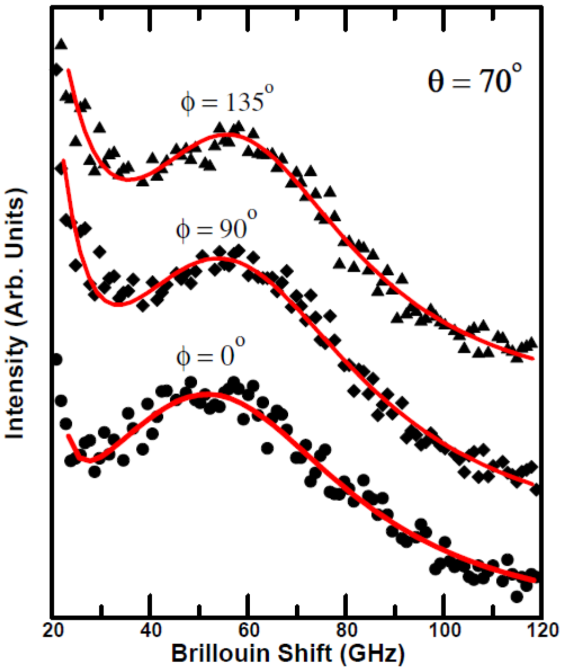

Figure 6-7: Brillouin spectra for different azimuthal rotations (φ) along the surface normal.

The unusually broad acoustic modes suggest that there is a possibility of damping of the acoustic phonons due to lack of long range alignment perpendicular to the tube axis and no preferred orientation. It could also be a combination of both longitudinal as well as transverse acoustic mode, coexisting. Using the relationship between the Brillouin shift and the sound velocity of the DWCNT mentioned above, the sound velocity of the observed bulk acoustic mode was found be 13.528 km s^{-1}. Please note that, in calculating this, we have used the effective refractive index (n) value of 1.05 observed in the case of CNT layers.[24] It is important to mention that from the lattice dynamical calculations by Damnjanovic et al,[25] the sound velocities of the longitudinal acoustic (LA) and the doubly degenerate transverse acoustic (TA) mode were found to be V_{LA} = 20.64 km s^{-1} and V_{TA} = 9.54 km s−1, respectively. It is interesting to note that the sound velocities measured in our experiments do not match with either LA or TA sound velocities predicted by these calculations. If one assumes that the acoustic mode observed here is neither a pure LA nor pure TA, but a combination mode due to its random arrangements, then the sound velocity should be given by $1/3(2V_{\mathrm{TA}}+V_{\mathrm{LA}})$. The average bulk acoustic sound velocity was found to be 13.24 km s^{-1} using the reported sound velocity of the pure acoustic branches from the lattice dynamic calculations. This is in excellent agreement with our experimental bulk acoustic mode sound velocity. If one could align these tubes into a compact layer, there is a possibility to elucidate the sound velocities of the pure branches from the Brillouin experiments, which would be consistent with theory.

6.4 Conclusion

In summary, we have carried out Brillouin light scattering measurements on randomly aligned DWCNT. As can be observed that these experiments have been performed for the first time on high quality DWCNTs and the measurements were very difficult to perform. We have observed the bulk acoustic phonon modes of DWCNTs for the first time using Brillouin Scattering experiments. Our bulk mode sound velocity is in excellent agreement with the lattice dynamic calculations and suggests that isotropic nature of the samples provides us with the average elastic property of the DWCNTs. The values thus obtained suggest that the tube-tube interactions in the DWCNT bundles are weak and don't change the elastic properties significantly.

6.5 References

1. S. Iijima, Nature **354,** 56 (1991).
2. R. Saito, G. Dresselhaus, and M. S. Dresselhaus, Physical Properties of Carbon Nanotubes, Imperial College Press, London (1998).
3. R. H. Baughman, et al., Science **284,** 1340 (1999).
4. S. Ghosh, A. K. Sood, and N. Kumar, Science **299,** 1042 (2003).
5. M. S. Dresselhaus and P. C. Eklund, Advances in Physics **49,** 705 (2000).
6. B. I. Yakobson, C. J. Brabec, and J. Bernholc, Physical Review Letters **76,** 2511(1996).
7. E. W. Wong, P. E. Sheehan, and C. M. Lieber, Science **277,** 1971 (1997).

8. V. N. Popov, V. E. Van Doren, and M. Balkanski, Solid State Communications **114,** 395 (2000).

9. J. P. Lu, Physical Review Letters **79,** 1297 (1997).

10. J. P. Lu, Journal of Physics and Chemistry of Solids **58,** 1649 (1997).

11. V. N. Popov, V. E. Van Doren, and M. Balkanski, Physical Review B **59,** 8355 (1999).

12. M. M. J. Treacy, T. W. Ebbesen, and J. M. Gibson, Nature **381,** 678 (1996).

13. A. Krishnan, E. Dujardin, T. W. Ebbesen, P. N. Yianilos, and M. M. J. Treacy, Physical Review B **58,** 14013 (1998).

14. S. Zhang, W. K. Liu, and R. S. Ruoff, Nano Letters **4,** 293 (2004).

15. R. Saito, R. Matsuo, T. Kimura, G. Dresselhaus, and M. S. Dresselhaus, Chemical Physics Letters **348,** 187 (2001).

16. A. P. Moravsky, E. M. Wexler, and R. O. Loutfy, Carbon Nanotubes: Science and Applications, edited by M. Meyyappan, CRC Press, Boca Raton , Ch. 3 65 (2005).

17. J. L. Hutchison, et al., Carbon **39,** 761 (2001).

18. J. M. Benoit, J. P. Buisson, O. Chauvet, C. Godon, and S. Lefrant, Physical Review B **66,** 734171 (2002).

19. S. Bandow, M. Takizawa, K. Hirahara, M. Yudasaka, and S. Iijima, Chemical Physics Letters **337,** 48 (2001).

20. S. Bandow, G. Chen, G. U. Sumanasekera, R. Gupta, M. Yudasaka, S. Iijima, and P. C. Eklund, Physical Review B **66,** 754161 (2002).

21. C. E. Bottani, A. Li Bassi, M. G. Beghi, A. Podest+á, P. Milani, A. Zakhidov, R. Baughman, D. A. Walters, and R. E. Smalley, Physical Review B **67,** 1554071 (2003).

22. V. Gadagkar, P. K. Maiti, Y. Lansac, A. Jagota, and A. K. Sood, Physical Review B **73,**1 (2006).

23. V. Gadagkar, S. Saha, D. V. S. Muthu, P. K. Maiti, Y. Lansac, A. Jagota, A. Moravsky, R. O. Loutfy, and A. K. Sood, Journal of Nanoscience and Nanotechnology **7,** 1753 (2007).

24. T. De Los Arcos, P. Oelhafen, and D. Mathys, Nanotechnology **18,** 265706 (2007).

25. M. Damnjanovic, E. Dobardzic, I. Milosevic, T. Vukovic, B. Nikolic, New Journal of Physics **5,** 148 (2003).

Miscellaneous Work

1. *"Nanocrystalline $NaNbO_3$ and $NaTaO_3$: Rietveld studies, Raman spectroscopy and dielectric properties,"* Vishnu Shanker, Saroj L. Samal, **Gopal K. Pradhan**, Chandrabhas Narayana and Ashok K. Ganguli, *Solid State Sciences **11** 562–569 (2009)*

2. *"Spin state transition in the ferromagnet $Sr_{0.9}Ce_{0.1}CoO_{2.85}$,"* R.V.K. Mangalam, **Gopal K. Pradhan**, Chandrabhas Narayana and A. Sundaresan, *Solid State Communications **146** 110–114 (2008)*

3. "Elastic and structural instability of cubic Sn_3N_4 and C_3N_4 under pressure," **Gopal K. Pradhan**, Anil Kumar, Umesh V. waghmare, Sudip K. Deb and Chandrabhas Narayana, *Physical Review B (Rapid. Com.)* under review

4. *"Velocity of Sound of Confined Water in Thermo-responsive Nanogel Suspensions,"* **Gopal K. Pradhan**, B.V.R.Tata, J. Brijitta and Chandrabhas Narayana, *Manuscript under preparation*